

**Biochemical and Structural Characterization of the Starter Module in the Saxitoxin Biosynthesis
Pathway**

by

Yongtong Lao

A dissertation submitted in partial fulfillment
of the requirements for the degree of
Doctoral of Philosophy
(Chemical Biology)
in the University of Michigan
2022

Doctoral Committee:

Professor Janet Smith, Chair
Associate Professor Jayakrishnan Nandakumar
Professor Alison Narayan
Professor Patrick O'Brien

Yongtong Lao

yolao@umich.edu

ORCID iD: 0000-0003-2727-1583

© Yongtong Lao 2022

Dedication

This dissertation is dedicated to students who believe in science.

Acknowledgements

My doctoral work would have been impossible without many of you. Firstly, I would like to thank my advisor Janet Smith for her patience, guidance, and wisdom throughout this project. Janet not only has provided me with advice and mentorship on scientific research but also supported me in exploring my interest in science illustration. I also thank my committee members, Jayakrishnan Nandakumar, Alison Narayan, and Patrick O'Brien, who always give brilliant suggestions about my research and inspire future directions to develop the project further. I am incredibly grateful to Meredith Skiba and Stephanie Chun. They have also worked on the saxitoxin project and most of my ideas in this project are developed from their valuable preliminary data.

My fellow lab best friends (Tyler Mccullough, Michael Rankin, and Yihua Li) made coming to work ten-fold more enjoyable. We turned many tedious lab chores into exciting competitions and took a daily walk(s) to rejuvenate ourselves with coffee/boba. I would like to give a special thanks to Michael Rankin, who is always a supportive audience to all my talks (sometimes the only audience of my practice talks), and the first reader of all my science writing. My thesis would not have been completed without him.

I developed my interest in science research during my undergraduate study. Dr. Joshua Schwochert was my research mentor for two years. He taught me not to be afraid to take risks and test new ideas. I always aspired to become a curious and motivated scientist like he is. With a role model like him, I am determined to keep making science progress and not to give up.

I would also like to thank my partner, Robert Benisch, for his continuous support, understanding, and motivation when I was stuck in the cycles of procrastination, especially during the last stressful months. I also appreciate his insightful feedback on my talks and writings.

The LC/MS-based assay analysis could not have been completed without the guidance and assistance of Dr. Wenqing Feng at the Life Science Institute, mass spectrometry core. Also, she helped me secure my scientist position at ThermoFisher Scientific through a last-minute mass spectrometry Bootcamp and interview preparation.

Also, the Ph.D. journey would be challenging without a stable and positive mindset. I would like to thank my therapists, Toby (a cat) and Zelda the dog. They never fail to brighten my days and help me relax after a hard day. Finally, I am grateful for the funding sources that have supported my research: The University of Michigan Life Science Institute, Program in Chemical Biology and Rackham Graduate School.

Table of Contents

| | |
|---|-----|
| Dedication | ii |
| Acknowledgements | iii |
| List of Tables | ix |
| List of Figures | x |
| Abstract | xii |
| Chapter 1 Introduction | 1 |
| 1.1 Natural Products | 1 |
| 1.2 Polyketide synthase biosynthesis pathway | 4 |
| 1.3 Starter modules of the type I polyketide synthases | 6 |
| 1.4 Methyltransferases in polyketide synthase pathways | 10 |
| 1.5 General mechanisms of natural product methyltransferases | 13 |
| 1.6 Metal-dependent methyltransferases in polyketide synthase pathways | 13 |
| 1.7 Thesis Review | 14 |
| 1.7.1 Functional and structural analysis of C-MT | 14 |
| 1.7.2 SxtA MT engineering | 14 |
| 1.7.3 Substrate selectivity and catalysis of SxtA AONS and DC | 15 |
| Chapter 2 Active Site Architecture of Polyketide Synthase Methyltransferase | 17 |
| 2.1 Summary | 17 |
| 2.2 Introduction | 18 |

| | |
|--|----|
| 2.2.1 Substrate selectivity and catalysis of SxtA AONS and DC | 18 |
| 2.2.2 Significance of biochemical and structural determination of the starter MTs | 19 |
| 2.3 Results and Discussion | 21 |
| 2.3.1 Structure of methyltransferase-decarboxylase in saxitoxin starter module..... | 21 |
| 2.3.2 Structural comparison of a starter MT and an extender MT | 28 |
| 2.3.3 Structural of SxtA MT-DC variant F458H..... | 31 |
| 2.3.4 The pre-catalytic and substrate-bound conformations in PKS starter C-MTs | 32 |
| 2.4 Conclusion..... | 37 |
| 2.5 Materials and methods..... | 37 |
| 2.5.1 Construct design | 37 |
| 2.5.2 Bacterial expression and purification | 38 |
| 2.5.3 Protein crystallization and structure determination | 39 |
| Chapter 3 Structural Basis of Methylation Control in Polyketide Synthase C- methyltransferase | 41 |
| 3.1 Summary | 41 |
| 3.2 Introduction | 42 |
| 3.2.1 The magic methyl effect..... | 42 |
| 3.2.2 The medicinal potential of saxitoxin | 42 |
| 3.2.3 The starter module of the saxitoxin biosynthesis pathway..... | 43 |
| 3.3 Results and Discussion..... | 44 |
| 3.3.1 Catalytic activities of SxtA MT-DC..... | 44 |
| 3.3.2 The active SxtA DC may restrain the methylation extent by SxtA MT..... | 46 |
| 3.3.3 Effect of bound metal in the SxtA MT active site | 49 |
| 3.3.4 A catalytic base for dimethylation..... | 50 |
| 3.3.5 The F458H substitution increases monomethylation efficiency | 51 |
| 3.3.6 Other factors in the extent of methylation | 54 |

| | |
|--|----|
| 3.3.7 Selectivity filter for the extent of methylation | 56 |
| 3.3.8 SxtA MT metal preference | 59 |
| 3.3.9 Conclusion | 60 |
| 3.4 Materials and Methods | 61 |
| 3.4.1 Plasmid preparation | 61 |
| 3.4.2 Bacterial expression..... | 62 |
| 3.4.3 Purification of SxtA MT-DC and its variants, and AprA ACP | 62 |
| 3.4.4 Production of acyl-ACPs..... | 63 |
| 3.4.5 Protein crystallization and structural determination..... | 63 |
| 3.4.6 Methylation assay..... | 64 |
| 3.4.7 Decarboxylation | 65 |
| 3.4.8 Methylation time course assay | 65 |
| 3.4.9 Methylation kinetic assay | 65 |
| 3.4.10 Analysis of reaction products by liquid chromatography-mass spectrometry (LC-MS) | 66 |
| Chapter 4 The Functional and Structural Analysis of Saxitoxin DC and AONS | 70 |
| 4.1 Summary | 70 |
| 4.2 Introduction | 72 |
| 4.2.1 The magic methyl effect..... | 72 |
| 4.2.2 Proposed features of controlling substrate selectivity in DCs..... | 76 |
| 4.2.3 AONS activity on Isobutyryl-ACP..... | 78 |
| 4.2.4 AONS structure | 79 |
| 4.2.5 AONS may mediate dimerization of the SxtA module | 80 |
| 4.2.6 Conclusion | 82 |
| 4.3 Materials and Methods | 86 |
| 4.3.1 Plasmid preparation | 86 |

| | |
|---|----|
| 4.3.2 Bacterial expression..... | 86 |
| 4.3.3 Purification of GphF DC, CurA DC and SxtA AONS..... | 86 |
| 4.3.4 Protein crystallization and structure determination..... | 87 |
| 4.3.5 Decarboxylation..... | 88 |
| 4.3.6 AONS assay and assay analysis by LC-MS..... | 88 |
| 4.3.7 AONS structure prediction and substrate modeling..... | 89 |
| Chapter 5 Conclusions and Future Directions..... | 90 |
| 5.1 Overview..... | 90 |
| 5.1.1 Structural comparison of PKS starter and extender MTs reveals substrate binding features..... | 90 |
| 5.1.2 PKS starter MTs require a permissive filter for the dimethylated product..... | 91 |
| 5.1.3 Substrate selectivity of PKS DCs is influenced by active pocket size and hydrophobicity..... | 92 |
| 5.1.4 AONS structure and activity..... | 93 |
| 5.2 Future Directions..... | 94 |
| 5.2.1 Investigate and expand the substrate scope of SxtA MT..... | 94 |
| 5.2.2 Expanding the MTs utility..... | 94 |
| 5.2.3 Understanding the full SxtA module architecture..... | 95 |
| 5.2.4 Further investigation of substrate selectivity of SxtA, GphF and CurA DCs..... | 96 |
| Bibliography..... | 97 |

List of Tables

| | |
|--|-----------|
| Table 2.1. Collection and refinement statistics of SxtA MT-DC and its variant F458H crystallographic data. | 35 |
| Table 2.2. Primers used for ligation-independent cloning and site directed mutagenesis. .. | 38 |
| Table 3.1. Primers used for ligation-independent cloning (LIC) and site-directed mutagenesis..... | 61 |
| Table 3.2. Collection and refinement statistics of AprA MT-DC crystallographic data..... | 64 |

List of Figures

| | |
|---|----|
| Figure 1.1 Natural products and their pharmaceutical applications. | 2 |
| Figure 1.2 Source of FDA-approved drugs in 1981-2019 ² | 3 |
| Figure 1.3. Comparison of polyketide synthase (PKS) and nonribosomal peptide synthetase (NRPS) systems. | 5 |
| Figure 1.4 Type I polyketide synthase-like starter modules. | 9 |
| Figure 1.5 Three catalytic strategies for methylation. | 12 |
| Figure 2.1. Structures and substrate specificity of polyketide synthase C-methyltransferases (PKS C-MTs)..... | 21 |
| Figure 2.2 SxtA MT-DC protein crystals. | 23 |
| Figure 2.3. SxtA MT-DC di-domain structure and interaction..... | 24 |
| Figure 2.4. The architecture of SxtA MT core..... | 27 |
| Figure 2.5. Electron density for critical sites, ligands, and di-domain linker of SxtA MT-DC.... | 27 |
| Figure 2.6. Active site of SxtA MT with SAH and of SxtA F458H with malonate. | 28 |
| Figure 2.7. Comparison of structures of SxtA and CurJ MTs | 31 |
| Figure 2.8. SxtA MT-DC F458H crystals..... | 32 |
| Figure 2.9. Pre-catalytic and substrate-bound conformations in SxtA and AprA MT1. | 34 |
| Figure 3.1. Reaction scheme of SxtA MT and DC domains in saxitoxin biosynthesis..... | 44 |
| Figure 3.2. SxtA MT-DC catalysis and structure. | 47 |
| Figure 3.3 SxtA mutagenesis approaches and multiple sequence alignment of key MT regions. | 49 |
| Figure 3.4 Methylation activity of SxtA MT-DC variants. | 50 |
| Figure 3.5 Monomethylation rate of SxtA MT-DC F458H/T637V and T637V. | 52 |

| | |
|---|----|
| Figure 3.6. Mn ²⁺ ligand sphere and second-shell environment..... | 54 |
| Figure 3.7. Active site of SxtA MT-DC F458H with dimethylmalonate and SAM..... | 56 |
| Figure 3.8. Comparison of selectivity filters for methylation extent in AprA MT1 and SxtA MT. | 58 |
| Figure 3.9. Impact of Ile204 on the extent of methylation. | 59 |
| Figure 3.10. Representative electrospray-ionization (ESI) mass spectra of AprA ACP ejection fragments in reaction samples..... | 69 |
| Figure 4.1. Chemical structures of saxitoxin and its derivative, gonyautoxin 5..... | 71 |
| Figure 4.2 Reaction scheme of SxtA MT, DC and AONS in the SxtA module. | 72 |
| Figure 4.3. Methylation and decarboxylation activity by SxtA MT-DC..... | 74 |
| Figure 4.4 Summary of decarboxylation activity of Mal-, MeMal- and Me ₂ Mal-ACP by SxtA, GphF, and CurA DCs..... | 75 |
| Figure 4.5. Proposed decarboxylation mechanisms for SxtA, CurA and GphF DCs..... | 76 |
| Figure 4.6. Comparing active sites of CurA, SxtA, and GphF DCs..... | 77 |
| Figure 4.7. Representative electrospray-ionization (ESI) mass spectra of AONS product. | 79 |
| Figure 4.8. Proposed AONS mechanism. | 80 |
| Figure 4.9. Structure of SxtA AONS in complex with its reaction intermediate (3)..... | 82 |
| Figure 4.10. Structure of BioF AONS in complex with its reaction intermediate (4) (PDB: IDJ9). | 84 |
| Figure 4.11. Sequence alignments of SxtA AONS and its structural homologs. | 86 |

Abstract

Natural products harbor great therapeutic potential and represent nearly 50% of FDA approved drugs. However, because of their structural diversity and complexity, many natural products cannot be chemically synthesized efficiently. Natural product biosynthesis pathways, especially the polyketide synthases (PKS) that condense acyl groups to form polyketides, are seen as powerful, chemoenzymatic tools to synthesize chemically challenging compounds. To harness the chemoenzymatic potential of PKS pathways, it is important to investigate their biochemical mechanisms and structural details.

Saxitoxin interacts with the voltage-gated sodium channels and is one of the most potent neurotoxic alkaloids known. Saxitoxin derivatives have potential for development as selective neuropathic pain treatments. Through X-ray crystallography, biochemical assays, and mutagenesis, we further study the enzymes involved in the starter module of the saxitoxin biosynthesis pathway and expand their enzymatic capabilities.

Three catalytic domains are found in the saxitoxin starter module: *C*-methyltransferase (*C*-MT), decarboxylase (DC) and 8-amino-7-oxonanoate synthase (AONS). The SAM- and metal-dependent SxtA MT initiates the biosynthesis. Structural and biochemical studies revealed essential catalytic residues and features that control the methylation extent in SxtA MT. Through a few simple amino acid substitutions, this monomethylating SxtA MT is converted into a dimethyltransferase. Interestingly, the two downstream enzymes, DC and AONS can process this MT product with an additional methyl group (dimethylmalonyl-ACP) to yield a methylated version of the saxitoxin precursor. This may be used to alter the chemical outcome of the

saxitoxin pathway via domain modification, potentially resulting in the development of saxitoxin analogs with reduced toxicity and high selectivity as a pain medicine.

SxtA DC was thought to be a gatekeeper because it does not act on MT methylation substrate (malonyl-ACP) and decarboxylates only the methylation product (methylmalonyl-ACP). Further investigation of SxtA DC demonstrates that it may not evolve a mechanism to filter another chemical group (such as dimethylmalonyl-ACP) that is uncommon in its biosynthesis environment. Substrate modeling with the structures of SxtA, CurA and GphF DCs from the saxitoxin, curacin, and gephyronic acid biosynthesis pathways, respectively, reveals that the size of the malonyl-binding pocket determines their substrate preference. A DC with a large pocket would prefer a bulkier malonyl-substrate and vice versa.

Structural analysis of the final catalytic domain, AONS, was initiated with an AlphaFold prediction. The AONS performs condensation between an arginine and an acyl group to yield a propionylated arginine-like SxtA precursor. This structure and the AONS's behavior in solution have suggested that AONS functions as a dimer. Characterization of MT, DC and AONS advances the understanding of the biosynthesis of chemically diverse natural products and provides valuable insights towards harnessing the biocatalytic potential of enzymes in PKS pathways.

Chapter 1 Introduction

1.1 Natural Products

Natural products are secondary metabolites produced by living organisms. Secondary metabolites give the host competitive advantages and extrinsic functions that ultimately aid survival³⁻⁶. Bacteria, fungi, and plants produce secondary metabolites with a diverse range of bioactivities, including antifeedant activity⁷⁻⁹. Natural products' unique structural characteristics and diversity distinguish them from synthetic chemicals. They have more stereocenters, fewer rotational bonds, more spiro rings, and different chemical compositions than synthetic compounds¹⁰. For example, *Artemisia annua*, a type of wormwood, has evolved an immune pathway, producing artemisinin to cope with pathogen infection¹¹. Natural products also play a vital role in solving challenges in the medical field and environmental sustainability¹²⁻¹⁴. Like most natural products, artemisinin has medical potential; it is active in preventing parasitic and viral infection. Interestingly to the biomedical community, it also displays anti-tumor properties¹⁵ (**Figure 1.1**). Recently, scientists have been investigating if it could also effectively treat COVID-19 infection¹⁶.

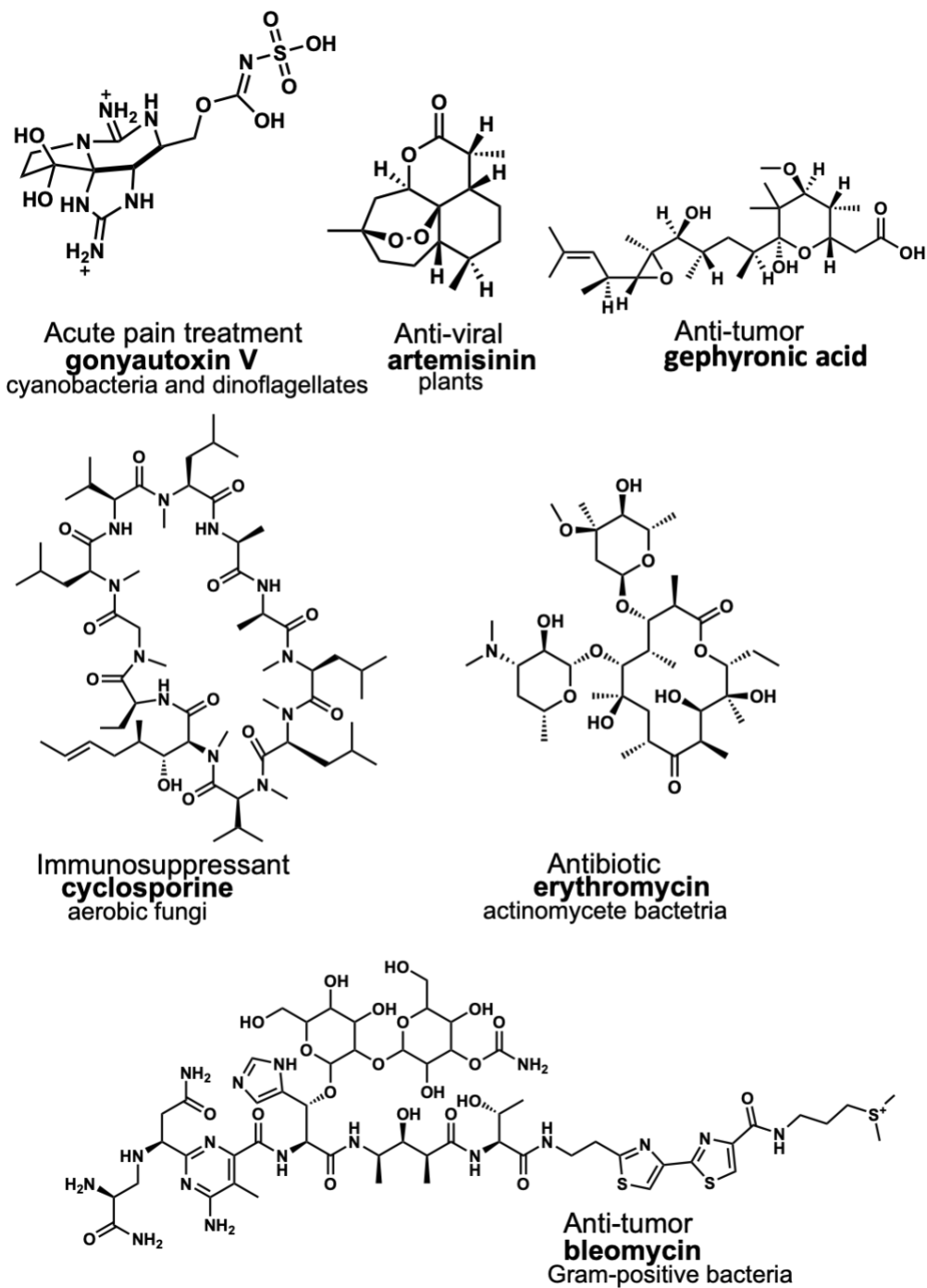


Figure 1.1 Natural products and their pharmaceutical applications.

Chemical structures of several bioactive natural products and their producing organisms and bioactivities are listed.

Using natural products to treat illness can be traced back to ancient times¹³. The earliest medical record of natural products was documented on clay tablets in cuneiform from Mesopotamia (2600 B.C.) about using oils from *Cupressus sempervirens* (Cypress) and *Commiphora* species (myrrh) to treat inflammation¹⁷. However, it was not until 1826 that the first purified natural product, morphine, become commercially available as a drug¹⁸. Now, natural products and their inspired compounds represent nearly half of newly approved medications per year, displaying antiviral, anti-tumor, immunosuppressant, and antibiotic activities, among many others. (Figures 1.1 and 1.2) From 1981 to 2019, 50% of FDA approved drugs were either unaltered natural products and their analogs² (Figure 1.2). This statistic is especially impressive, given that less than 1 % natural products has been exploited^{19,20}.

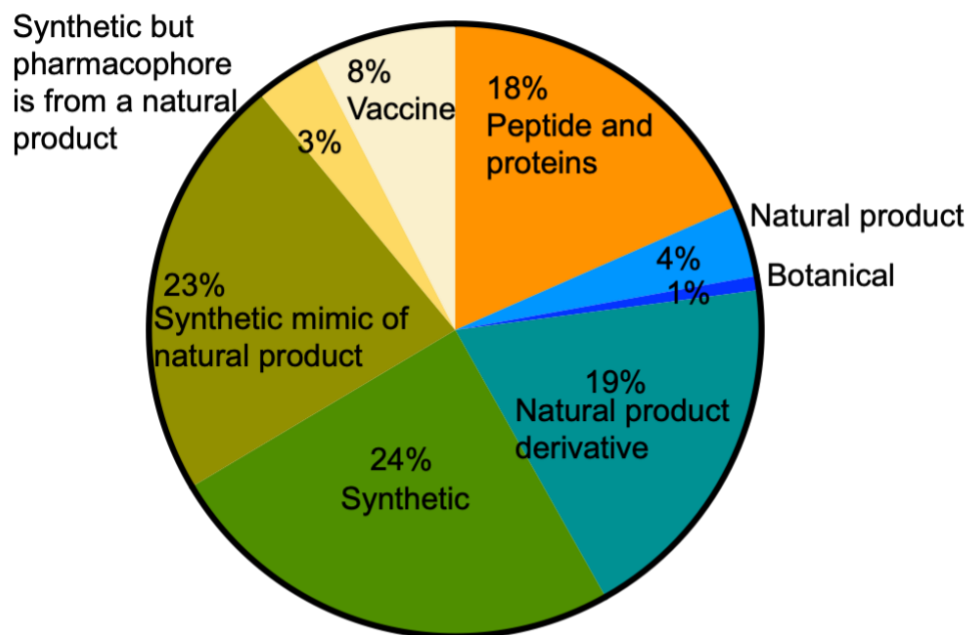


Figure 1.2 Source of FDA-approved drugs in 1981-2019²
 Natural products and their mimics and derivatives represent 50% of FDA-approved drugs.

Besides natural products' medical use, natural product biosynthesis pathways harbor enzymes that can be engineered as biocatalysts for a wide range of industrial and medical applications. A notable example that demonstrated the potential of natural product enzymes was achieved in the production of vanillin, the most widely used flavoring agent in the food and cosmetic industries. An *E. coli* strain was engineered to produce vanillic acid. The vanillic acid was later extracted and reduced in vitro to make 99% of the vanillin we consume today. Consequently, the characterization of natural product biosynthesis pathways has led to several successful biosynthetic and metabolic engineering cases for therapeutics and other applications.

1.2 Polyketide synthase biosynthesis pathway

The biosynthesis of natural product is carried out by specialized enzymes, such as nonribosomal peptides synthetases (NRPS), polyketide synthases (PKS), and hybrids (**Figure 2.3**). For most natural products from microbial species, the enzymes responsible to produce a compound are encoded in a biosynthetic gene cluster^{21, 22}. A few well-known products that come from those pathways are the antibiotic erythromycin A (PKS)²³, the immunosuppressive cyclosporine (NRPS)(**Figure 1.1**)²⁴ and the anti-tumor bleomycin (hybrid)²⁵. NRPS are multidomain mega-enzymes that condense amino acids, often forming branched or cyclic peptides (**Figure 1.3**). PKS are similarly sized, but instead they condense acyl-CoA moieties into longer chains. Their structure and mechanism are homologous with that of fatty acid synthases (FAS). A simple building block, acyl-coenzyme A (CoA), is used by the PKS enzymes in a four-step process: loading, elongation, modification, and transfer of the substrate from module to module²⁶. This four-step process adopts different mechanisms depending on the specific PKS systems; in general, there are three types of PKS systems. Type I modular PKS systems are large, modular enzymes arranged like an assembly line²⁷. In contrast to Type I PKS, Type II PKS

systems are composed of discrete enzymes²⁸ that iteratively elongate the carbon chain rather than handing off the product after a series of condensation events to the next module. Type III PKS are also iterative enzymes; however, they lack acyl carrier protein (ACP)²⁹ to shuttle building blocks and intermediates to downstream catalytic enzymes in type I and II pathways (**Figure 1.3**)^{30, 31}. Type I PKS systems have raised interest because of their high biosynthetic capability and modularity^{32, 33}. This interest has led to extensive study and attempts in engineering designer type I PKS pathways to generate custom natural product analogs^{34, 35}.

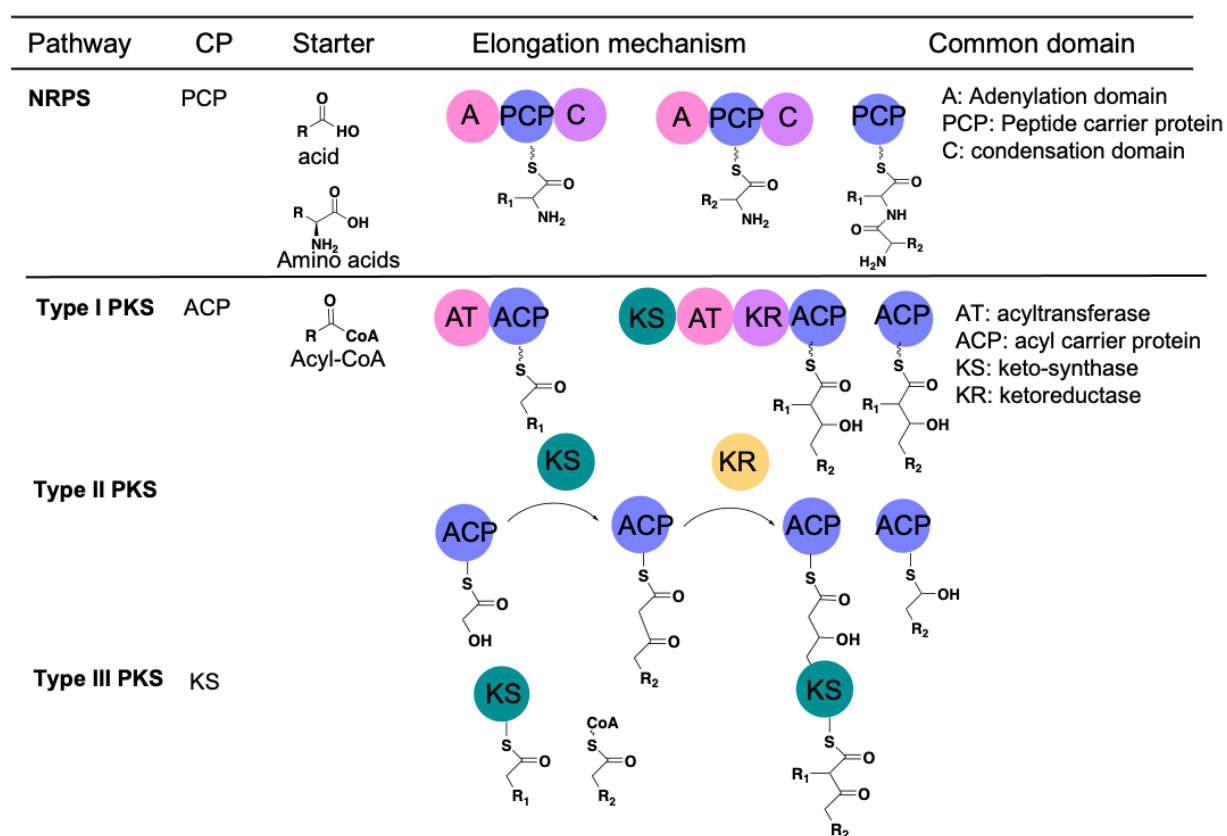


Figure 1.3. Comparison of polyketide synthase (PKS) and nonribosomal peptide synthetase (NRPS) systems.

The minimally required domains in a NRPS pathway are an adenylation domain (A), a peptide carrier protein (PCP), and a condensation domain (C); In type I and II PKS, they are ketosynthase (KS), acyltransferase (AT) and acyl-carrier protein (ACP). In PKS pathways, functional group R₂ refers to an extended carbon chain

1.3 Starter modules of the type I polyketide synthases

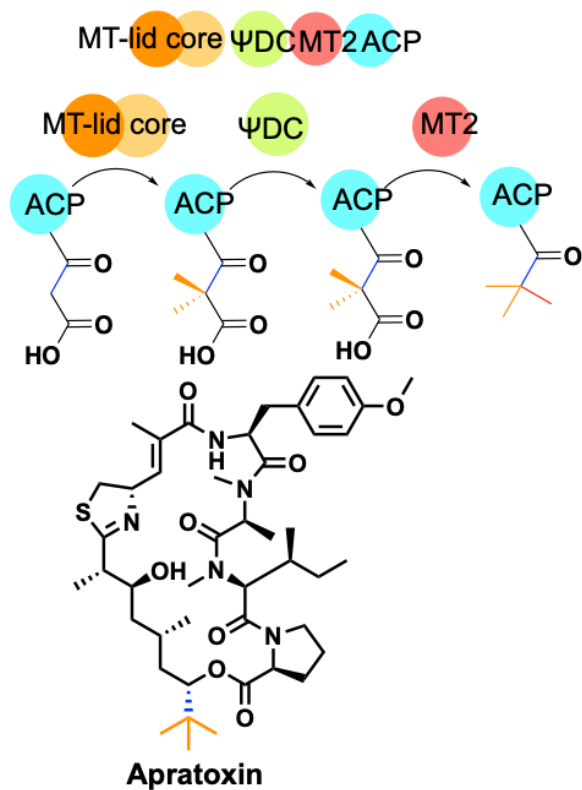
In many Type IPKS pathways, biosynthesis is initiated by an acyltransferase (AT). This enzyme transfers the acyl group from acyl-CoA onto the thioester of the phosphopantetheine (Ppant) arm of a holo-ACP within the starter module. Some starter modules contain a KS (ketosynthase) domain that decarboxylates substrates such as malonyl and methylmalonyl³⁶. These acyl-ACP products of the starter module are then passed to the KS domain in the first extension module, where Ppant-bound substrate is transferred onto the KS active site cysteine. The extender KS domain catalyzes decarboxylative Claisen condensation to extend the polyketide by one unit^{37, 38}. Next, modification enzymes within the module, such as enoylreductases (ER)^{39, 40}, dehydratases (DH)⁴¹, methyltransferases (MT)⁴²⁻⁴⁴ and ketoreductases (KR)⁴⁵, catalyze additional processing of the polyketide. After every enzyme processes the growing polyketide within the module, the chain will be passed onto the KS domains in the following extension modules for additional rounds of elongation and modification. Eventually, the polyketide chain meets the thioesterase (TE) domain that releases the product via either enzymatic hydrolysis or cyclization⁴⁶⁻⁴⁸.

In a few cases, cognate AT and KS domains are missing in the starter module of some pathways such as the apratoxin⁴³, saxitoxin^{49, 43} and gephyronic acid⁵⁰ biosynthesis pathways (**Figure 1.4**). In these cases, a discrete AT from another pathway may catalyze the acyl transfer reaction to initiate these biosynthesis pathways⁵¹; however, in most cases, the loading ATs are not identified yet. In the saxitoxin and gephyronic acid biosynthesis pathways, SxtA and GphF starter modules begin their biosynthesis with one or two methylations on malonyl-ACP, followed by decarboxylation. In the apratoxin biosynthesis pathway, the AprA starter module starts with dimethylation on malonyl-ACP. However, its decarboxylase is truncated and thus inactive

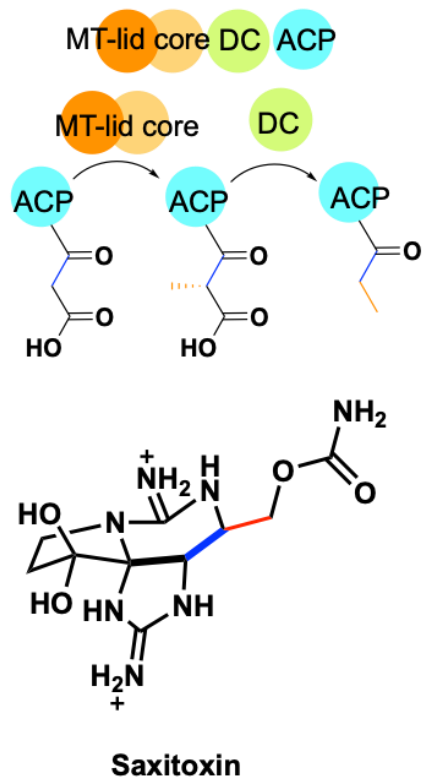
(ΨDC). AprA MT2, the following domain of AprA ΨDC, are bifunctional (catalyzing both methylation and decarboxylation), may have involved to compensate for the upstream inactive, truncated decarboxylase. The decarboxylation is essential to generate acetyl, propionyl and isobutyryl precursors in these pathways. (**Figure 1.4**). Even though it is truncated, the AprA ΨDC plays an important structural role in stabilizing the AprA MT1, as excised AprA MT is not soluble without the ΨDC. Additionally, the decarboxylase may be a gatekeeper to promote fidelity of the pathway production. GphF DC only performs catalysis on dimethylmalonyl-ACP, the product of GphF MT. It exhibits low level of activity on methylmalonyl- and malonyl-ACP, the starting material and reaction intermediate of GphF MT.

Natural Product Functional and structural characterization of these unique starter modules improves PKS annotation and provides a more advanced understanding for PKS engineering. PKS pathways are an excellent target for chemoenzymatic engineering because alterations to both the domain content and domain order may alter the identity of the final product, thereby increasing the chemodiversity of available polyketides.

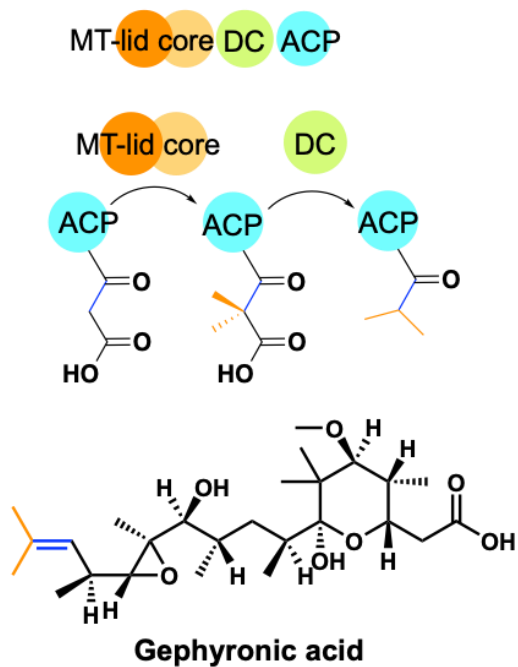
AprA, BryX



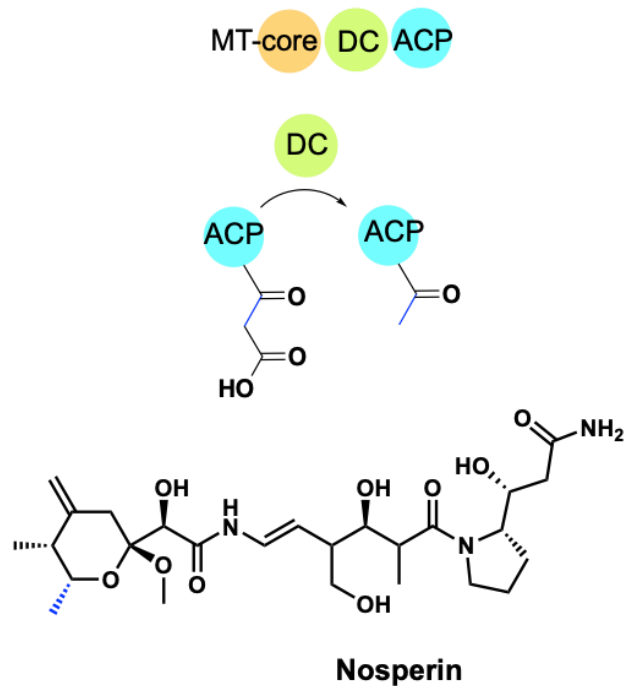
SxtA, Tal



GphF



Bat1, NspA



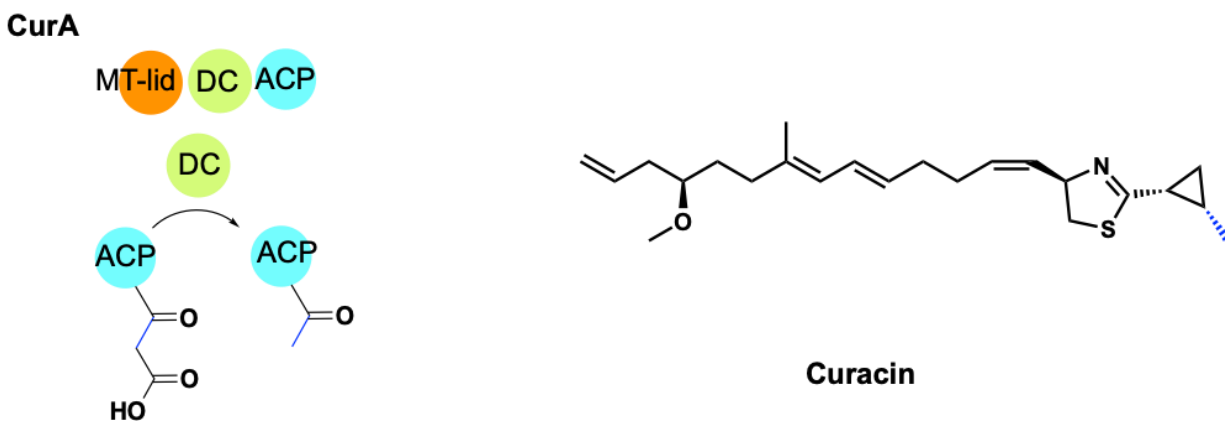


Figure 1.4 Type I polyketide synthase-like starter modules.

Domain architecture of acyl producing PKS starter modules: a methyltransferase (MT), a decarboxylase (DC), and an acyl carrier protein (ACP). The elongation steps that occur within the starter modules are depicted next to the domain architecture. Orange bonds represent the methyl groups installed by the MTs that are extensively studied in this thesis. Blue bonds mark the location of the acyl group in the chemical structures of these natural products. Abbreviations are as the following: AprA, apratoxin A; Bry, bryostatin; Gph, gephronic acids; SxtA, saxitoxin; TaI, myxovirescin; Bat, batumin; Nsp, nosperin; Cur, curacin.

Some biosynthesis pathways are started with a methylation reaction by a starter MT. These MTs naturally catalyze the transfer of the activated methyl group from donor SAM (S-adenosyl-methionine) onto the acceptor C-nucleophile of the substrate. Methylation is a widespread modification of proteins, DNA, RNA, and small molecules. 4000+ MT structures were deposited in PDB between 1990-2022. 1700+ of them were complexed with either S-adenosyl-methionine (SAM) or the methyl transfer byproduct, S-adenosyl-homocysteine (SAH). SAM-dependent MTs catalyze methylation on *O*-, *C*-, *N*-, and *S*- nucleophiles⁵². Natural product biosynthesis pathways also contain these methyltransferases to build their structurally diverse and bioactive compounds^{53, 54}. Interestingly, most natural product MTs are SAM-dependent, and a large majority of them belong to the class I, characterized by the alternating β - α - β Rossmann-fold⁵⁵. The core fold is usually decorated with additional helices for substrate binding or

oligomerization, conferring on the PKS MTs the ability to catalyze reactions on an expansive repertoire of substrates and direct the substrate to another active site in the module.

1.4 Methyltransferases in polyketide synthase pathways

Structures of PKS MTs have revealed several features required for MT-catalyzed methyl transfer. Firstly, the active site architecture must allow proximity of the methyl acceptor and the donor (usually, SAM) within 3 Å⁵³. The methyl acceptor must be a chemically reactive nucleophile to accept the methyl group. In many cases, the methyl-accepting site is activated through proton abstraction or the exclusion of water molecules. MTs in PKS and NRPS pathways have evolved three recognized chemical mechanisms for their catalytic reaction: (1) proximity and desolvation⁵⁶, (2) general acid and base mediated catalysis, and (3) metal-dependent catalysis (**Figure 1.5**).

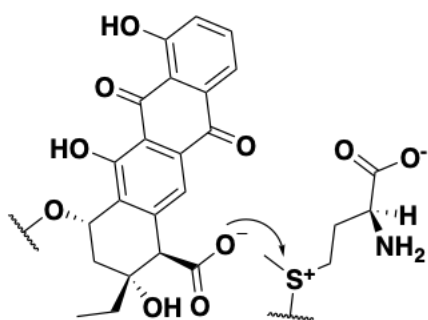
A mechanistic example of proximity and desolvation is an *O*-MT in daunorubicin biosynthesis pathway⁵⁷. This *O*-MT active site provides a chemical environment to exclude water from the methyl donor-acceptor interface (desolvation) and ensure the methyl acceptor is near the donor methyl group (proximity).

General acid and base-mediated methylation requires a catalytic base to activate the methyl acceptor for nucleophilic attack on the methyl donor group. This mechanism is employed by the CurJ *C*-MT from the curacin biosynthesis pathway employed this mechanism. CurJ MT contains a histidine in the active site that deprotonates the α carbon of the β -ketoacyl substrate⁴².

Finally, some cationic metal ions also facilitate methyl transfer. The metal coordinates the methyl acceptor to be in a favorable position for deprotonation by a water molecule or a catalytic base. The metal also perturbs the pK_a of the methylation site to promote deprotonation and the formation of a nucleophilic anion. A rare Fe³⁺ *C*-MT in the apratoxin biosynthesis

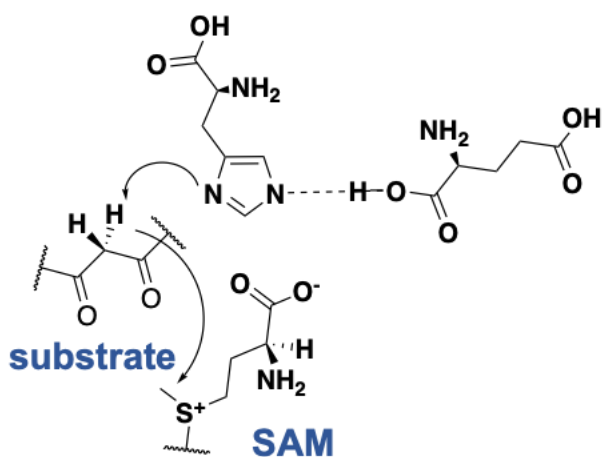
pathway may rely on both the acid-base and metal-dependent mechanisms for its catalysis⁴⁴. Fe^{3+} works as a Lewis acid to position the AprA substrate and lowers the pK_a of its methyl-accepting α carbon. For the first methyl transfer, a water molecule is likely to deprotonate the α carbon to facilitate the reaction. The pK_a of resulted product, methylmalonyl-ACP is higher than that of malonyl-ACP. For a second methyl transfer, a catalytic base (such as tyrosine) is required to deprotonate the accepting α carbon to generate a nucleophilic enol substrate, which, then attacks the activated methyl group of SAM to yield dimethylmalonyl-ACP.

Proximity and desolvation effects



substrate

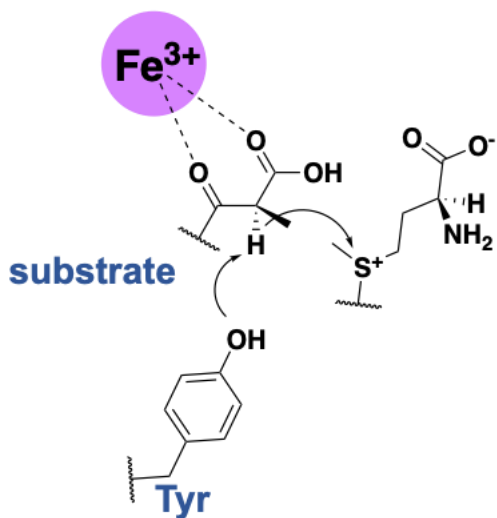
Acid-base mechanism



substrate

SAM

Metal-dependent mechanism



substrate

Tyr

Figure 1.5 Three catalytic strategies for methylation.

(a) The proximity and desolvation effects mechanism of DnrK O-methylation. The enzyme creates a chemical environment that excludes water molecules around the methyl donor-acceptor interface and positions the substrate near the methyl donor. (b) acid and base mediated mechanism demonstrated by CurJ MT. Glutamate enhances the basicity of the imidazole group of histidine via hydrogen bonding. Histidine works as a base to deprotonate the substrate driving the S_N2 methyl transfer from SAM. (c) Metal-dependent mechanism exemplified by AprA MT1. Metal mediated deprotonation of α - carbon of the substrate, generating a nucleophilic enol group to react with the electron-deficient methyl group of SAM.

1.5 General mechanisms of natural product methyltransferases

Interestingly, C-MTs, which initiate the biosynthesis of apratoxin, saxitoxin, and gephyronic acid, are metal-dependent, contrasting the C-MTs in the extender modules of the pathway. The metal may act as an additional regulator of these pathways because the biosynthesis will increase in a nutrient-rich (high metal) environment. These starter MTs share low sequence identity with C-MTs and O-MTs in PKS extender modules and have an MT lid about 200 amino acids long over their Rossmann-fold MT core. The presence of both MT lid and core is required for methyl transfer activity on the shared substrates, malonyl-ACP⁵⁸⁻⁶⁰. CurA MT lacks methylation activity because this MT inherently contains only the MT lid⁴⁴ (**Figure 1.4**).

1.6 Metal-dependent methyltransferases in polyketide synthase pathways

Common PKS engineering strategies involve domain swapping, module swapping, and modification to the active site to alter substrate specificity and protein function⁶¹. The approach of altering the order of domains and modules for novel compounds has met with little success because downstream enzymes in the pathways are involved in gatekeeping, rejecting non-native substrates^{62, 63}. The reactivity may also be regulated⁶² by complex protein-protein interactions and linkers between proteins^{64, 65}. Although many advanced structural biology techniques are available, structural characterization of a complete PKS module to understand protein-protein

interactions is complex and difficult because of its high flexibility, many conformations and large size. Large and flexible proteins are challenging to be crystallized and do not allow good averaging for cryo-EM microscopy. In the next two chapters, we report the functional and structural study of an excised MT-DC di-domain. Comprehensive structural and chemical insight is necessary for efficient engineering. Through engineering of the MT domain's function, we modify outcome of the saxitoxin starter module from monomethylation to dimethylation.

1.7 Thesis Review

1.7.1 Functional and structural analysis of C-MT

The following chapters present an advancement toward understanding the enzymes involved in the type I PKS-like starter modules of natural product biosynthesis pathways with an initial emphasis on the SxtA MT. Determination of the domain boundaries of SxtA C-MT-DC enabled its biochemical and structural characterization. Despite the distant relationship between SxtA C-MTs and other extender module C-MTs based on sequence similarity, structural alignment of the MT core of SxtA and extender module MT CurJ revealed overlapping core and secondary structures. The most distinct differences in their structures are a helical insertion near the active site that led to the divergence in their preference for different substrates and co-factors. Mass spectrometry-based biochemical assays enabled the characterization of the metal-dependent monomethylation activity of SxtA MT. Sequence alignment and structural comparison of various starter MTs provided insight to propose features that control whether one or two methyl groups are transferred onto a substrate.

1.7.2 SxtA MT engineering

Proposed features for methylation control in SxtA and AprA MTs were investigated by site-directed mutagenesis. Although the first round of site-directed mutagenesis followed by methylation assays did not reveal the basis of methylation control, these sets of mutagenesis led to an accidental discovery of a faster MT variant, F458H. This variant demonstrated fivefold greater catalytic efficiency than the wild type enzyme. To understand this, we determined the structure of the SxtA F458H variant, which not only helped us understand how the substitution of histidine for phenylalanine accelerated methylation reaction but also provided a complete view of the MT active site that was not available in the crystal form of the previously determined SxtA MT-DC wild type structure. This new structure permitted the modeling of a dimethylmalonate, substrate analog of dimethylmalonyl-ACP, into the active site. Dimethylmalonate modeling helped us identify an essential feature determining mono- versus dimethylation. Via site-directed mutagenesis of only 4 amino acid substitutions, we successfully turned the monomethylating SxtA MT into an efficient dimethyltransferase.

1.7.3 Substrate selectivity and catalysis of SxtA AONS and DC

Later, the decarboxylation and Claisen condensation activities of SxtA DC and 8-amino-7-oxononanoate synthase (AONS) of the nonnatural dimethylmalonyl-ACP product were investigated. SxtA AONS is a catalytic domain following the SxtA DC in the SxtA starter module. It is important that both SxtA DC and AONS accept the product of the engineered SxtA MT to promote chemodiversity of the module via domain engineering. Surprisingly, DC, which showed selectivity against methylmalonyl-ACP over malonyl-ACP, catalyzed a significant level of decarboxylation of dimethylmalonyl-ACP to generate isobutyryl-ACP. The AONS then catalyzed PLP-dependent carbon-carbon bond formation between arginine and isobutyryl-ACP to make a methylated saxitoxin precursor⁶⁶.

The result of SxtA DC reaction on the dimethylated substrate inspired further analysis of the substrate selectivity of the GNAT family DCs. This study was originally initiated by Skiba et al⁵¹. However, structural analysis of GphF and CurA DCs with bound isobutyryl-CoA and acetyl-CoA, respectively, coupled with a few site-directed mutagenesis experiments, did not reveal the basis of substrate selectivity. Herein, we determined new structures of GphF and CurA DC variants with bound dimethylmalonyl- and malonyl-substrates, respectively. In addition, we also modeled dimethylmalonyl-CoA into the active site of SxtA, GphF, and CurA DCs. We proposed that differences in the size of the active site pocket and hydrophobicity lead to their different substrate selectivity.

Chapter 2 Active Site Architecture of Polyketide Synthase Methyltransferase

Partially reproduced with permission from Lao, Y.; Skiba, M. A.; Chun, S. W.;

Narayan, A. R. H.; Smith, J. L. (2022) Structural Basis for Control of Methylation Extent in Polyketide Synthase Metal-Dependent C-Methyltransferases. *ACS Chem Biol*. Copyright 2022 American Chemical Society.

2.1 Summary

Installation of methyl groups can significantly improve the binding of small-molecule drugs to protein targets. However, site-selective methylation often presents a significant synthetic challenge. Methyltransferases (MTs) that require metal- and *S*-adenosyl-methionine (SAM)- are powerful enzymatic tools for chemically challenging *C*-methylation reactions. Natural product biosynthesis pathways are an excellent source of a variety of C-MT. Despite their potential, metal- and SAM-dependent MTs are the least studied in the polyketide synthase (PKS) pathways. Herein, we report two crystal structures of a starter methyltransferase in the saxitoxin (STX) biosynthesis pathway. We present two enzymatic conformations (pre-catalytic and substrate-bound) and identify substrate and cofactor binding sites. Structural comparison of the starter SxtA MT and the extender CurJ MT (from the curacin biosynthesis pathway) revealed features that distinguish their biochemical mechanisms and substrate scopes. In addition, the structural analysis provides insight into identifying residues critical for its catalysis.

2.2 Introduction

C-methyltransferases have intrigued scientists with their specific methylation of natural and synthetic compounds to optimize the production of pharmaceuticals^{67, 68}, agrochemicals, and functional materials⁶⁹. Moreover, some C-MTs act on a broad range of substrates in addition to their natural substrates⁷⁰ or accept SAM analogues with altered alkylating groups⁷¹⁻⁷³, demonstrating their utility as biocatalysts. Type I polyketide synthase (PKS) methyltransferases (MTs) are potential tools for catalytic methylation because they methylate under mild conditions, with high site- and stereo-selectivity^{66, 74, 42, 44, 70}. Modular type I PKSs generate bioactive natural products through successive elongation and tailoring reactions using malonyl- (Mal-), methylmalonyl- (MeMal-), and dimethylmalonyl- (Me₂Mal-) coenzyme A (CoA) building blocks^{75, 76}, among others.

2.2.1 Substrate selectivity and catalysis of SxtA AONS and DC

In modular PKS systems, biosynthesis is initiated by transferring an acyl group onto the loading acyl carrier protein (ACP) of the starter module. The starter module prepares a chemical precursor to pass onto extender modules for repeated Claisen condensation reactions to generate bioactive secondary metabolites^{37, 76}. Modular PKS system may harbor two types of C-MTs: starter and extender MTs. A starter MT initiates biosynthesis within a type I PKS-like module, followed by decarboxylation (usually by decarboxylase) to generate small, branched acyl substrates such as (pivaloyl-, acetyl-, propionyl-, and isobutyryl groups) (**Figure 1.4 in chapter 1**).

An extender MT elongates and modifies the polyketides in extender modules. An exceptional case is AprA MT2. This domain is found in the starter module of the apratoxin biosynthesis pathway and structurally and mechanistically resembles the extender MTs such as

CurJ MT. Both types of MTs are SAM-dependent and add α -branches to the polyketide substrates. A few of the extender MTs have been biochemically and structurally characterized such as CurJ MT⁴², Dis MT1⁷⁴, and AprA MT2⁴³, from the curacin, disorazol, and apratoxin biosynthesis pathways, respectively (**Figure 2.1**). Despite their overall structural similarities, marked by the Class I MT Rossmann - fold^{77, 52} and a large helical lid over the MT core, they have low sequence conservation at their substrate-binding sites and accept a variety of substrates for methylation (**Figure 2.1**). Also, extender MTs possess a conserved catalytic His-Glu dyad^{74, 42, 43} and may share a similar catalytic mechanism. The carboxyl group of glutamate forms hydrogen bonds to the imidazole of the histidine, increasing its basicity to deprotonate the substrate α -carbon, facilitating the methyl transfer. While much is known about the extender MTs, AprA MT1 was the only starter MT structurally characterized. AprA MT1 initiates apratoxin biosynthesis by dimethylating malonyl-ACP⁴³. (**Figure 1.4 in chapter 1**). In contrast to an extender MT, the AprA MT1 is metal-dependent^{66, 44} and may rely on both acid/base and metal-dependent mechanisms for its catalysis. Fe³⁺ binds to the bidentate malonyl-ACP substrate, positioning the substrate and potentially perturbing the pK_a of the methyl-accepting site for the second methyl transfer. Moreover, the structure of AprA MT1 is so distinct from any extender MTs that none of the existing MT structures (such as CurJ MT and AprA MT2) could be used to solve the phasing problem of AprA MT1 through molecular replacement. Instead, a seleno-methionine derivative was used to determine the phases.

2.2.2 Significance of biochemical and structural determination of the starter MTs

The study of starter MTs has been made difficult by the poor annotation of these domains. Using a starter MT sequence as a BLAST query returns many homologs mislabeled or noted as hypothetical proteins. Further studies of the starter MTs can improve the accuracy of

MTs classification and facilitate understanding their mechanism with the eventual goal of use as biocatalysts.

SxtA MT⁶⁶, GphF MT⁵⁰, BryX MT⁷⁸, and Tal MT⁷⁹, from the saxitoxin, gephyronic acid, bryostatin, and myxovirescin biosynthesis pathways, are starter MTs (**Figure 2.1**). They require SAM and metal ions to perform one or two methylations on malonyl-ACP. Herein we reported our structural studies of SxtA MT and decarboxylase (DC) with a deep analysis of the crystal structures of SxtA MT-DC at 2.6 Å and its variant F458H at 2.1 Å. SxtA MT is a rare Mn²⁺- and SAM-dependent monomethyltransferase that initiates the saxitoxin biosynthesis pathway. Following the SxtA MT reaction, the SxtA DC domain converts MeMal-ACP to propionyl-ACP, the extender unit for saxitoxin biosynthesis (**Figure 1.4**)^{66, 80}. SxtA MT-DC was expressed, purified, and crystallized as a didomain because excised SxtA MT is not soluble without the DC domain. The SxtA MT-DC wildtype and F458H structures revealed critical and conserved features within the PKS starter C-MT active site and conformational shift upon substrate binding. This study eventually inspired protein engineering to optimize the efficiency of the SxtA MT and alter its catalytic specificity (mentioned in later chapters)

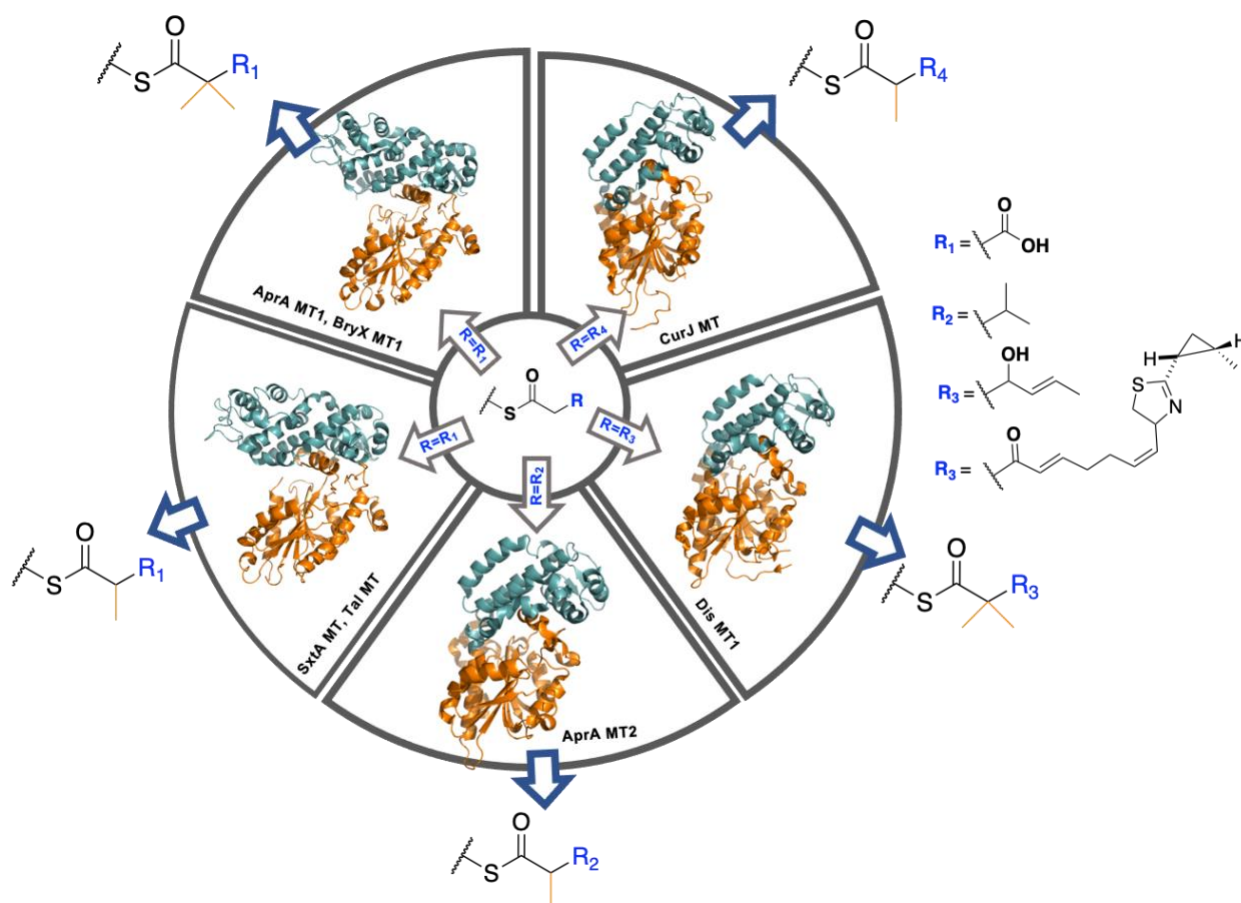


Figure 2.1. Structures and substrate specificity of polyketide synthase C-methyltransferases (PKS C-MTs).

MT structures are shown as cartoons and colored by subdomains (MT lid, blue; MT core, orange). Pathway abbreviations follow: AprA, apratoxin A; CurJ, curacin; Dis, disozarol; BryX, bryostatin; SxtA, saxitoxin A; Tal, myxovirescin A. The reaction products catalyzed by each enzyme are shown outside of the circle.

2.3 Results and Discussion

2.3.1 Structure of methyltransferase-decarboxylase in saxitoxin starter module

We first identified the boundaries of the SxtA MT (residues 1–506) and DC (residues 512–710) domains by conducting a multiple sequence alignment analysis using the crystal structures of the AprA MT^{66, 44}, CurA DC⁵⁸, and GphF DC⁵¹. The SxtA MT-DC is a monomer in solution and crystallized in the presence of Mn²⁺ and SAM with two molecules in the asymmetric unit (**Table**

1 and Figure 2.2). The structure was solved by molecular replacement from the structures of AprA MT1⁴⁴ (54% sequence identity, PDB: 6B3A) and CurA DC⁵⁸ (47% identity, PDB: 2REE) and refined to have 95.4% Ramachandran favored, R_{work} of 23.8% and R_{free} of 29.8% (**Table 1**). SxtA MT has a large N-terminal lid sub-domain (residue 1–234), which caps the MT-core and packs against the interior of the active site tunnel with its hydrophobic side chains, and a C-terminal core sub-domain (249–506), with class I MT superfamily characteristics (**Figure 2.3a**). The DC domain is tightly packed against the MT core domain, resembling the MT1- Ψ DC arrangement in AprA², perhaps explaining why excised SxtA MT is insoluble (**Figure 2.3 b, c**). The characteristic of the class I is include conserved SAM binding motifs⁵² and the alternating β - α - β secondary MT core fold (**Figure 2.4**). Several insertions (α -helices C, E, and F and β -strand 7) were found in the SxtA MT core in addition to the minimal MT core fold (**Figure 2.4b**). The C-terminus of α -helix F contains two out of the three metal coordinating ligands (glutamines 459 and 464). SxtA MT α -helix E constructs a hydrophobic surface to interact with an N-terminal helix of the DC. Several hydrogen bonding interactions further enhance this MT-DC contact (**Figure 2.3c**). Other insertions such as α -helix C and β -strand 7 may be the dimerization interface (modular dimerization is thought to be essential to PKS function^{81, 82}. Excised MT is a monomer in solution but may be a dimer in the module) or the connection site between domains (such as between the MT and ACP) in the module. The substrate tunnel is in a cleft between the subdomains. SAH¹, the hydrolyzed product of SAM, sits perpendicular to the MT core fold segment, with its adenosyl portion on the conserved GXGXG motif of the linker loop between β -sheet 1 and α -helix A (**Figure 2.4**).

¹¹ The identity of SAH cannot be determined by the poor density for the homocysteine moiety. SAH is the most likely species because SAM is not stable for days of crystallization unless protected by the enzyme. In the SxtA MT-DC WT structure, the active site was exposed due to the flexible didomain linker and therefore, the SAM is likely to not be protected.

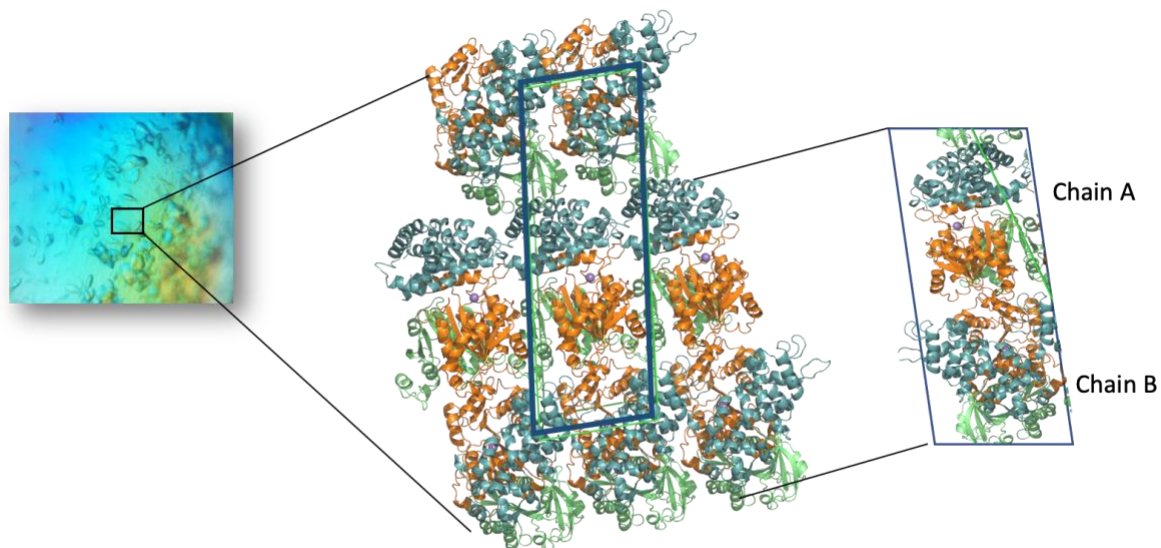


Figure 2.2 SxtA MT-DC protein crystals.

SxtA MT-DC di-domain was crystallized with two molecules (marked by chains A and B) in the asymmetric unit, despite being a monomer in solution. The blue box represents both the asymmetric unit and unit cell. The arrangement of proteins in the crystal lacks rotation symmetry and thus belongs to the P1 space group. C atoms in backbone are colored by the sub-domain of origin (blue MT lid, orange MT core, green DC).

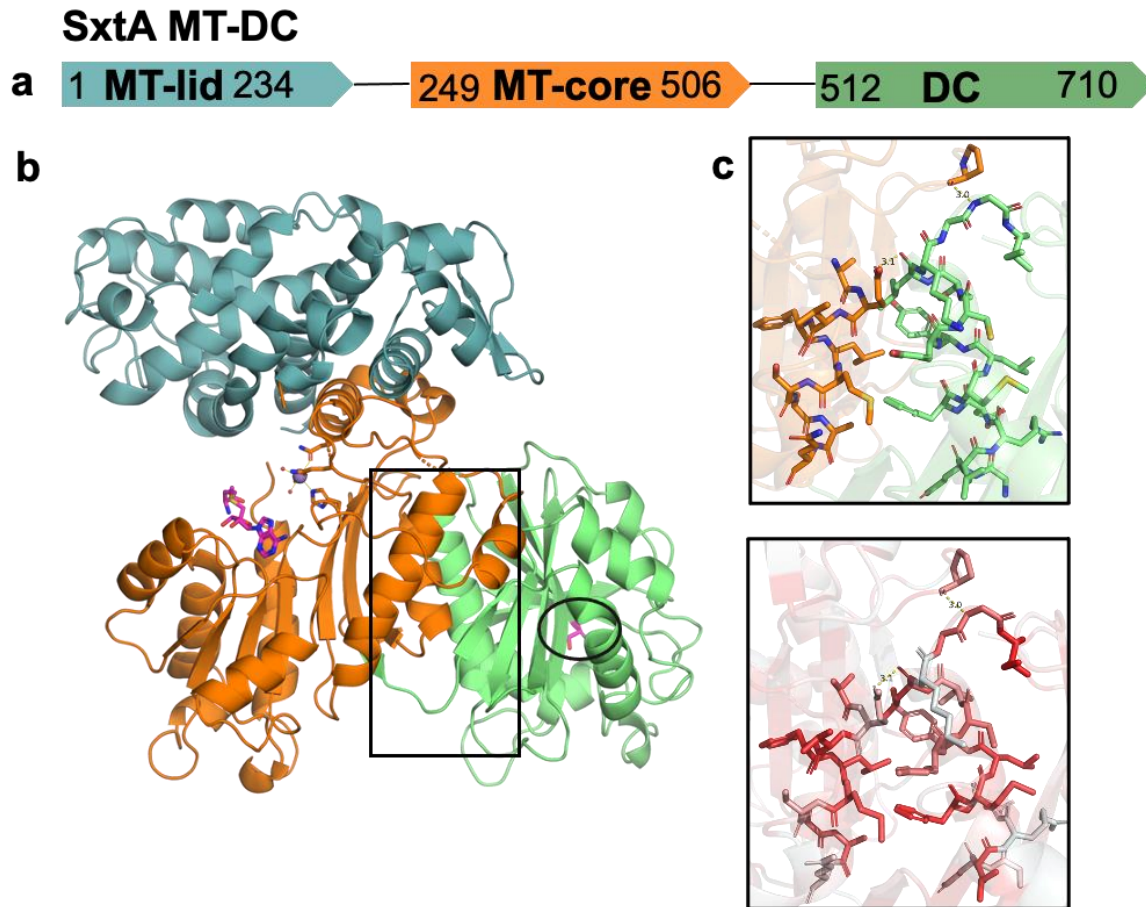


Figure 2.3. SxtA MT-DC di-domain structure and interaction.

(a) SxtA MT-DC di-domain boundaries. (b) Di-domain ternary complex with Mn^{2+} and SAH, colored by the domain (blue, MT lid; orange, MT core; green, DC). The Mn^{2+} (purple sphere), Mn^{2+} ligands (orange C), SAH (magenta C), and DC catalytic Thr637 (circled, magenta C) are shown in stick form (red O, blue N, yellow S). (c) MT-DC interaction is colored according to the domain of origin and hydrophobicity (red, nonpolar; white, polar).

A hexahedral metal coordination site is near the SAM/SAH binding site, and Mn^{2+} is coordinated by three water molecules and three amino acids (Glu459 and 464, and His372) (Figure 2.5c). The metal site marks the end of the substrate tunnel and likely the terminal of the Mal-ACP, where the carboxyl group locates (Figure 2.6). This structure missed some essential information due to regions of disorder. The flexible sub-domain linker (residues 235–253) wraps around the active site, but residues 235–249 were disordered in this crystal form (Figure 2.5a).

As a result, although electron density was strong for the metal ion and the SAH adenosine moiety, it was weak for the homocysteine group (**Figure 2.5b**), proximal to the disordered sub-domain linker. The disorder also accounts for the inability to obtain crystals in this form for a complex with the substrate analog malonate.

Figure 2.4. The architecture of SxtA MT core.

(a) Di-domain ternary complex with Mn^{2+} and SAH (cyan, cartoon). The Mn^{2+} (purple sphere), Mn^{2+} ligands (orange C, sticks), and SAH (magenta C, stick) are depicted. Alternating α -helices (orange) and β -strands (navy) mark the Rossmann-fold in the MT core. (b) Topology of SxtA MT core and a MT core-fold. Dashed lines highlighted insertions for potential oligomerization, substrate binding, and downstream domain connection. The three metal coordinating residues (His372, Gln464, and Gln459) were marked by red spots, and the conserved GXGXG for SAM/SAH binding was marked by a purple triangle.

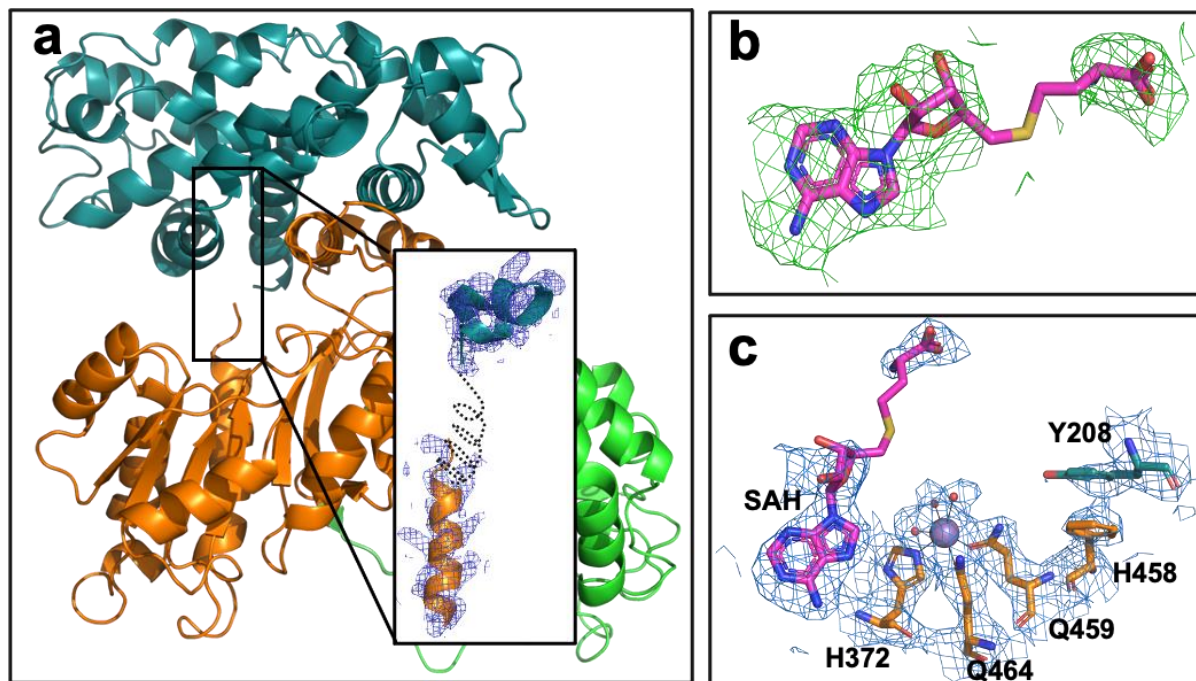


Figure 2.5. Electron density for critical sites, ligands, and di-domain linker of SxtA MT-DC.

(a) $2.6\text{-}\text{\AA}$ $2F_o - F_c$ electron density of residues 218-261 in SxtA MT-DC structure. The majority (residues 235-249) of the flexible sub-domain linker had no electron density and was represented by a black dashed curve. (b) $F_o - F_c$ omit density. SAH is modeled, although the homocysteine group is disordered. (c) Active site with Mn^{2+} (purple sphere) and SAH (magenta C). C atoms in amino acid side chains are colored by the sub-domain of origin, as in Figure 2.3. The $2F_o - F_c$ density (blue) is contoured at 1.0 RMS, and the $F_o - F_c$ omit density (green) at 3.0 RMS.

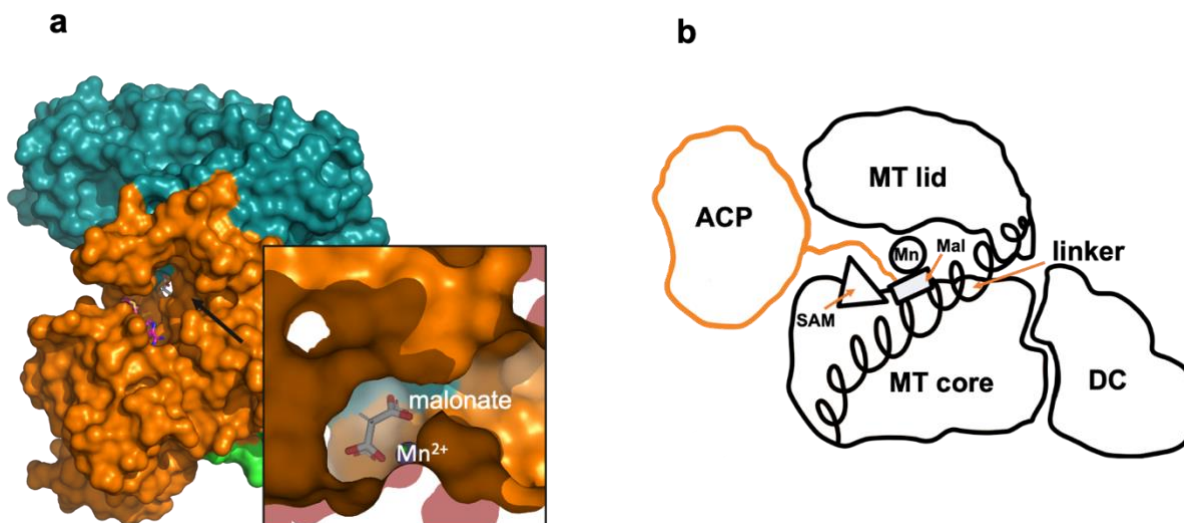


Figure 2.6. Active site of SxtA MT with SAH and of SxtA F458H with malonate. (a, b) In the SxtA MT structure, the di-domain linker is disordered and not built (a). (b) In SxtA F458H structure, the di-domain linker is stabilized and shown in surface view. Malonate is coordinated by the metal and displaces two water molecules. Metal-binding amino acids (orange), malonate (white) and SAM (magenta) are shown in sticks. Metal, Mn²⁺, are portrayed as a purple sphere. (c) A cartoon depiction of SxtA MT active site architecture and proposed fitting of malonyl-ACP in the di-domain tunnel. SxtA MT lid, core and SxtA DC are colored by the sub-domain of origin, as in **Figure 2.3**.

2.3.2 Structural comparison of a starter MT and an extender MT

Despite having low sequence identities (< 20%⁴⁴), PKS starter MTs and extender MTs share a few conserved structural features, such as an N-terminal helical lid (**Figure 2.7a-b**). The MT-lid caps the MT-core and packs the interior of the active site tunnel with its hydrophobic side chains. However, starter SxtA and extender CurJ MT lids are structurally distant; SxtA MT has a slightly longer lid (residue 1-234) than CurJ MT (residue 28-171). The cores of the two enzymes are more structurally related (RMSD = 3.2 Å, 116 backbone atoms are aligned) (**Figure 2.7c**). The Glu-His dyad, which is conserved among embedded MTs, is also found in an analogous position in SxtA MT (**Figure 2.7d**). Surprisingly, this dyad (His 372 and Glu 434) in SxtA MT does not directly contribute to the catalysis as in extender MTs. Instead, this dyad participates in the first

and secondary metal spheres to coordinate Mn^{2+} . Both SxtA and CurJ MTs have a helical insertion at an analogous position within the Rossman fold (SxtA residues 449-466 and CurJ residues 307-341⁴²) to construct their substrate-binding pocket and metal coordination sphere (**Figure 2.7a, b, f**). High sequence variation within the insertion likely plays a significant role in distinguishing the substrate, cofactor specificity, and catalytic mechanism among MTs. Extender MTs exhibit high sequence variation in this region and have a broad substrate library ranging from a short isobutyryl-ACP to a more complex β -ketoacyl substrate (**Figure 2.1**).

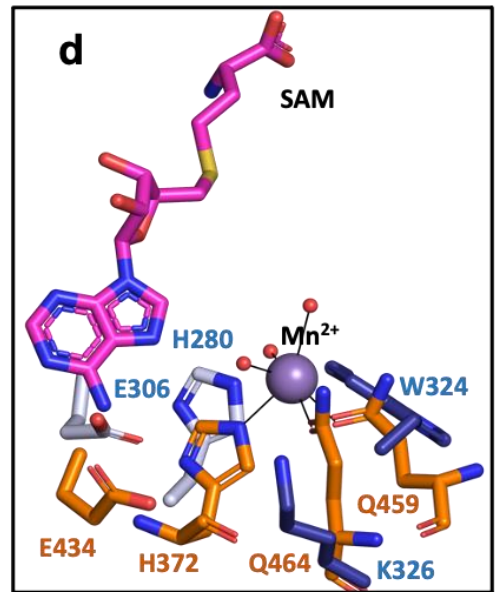
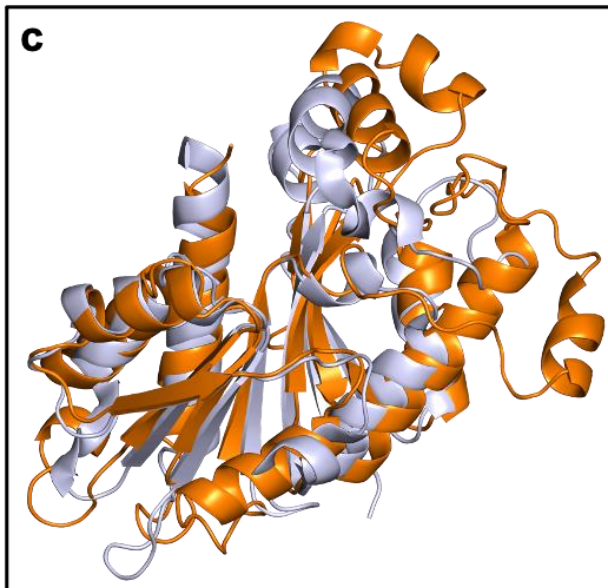
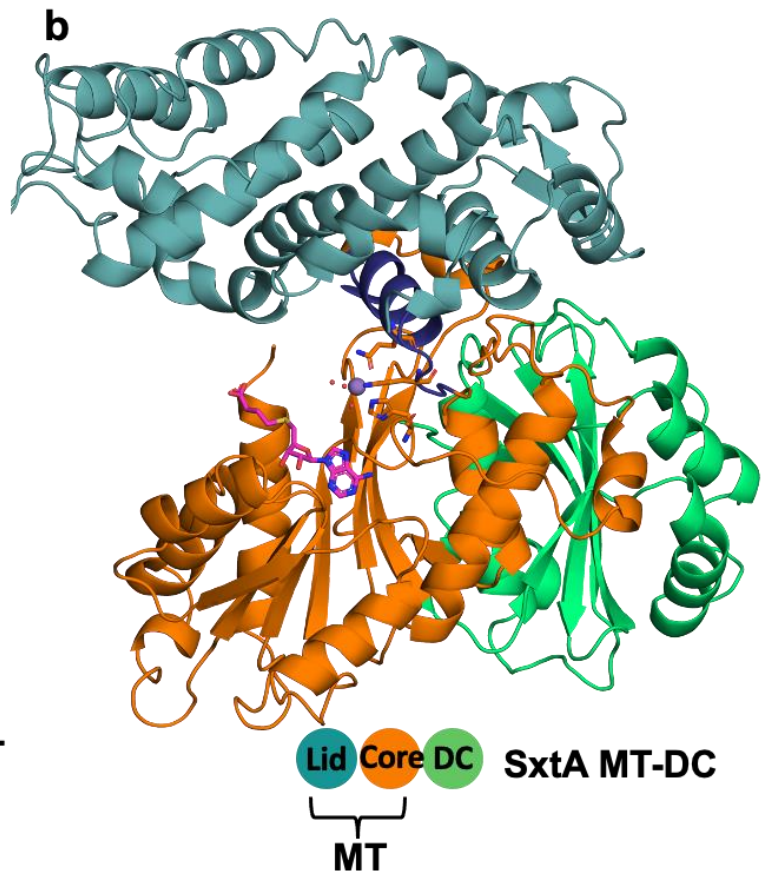
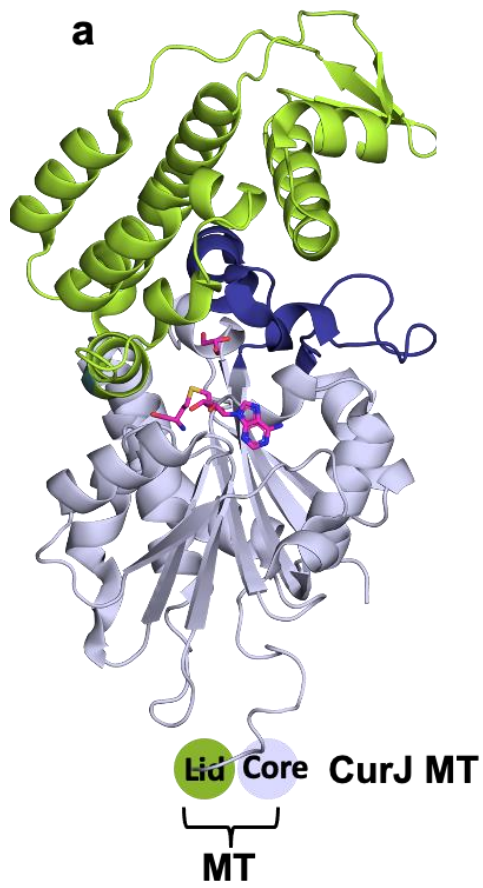


Figure 2.7. Comparison of structures of SxtA and CurJ MTs

(a) Tertiary structure of CurJ MT complex with SAH (PDB: 5THZ). The structure is colored by the domain (lime MT lid, silver MT core). Insertions that form the metal site and substrate tunnel in SxtA (residues 449-466) and CurJ (residues 307 – 344) are colored blue. (b) Tertiary structure of SxtA complex with SAH and Mn^{2+} . It is colored by the sub-domain of origin as in **Figure 2.3**. (c) Superimposition of CurJ and SxtA core domains (RMSD = 3.4 Å). (d) The His-Glu dyad (SxtA 372 and Glu 434 and CurJ His280 and Glu306) are conserved in both MTs. The helical insertion in SxtA MT core contain 2 metal coordinating residues (two glutamines) while CurJ has a lysine and a tryptophan at the corresponding positions. SxtA amino acids are labeled in orange and CurJ amino acids are labeled in blue.

2.3.3 Structural of SxtA MT-DC variant F458H

Later, a 2.1 Å SxtA MT-DC F458H structure (more details about this variant in chapter 3) with Mn^{2+} and malonate was determined in a new crystal form (**Figure 2.8a and Table 1**). The sub-domain linker was ordered in these crystals, providing a complete view of the MT active site. In this structure, the inactive analogue of malonyl-ACP, malonate, binds to the metal ion as a bidentate ligand and replaces two water molecules. One malonate carboxyl group hydrogen-bonds with Mn^{2+} ligand Gln464 and represents the terminus of the Mal-ACP, and the other carboxylate is in the position of the ACP Ppant. Full-length SxtA MT-DC F458H (residue 1-710) protein was used for crystallization; however, the crystallized polypeptide was shorter (**Figure 2.8**), potentially due to hydrolysis by a protease contaminant. In this crystal structure, no clear electron density was visible beyond residue 638. The F458H structure, with Mn^{2+} and malonate, provides detailed information about the substrate-protein interaction and, together with the apo enzyme structure, allows us to view the MT in two different enzymatic states.

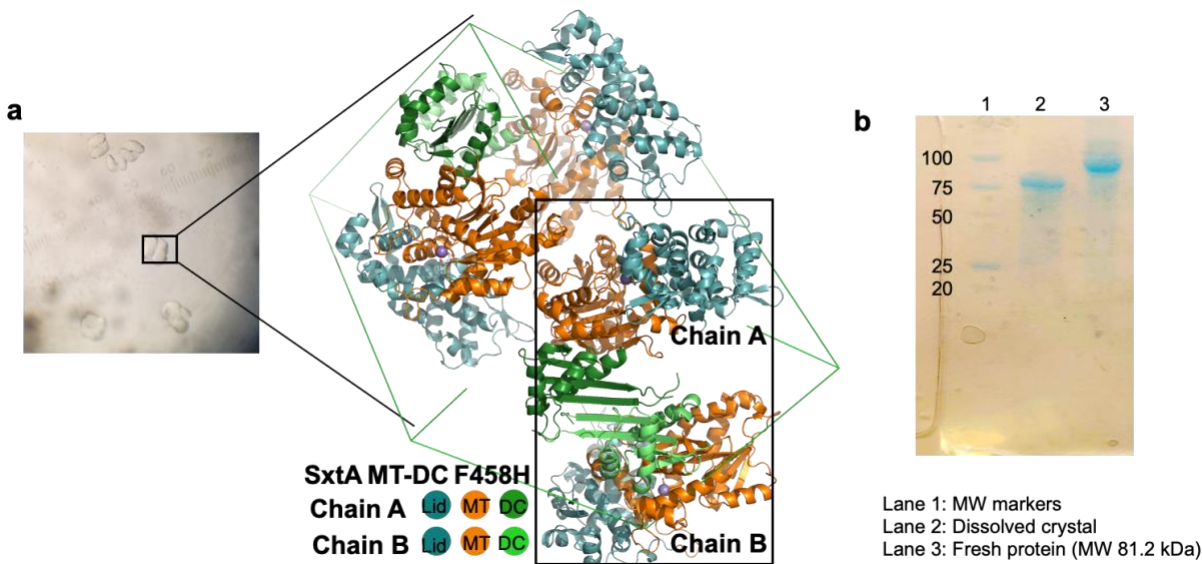


Figure 2.8. SxtA MT-DC F458H crystals

(a) SxtA MT-DC F458H di-domain was crystallized with two molecules in the asymmetric unit (marked by chains A and B). Two polypeptides form a dimer via a truncated DC domain. The structure is colored by the sub-domain of origin, as in Figure 3.3. The green box represents the unit cell. (b) SDS-PAGE analysis of a dissolved SxtA MT-DC F458H crystal and fresh SxtA MT-DC F458H. The crystallized protein was degraded during the 2 weeks of crystallization.

2.3.4 The pre-catalytic and substrate-bound conformations in PKS starter C-MTs

Comparison of the highly similar SxtA MT and AprA MT1 structures (RMSD = 1.4 Å) in complex with various combinations of substrates and cofactors has revealed two conformations of the starter PKS MTs: pre-catalytic and substrate-bound (**Figure 2.9**). The structures of metal-free AprA MT1-ΨDC and SxtA MT-DC with Mn²⁺ and SAH exhibit pre-catalytic conformation (**Figure 2.9 a, b**). This conformation is marked by the characteristics of a disordered sub-domain linker and pi-pi interaction (centroid distance: 3.7 Å) between SxtA Phe458 and Tyr208 (AprA Tyr455 and Tyr206). The disordered sub-domain linker causes the homocysteine group of SAM to be solvent-exposed and disordered. The substrate-bound conformation was identified in the structures of metal-bound AprA MT1-ΨDC and SxtA MT-DC F458H complex with Mn²⁺ and malonate (**Figure 2.9 c, d**). In AprA MT1-ΨDC, the bound

metal facilitated this conformational change by coordinating to His456, thus breaking the pi-pi interaction of the nearby Tyr455 with Tyr206. The di-domain linker is ordered in this conformation, and SAM in AprA MT1- ΨDC is protected and shows decent density around the methionine portion. The driver of conformational change in SxtA MT was not identified as many possibilities such as a different crystal form, additional malonate binding, and the F458H substitution can lead to that shift. SxA His458 (AprA Tyr455) may be a catalytic or substrate binding residue. In the substrate-bound conformation, SxA His458 (AprA Tyr455) no longer participated in the restrictive pi-pi interaction with SxtATyr208 (AprA Tyr206), instead, it points toward the malonate. The di-domain linker controls the access to the active site and becomes ordered upon substrate binding to protect SAM from hydrolysis and enhance acyl-ACP binding.

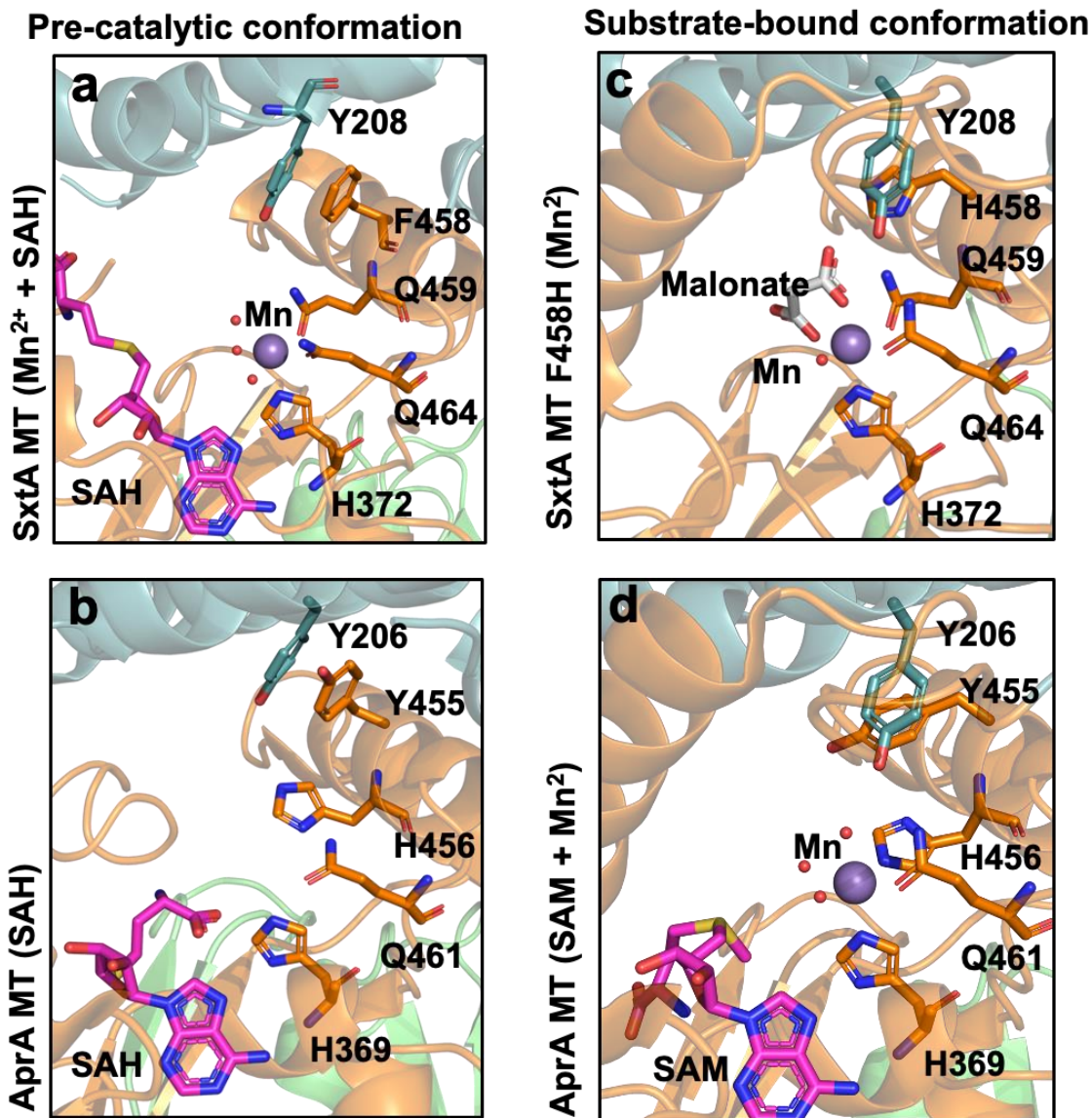


Figure 2.9. Pre-catalytic and substrate-bound conformations in SxtA and AprA MT1. Active site of (a) SxtA MT with Mn²⁺ and SAH, (b,d) AprA MT1, and (c) SxtA MT F458H. Select amino acids (AprA Y206, H369, Y455, H456, and Q461; SxtA Y208, H372, F/H458, Q459, and H464), malonate, and SAH/SAM are shown in sticks with atomic coloring (red O, blue N, yellow S, orange C). Metal coordination bonds are shown as black solid lines.

Table 2.1. Collection and refinement statistics of SxtA MT-DC and its variant F458H crystallographic data.

| | SxtA MT-DC | SxtA MT-DC F458H |
|--------------------------------------|----------------------------|-----------------------------|
| Ligands | Mn ²⁺ | Mn ²⁺ |
| | SAH | |
| | | malonate |
| Data Collection | | |
| Space group | <i>P</i> 1 | <i>P</i> 2 ₁ |
| Unit cell, a,b,c (Å) | 43.8, 69.7, 127.6 | 78.6, 83.79, 117.8 |
| Unit cell, α,β,γ (°) | 86.3, 83.2, 84.0 | 90, 103.1, 90 |
| X-ray source | APS 23ID-B | APS 23ID-B |
| Wavelength (Å) | 1.033 | 1.033 |
| d _{min} (Å) | 2.6 | 2.1 |
| R _{merge} | 0.126 (0.921) ^a | 0.105 (1.355) |
| Avg I/σ(I) | 8.6 (1.4) | 10.9 (1.4) |
| Completeness (%) | 98.0 (97.4) | 98.3 (92.8) |
| Multiplicity | 3.6 (3.5) | 6.9 (6.6) |
| Total observations | 160,449 (15,071) | 597,275 (54,134) |
| Wilson B factor (Å ²) | 51.4 | 46.5 |
| CC _{1/2} | 0.995 (0.695) | 0.997 (0.756) |
| CC* | 0.999 (0.906) | 0.999 (0.928) |

| Refinement | | |
|--|-----------|-----------|
| Data range (Å) | 42.4-2.6 | 47.3-2.1 |
| Reflections (#) | 44,752 | 86,787 |
| R _{work} /R _{free} (%) | 23.8/29.8 | 20.6/23.9 |
| Nonhydrogen atoms (#) | 10,882 | 10,088 |
| protein | 10,787 | 9,832 |
| ligands | 16 | 16 |
| water | 87 | 240 |
| Amino acid residues | 1,358 | 1,232 |
| Deviation from ideality | | |
| bond lengths (Å) | 0.003 | 0.009 |
| bond angles (°) | 0.65 | 1.03 |
| Average B-factor (Å ²) | 64.8 | 52.3 |
| protein | 64.9 | 52.3 |
| ligands | 52.6 | 42.4 |
| solvent | 49.2 | 52.6 |
| Ramachandran plot | | |
| favored (%) | 95.4 | 96.4 |
| allowed (%) | 4.4 | 3.2 |
| outliers (%) | 0.2 | 0.4 |
| PDB code | 7UCI | 7UCL |

^a Values in parentheses pertain to the outermost shell of data.

2.4 Conclusion

The comparison of the starter SxtA MT and extender CurJ MT structures revealed features that make these two types of PKS C-MTs different from each other. High sequence and structural variation within their helical insertion distinguishes the biochemical mechanisms, substrate scope, and cofactor requirement (starter C-MTs require metal ions) among starter and extender MTs. Identification of these features may not only improve the annotation of MTs from sequences but also help determine the catalytic condition required for these enzymes. In addition, structural analysis of SxtA MT-DC, SxtA F458H, and AprA MT1-ΨDC helped us explore the conformational changes in starter MT associated with substrate binding. The flexible di-domain linker controls the access of the catalytic pocket and becomes ordered upon substrate binding to trap intermediates and protect SAM from hydrolysis. In addition, a few residues within the active site, such as SxtA F458 and Y208 (AprA Y455 and Y206), reorientate themselves for an optimal reaction condition SAM from hydrolysis.

2.5 Materials and methods

2.5.1 Construct design

All PCR primers are listed in **Table 2**. pMCSG7-*SxtA_1_721* (SxtA MT-DC residues 1-721) was amplified from *sxtA* (GenBank accession code). Constructs encoding SxtA MT-DC were inserted into pMCSG7 by ligation independent cloning (LIC) to generate pMCSG7-*SxtA_1_721*. For a truncated SxtA MT-DC (residues 1–710), pMCSG7-*SxtA_1_710* was sub-cloned using primers in **Table 2.2**. Site-directed mutagenesis F458H was done via QuikChange (Agilent) using primers in **Table 2.2**.

Table 2.2. Primers used for ligation-independent cloning and site directed mutagenesis.

| Name | Vector | Primer |
|--------------------|--------|---|
| SxtA 1_710 Forward | pMSG7 | TACTTCCAATCCAATGCAATGTTACAAAAGATTA ATCG |
| SxtA 1_710 Reverse | | TTATCCACTTCCAATGCTACGAGTGCAAAGCACT GTCGCGCA |
| SxtA_F458H_Forward | pMSG7 | CGAAAACCTTACATTTTCGATGCGCATCAGGGATTTT CTCAGCAGTAT |
| SxtA_F458H_Reverse | | ATACTGCTGAGAAAATCCCTGATGCGCATCGAAAT GTAAGTTTTTCG |

Overhangs for LIC are bolded.

2.5.2 Bacterial expression and purification

All plasmids were transformed into *Escherichia coli* strain BL21(DE3). Cell cultures were grown at 37 °C in 0.5 L Terrific Broth (TB) with 100 µg mL⁻¹ ampicillin until OD₆₀₀ reached 1–2, then cooled to 20°C over 0.5–1 hr, induced with 200 µM IPTG, and grown overnight. Cell pellets from 0.5 L cultures were resuspended in 35 mL Buffer A (50 mM Tris pH 7.4, 300 mM NaCl, 10% (v/v) glycerol) with 0.1 mg mL⁻¹ lysozyme, 0.05 mg mL⁻¹ DNase, 2 mM MgCl₂, 20 mM imidazole. Resuspended cells were incubated on ice for 30 min, lysed by sonication, and centrifuged at 38,650 x g, for 20 min. The soluble fraction was then filtered through a 0.45 µm MILLEX-HP membrane and loaded onto a 5 mL His trap column (cytiva) pre-equilibrated with Buffer A. The column was washed with 50 mL Buffer A and eluted with a 50 mL gradient of 20–400 mM imidazole in Buffer A. For SxtA MT-DC, the N-terminal His tag

was removed by overnight dialysis in Buffer A at 4°C in the presence of tobacco etch virus (TEV) protease⁸³ and 2–5 mM dithiothreitol (DTT) at a 50:1 molar ratio of MT-DC:protease. The mixture was reapplied to the His-trap column to remove uncleaved MT-DC and the protease. SxtA MT-DC was further purified via HiLoad Superdex S200 or S75 (Cytiva) gel filtration chromatography with Buffer B (50 mM Tris pH 7.4, 50 mM NaCl, 10% (v/v) glycerol). The SxtA MT-DC eluted as a monomer with apparent molecular weight 80 kDa. The purified SxtA MT-DC was concentrated to 12–14 mg mL⁻¹ and stored in aliquots at –80°C.

2.5.3 Protein crystallization and structure determination

Tag-free SxtA MT-DC (residues 1–710) was crystallized at 4°C by vapor diffusion in a 1:1 mixture of protein stock (12 – 14 mg mL⁻¹ in Buffer B with 5 mM *S*-adenosylmethionine (SAM), 5 mM MnCl₂) and well solution (5–8% polyethylene glycol (PEG) 20K, 0.1 M MES pH 6.25–6.5). Crystals were cryo-protected by a 5-min soak in cryo-solution (20% 1,2-propanediol, 0.1 M MES pH 6.5, 5 mM MnCl₂, 5 mM SAM and 10% PEG 20K), then harvested and stored in liquid nitrogen. Diffraction data were collected at the Advanced Photon Source (APS) beamline 23ID-B (GM/CA@APS) and processed using XDS⁸⁴. The structure (space group *P*1 with two polypeptides in the asymmetric unit) was solved by molecular replacement from the structures of CurA DC (PDB 2REE⁵⁸) and AprA MT1 (PDB 6B3A²) using Phaser⁸⁵ in the Phenix software suite⁸⁶. The SxtA MT-DC structure was built using *Coot*⁸⁷, and the model was refined with phenix.refine⁸⁶. The model is nearly complete, including a few cloning-artifact residues. A few regions were disordered and are not included in the model (228–249 and 706–710 in chain A; 149–159, 181–186, 228–248 and 706–710 in chain B). Wild type SxtA MT-DC formed mosaic crystals with limited reproducibility. Due to crystal packing, density was stronger for chain A than chain B (mean B-factor 61.7 Å² for chain A, 71.3 Å² for chain B). Electron density for chain

B residues 268–390 was weak, so we built this region from the corresponding region of chain A and retained the side chains. TLS groups for refinement were: in chain A, N-terminus through 189, 190–267, 268–530, 531–705; in chain B, N-terminus through 252 and 253–705.

Tag-free SxtA MT-DC F458H (residues 1–721) was crystallized at 20°C by vapor diffusion from a 1:1 mixture of protein stock (12–14 mg/mL in Buffer B with 5 mM SAM, 2 mM sodium malonate, 5 mM (*R*)-pantetheine, 5 mM MnCl₂) and well solution (18% PEG 3350, 0.16 M Li₂SO₄, 0.1 M Bis-Tris pH 6.5). Crystals were cryo-protected by 5-min soak in cryo-solution (32% PEG 3350, 0.2 M Li₂SO₄, 0.1 M Tris pH 7), then harvested and stored in liquid nitrogen. Diffraction data were collected at beamline 23ID-B (GM/CA@APS) and processed using XDS. The structure (space group *P*2₁ with two polypeptides in the asymmetric unit) was solved by molecular replacement from the SxtA MT-DC structure using Phaser. Model building was done with *Coot* and refinement with phenix.refine. Electron density was complete for the MT domain, including the 228–249 loop near the active site. However, in the DC domain, residues 574–588 were disordered, and the map had no density for the C-terminus (residues 627–710 in chain A and 628–710 in chain B). SDS-PAGE analysis of dissolved crystals and protein stock showed that the crystallized protein was truncated, apparently due to proteolysis during the 14 days of crystal growth (**Figure 3.7**).

Chapter 3 Structural Basis of Methylation Control in Polyketide Synthase C-methyltransferase

Partially reproduced with permission from Lao, Y.; Skiba, M. A.; Chun, S. W.; Narayan, A. R. H.; Smith, J. L. (2022) Structural Basis for Control of Methylation Extent in Polyketide Synthase Metal-Dependent C-Methyltransferases. *ACS Chem Biol*. Copyright 2022 American Chemical Society.

3.1 Summary

A biocatalyst to perform site- and stereoselective methylation is valuable for many industrial and medical applications. The metal- and *S*-adenosyl-methionine (SAM) dependent starter methyltransferases (MTs) from different biosynthesis pathways can either monomethylate or dimethylate the malonyl-ACP substrates. Further investigation into the structures of MTs from natural product biosynthesis pathways helped identify potential features that determine the degree of methylation. Possible features were tested through mutagenesis followed by (liquid chromatography-mass spectrometry) LC-MC-based biochemical assay. The SxtA monomethyltransferase was converted to a dimethyltransferase by modification of the metal binding site, the addition of an active site base, and an amino acid substitution to provide space in the substrate pocket for two methyl substituents. A reciprocal change converted a related dimethyltransferase into a monomethyltransferase, supporting our hypothesis that steric hindrance can prevent a second methylation event. A novel understanding of MTs will accelerate the development of MT-based catalysts and MT engineering for use in small-molecule synthesis.

3.2 Introduction

3.2.1 *The magic methyl effect*

Methylation is a widely used modification in drug discovery due to the so-called "magic methyl effect"^{67, 68} that can boost drug potency up to 2000-fold. A simple methyl group can modulate many properties of a drug molecule. For instance, ibufenac is associated with high rates of idiosyncratic hepatotoxicity, while ibuprofen, which differs from ibufenac by only one methyl group, is among the most effective and widely used non-steroidal anti-inflammatory drugs⁸⁸. As a result of the additional methyl substituent, ibuprofen has slower acyl glucuronide migration, reduced toxicity, and increased half-life relative to ibufenac⁸⁹. Methyltransferases involved in natural product biosynthesis accomplish selective installation, sometimes even on various substrates⁷⁰. Thus, biocatalytic approaches may be valuable, particularly for methylations where de novo synthesis or deconstruction and re-assembly are impractical. C-methyltransferases (C-MT) in polyketide synthase (PKS) pathways are potential tools for this purpose. Modular type I PKSs generate bioactive natural products through successive elongation and tailoring reactions using malonyl- (Mal-) or methylmalonyl- (MeMal-) coenzyme A (CoA) building blocks^{75, 76}. C-MTs within PKS pathways can be useful methylation tools because they selectively perform one or two methylation reactions under mild conditions and achieve high site- and stereo-selectivity^{66, 74, 42, 44, 70}.

3.2.2 *The medicinal potential of saxitoxin*

Saxitoxin (STX), a paralytic shellfish toxin produced by freshwater cyanobacteria and marine dinoflagellates, is one of the most potent naturally occurring neurotoxic alkaloids known⁹⁰. The positively charged guanidium groups of STX interact with negatively charged

amino acids in domains I and II of voltage-gated sodium channels^{91, 92}, causing tissue-specific paralysis^{93, 91, 94}. SXT derivatives have the potential for development as selective neuropathic pain treatments⁹⁵ directed to voltage-gated channels. However, the STX biosynthetic pathway has not been fully exploited despite considerable biochemical study^{66, 96-101}. Barriers to a synthetic biology approach include lack of an effective heterologous host and limited access to analogs¹⁰². Thus, modification of saxitoxin to generate analogs would benefit from the chemoenzymatic approach¹⁰³

3.2.3 The starter module of the saxitoxin biosynthesis pathway

STX biosynthesis is initiated by a PKS-like loading module, SxtA (**Figure 3.1**), which includes a rare Mn²⁺-dependent C-MT domain for monomethylation of malonyl-acyl carrier protein (Mal-ACP) to generate methylmalonyl (MeMal)-ACP^{66, 80}. Following the SxtA MT reaction, a SxtA decarboxylase (DC) domain converts MeMal-ACP to propionyl-ACP, the starter unit for STX biosynthesis^{66, 80}. SxtA DC is a member of the GCN5-related N-acetyltransferase (GNAT) superfamily, which includes predominantly acyltransferases and a few decarboxylases. Like the GNAT superfamily enzymes in the biosynthesis pathways for curacin A (CurA DC) and gephyronic acid (GphF DC), SxtA DC catalyzes only decarboxylation^{58, 51}. Skiba et al. previously characterized the activity and structure of a related metal-dependent C-MT, AprA MT1, an S-adenosylmethionine (SAM) and Fe³⁺-dependent dimethyltransferase⁴⁴. AprA MT1 is followed by an MT2 domain that catalyzes a third methyl transfer coupled to decarboxylation to afford the pivaloyl-ACP starter unit for apratoxin A biosynthesis⁴³. An AprA pseudo-decarboxylase (ΨDC) located between MT1 and MT2 lacks catalytic activity. Despite their highly similar sequences (54% identity), SxtA MT and AprA MT1 differ in their metal selectivity (Mn²⁺ and Fe³⁺, respectively) and extent of methylation (one and two methyl

transfers, respectively)⁴⁴. In the present study, we characterized the activity of the SxtA MT. Comparison of SxtA MT and AprA MT1 uncovered features that determine the selectivity of each enzyme for transfer of one or two methyl groups. The critical discovery was an amino acid side chain in the substrate pocket that provides a steric block to a second methyl transfer. We then engineered the SxtA MT-DC didomain to transfer two methyl groups and the AprA MT1-ΨDC to transfer a single methyl group. These results provide critical insights into engineering related C-MTs for functionalization of drug scaffolds.

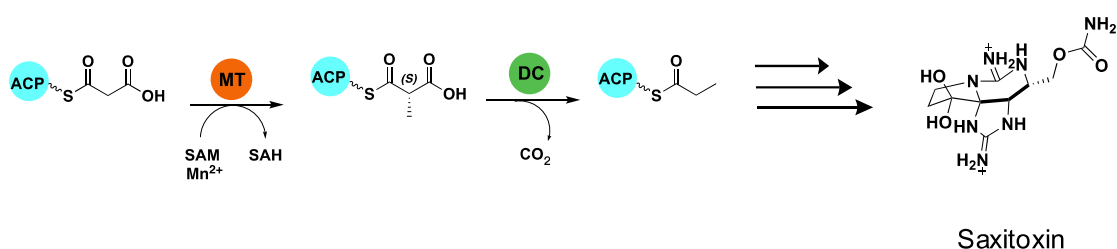


Figure 3.1. Reaction scheme of SxtA MT and DC domains in saxitoxin biosynthesis.

The product of the SxtA MT and TaI MT is inferred to be (S)-methylmalonyl-ACP, based on the structures of AprA MT1 substrate complexes¹².

3.3 Results and Discussion

3.3.1 Catalytic activities of SxtA MT-DC

The methylation and decarboxylation activities of wild type SxtA MT-DC were investigated (**Figure 3.2a–b**). We first identified the boundaries of the SxtA methyltransferase (MT, residues 1–506) and decarboxylase (DC, residues 512–710) domains by reference to a multiple sequence alignment and crystal structures of the AprA MT1^{66, 44}, CurA DC⁵⁸ and GphF DC⁵¹. We produced the recombinant SxtA MT-DC didomain (1–721) for biochemical study, as the excised MT domain was unstable without the DC. The AprA ACP domain was used to deliver substrates, as the excised SxtA ACP domain was unstable. The ACP was loaded with a

malonyl (Mal) or methylmalonyl (MeMal) group via a non-specific phosphopantetheinyl transferase^{104, 105}. The MT and DC catalytic activities were assayed by monitoring the distribution of acyl-ACP species using liquid chromatography-mass spectrometry (LC-MS) with quantification of ACP-bound species using a phosphopantethine (Ppant) ejection assay¹⁰⁶. SAM-dependent methylation of Mal-ACP was dependent on added metal. The MT exhibited a strong Mn^{2+} preference, with 10-fold greater methylation under our assay conditions relative to Fe^{3+} (**Figure 3.2a**). A metal-free enzyme that cannot catalyze methyl transfer was used to evaluate the substrate selectivity of the SxtA DC with Mal-ACP or MeMal-ACP. SxtA DC decarboxylated MeMal-ACP but had no detectable activity with Mal-ACP (**Figure 3.2b**). In accord with the chemical structure of saxitoxin, SxtA MT-DC produced no detectable dimethylation products: dimethylmalonyl- (Me_2Mal -) ACP or its decarboxylated product isobutyryl-ACP. To simplify the analysis of SxtA methylation activity, we eliminated decarboxylation activity by producing SxtA MT-DC T637V; Thr637 is analogous to the catalytic Thr in the CurA DC⁵⁸. We confirmed that MT-DC T637V lacked decarboxylation activity (**Figure 3.2b**), as previously reported,⁶⁶ but retained methylation activity ($79\pm 12\%$ in the standard assay) similar to the wild type MT-DC ($85\pm 8\%$) (**Figure 3.2a**). To facilitate quantitative comparison of methylation reactions, we determined assay conditions (time, temperature, and concentration) in which the wild type enzyme methylated most of the Mal-ACP substrate ($\sim 85\%$). All comparative assays of wild type and mutagenized MT were performed identically under these conditions.

Analysis of the MT active site structures did not lead to an obvious mechanism for control of the extent of methylation by the monomethylating SxtA MT-DC and dimethylating AprA MT1- Ψ DC (**Figure 3.2 c-e**). The active site structures are highly similar (RMSD = 1.4 Å), but sequence differences in and near the active site may contribute to this functional divergence.

We used site-directed mutagenesis to investigate several features of the SxtA MT-DC structure that differ from AprA MT1-ΨDC. These features include the presence of an active DC domain in SxtA MT- DC, metal selectivity, and metal coordination sphere (**Figure 3.3**).

3.3.2 The active SxtA DC may restrain the methylation extent by SxtA MT

The SxtA DC includes a complete DC domain, in which Thr637 and His671 are the catalytic residues by analogy to CurA DC⁵⁸. DCs in PKS loading modules may function as gatekeepers by selectively acting on acyl-ACPs to generate starter units specific to the corresponding biosynthetic pathways: SxtA DC acts on MeMal-ACP (**Figure 3.2b**), CurA DC decarboxylates on Mal-ACP⁵⁸, and GphF DC on Me₂Mal-ACP⁵¹. The SxtA DC domain may restrict the SxtA MT to a single methyl transfer by decarboxylating MeMal-ACP more rapidly than the MT can exchange SAH for SAM and catalyze a second methyl transfer. To investigate this possibility, we determined the extent of methylation by the DC-inactive SxtA T637V variant. This substitution eliminated decarboxylation activity, created a variant with methyl transfer activity equivalent to the wild type (**Figure 3.2b**), but led to no detectable dimethylation activity.

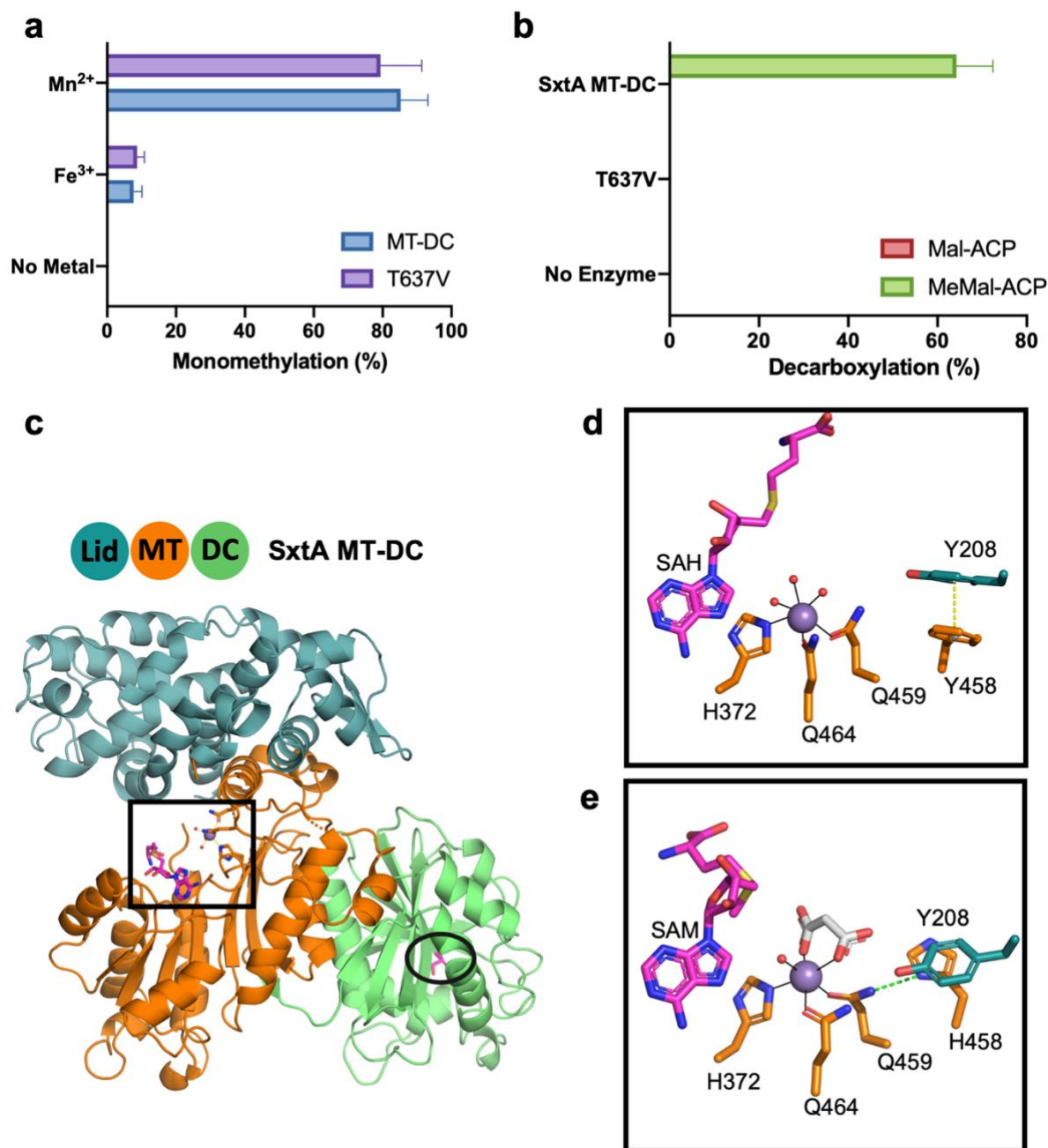


Figure 3.2. SxtA MT-DC catalysis and structure.

(a) SxtA MT-DC wild type and T637V methylation with added Mn²⁺, Fe³⁺, and no-metal control. Monomethylation was quantitated as a percent of total Mal-ACP substrate converted to methylated products; no dimethylation products were detected. (b) SxtA MT-DC wild type and T637V decarboxylation with Mal-ACP and MeMal-ACP substrates. Decarboxylation was quantitated as percent of total Mal-ACP or MeMal-ACP substrate converted to acetyl- or propionyl-ACP. Error bars represent the standard deviation of >5 experiments. (c) Didomain ternary complex with Mn²⁺ (purple), SAH, and Thr637 (magenta C) with domain coloring (blue MT lid, orange MT core, green DC). Active sites are boxed (MT) and circled (DC) in stick form (red O, blue N, yellow S). (d) SxtA MT active site with stacked Phe458 and Tyr208. SAH homocysteine is modeled; side chain C colored by the domain of origin; waters in red. (e) MT active site of SxtA F458H. Malonate (white C) replaces two water ligands; SAM is modeled. His458 is hydrogen bonded to Gln459 ligand (dashed line).

transferred to a substrate may also be determined by the metal ion and its ligand sphere. SxtA MT is strongly selective for Mn^{2+} (**Figure 3.2a**), whereas AprA MT1 preferred Fe^{3+} and had weak activity with Mn^{2+} and other divalent metal ions⁴⁴. Moreover, AprA MT1 dimethylation was Fe^{3+} dependent. Fe^{2+} supported only one methyl transfer, leading to the hypothesis that the more energetically challenging second methyl transfer may require the stronger Lewis acid of a trivalent metal ion due to the higher pK_a of the MeMal-ACP α proton compared to Mal-ACP¹⁰⁷.⁴⁴. The differing metal selectivity may result from different ligand spheres in SxtA MT, AprA MT1 and GphF MT (**Figure 3.3b**). In SxtA MT, the Mn^{2+} has two glutamine ligands (464 and 459) and one histidine (372), whereas the metal sites in AprA and GphF MTs have one glutamine ligand and two histidines, perhaps accounting for the different extent of methylation.

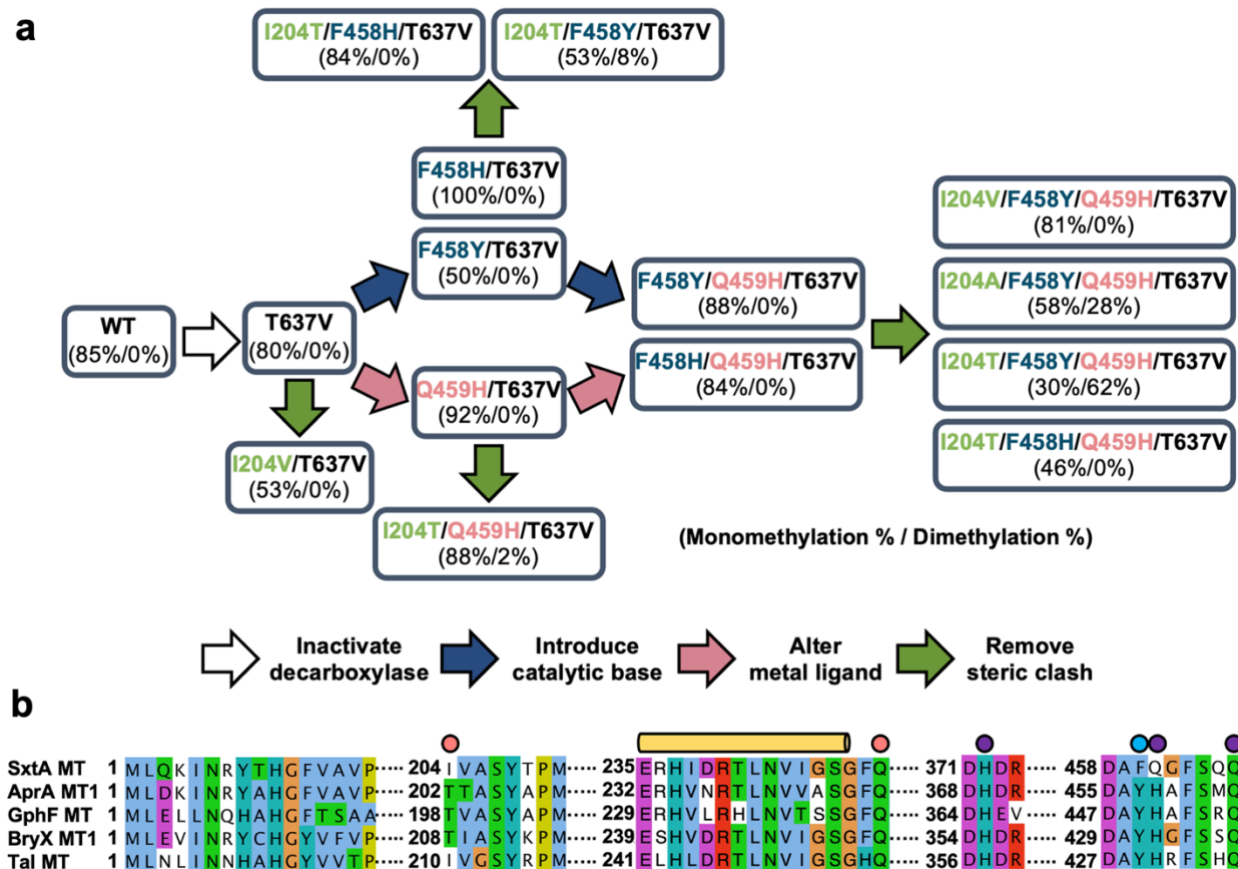


Figure 3.3 SxtA mutagenesis approaches and multiple sequence alignment of key MT regions.

(a) Schematic of SxtA MT-DC site-directed mutagenesis. Mn^{2+} -dependent activity of each variant is indicated (% monomethylation / % dimethylation) for reactions in the standard assay condition. (b) Sequence alignment of loading-module MTs in pathways with identified natural products. The proteins (natural product, GenBank accession) are SxtA (saxitoxin, WP_009343302.1), AprA MT1 (apratoxin A, WP_075900460), GphF MT (gephyronic acid, KF479198.1), BryX MT1 (bryostatin, ABK51302.1), and Tal MT (myxovirescin A, WP_011553948.1). SxtA Ile204 and Gln250 in the active site pocket are indicated with a pink circle; Phe458, which was mutagenized to His and Tyr, by a blue circle; and metal ligands by purple circles. The disordered SxtA MT lid-core linker is highlighted with a long yellow cylinder.

3.3.3 Effect of bound metal in the SxtA MT active site

To test this hypothesis, we mutagenized the ligand sphere in SxtA by creating two variants (Q459H and Q459H/T637V) that mimic the AprA Fe^{3+} site. However, SxtA Q459H and Q459H/T637V had Mn^{2+} -dependent methyl transfer activity similar to SxtA wild type and SxtA T637V, respectively, and we detected no dimethylated products (**Figure 3.4a**). Interestingly, the alteration of ligands from 2 Gln / 1 His to 1 Gln / 2 His substantially increased the Fe^{3+} -dependent activity by six-fold relative to levels for the SxtA wild type and by three-fold for SxtA T637V (**Figure 3.4b**). Nevertheless, the Q459H substitution did not alter the SxtA MT preference for Mn^{2+} .

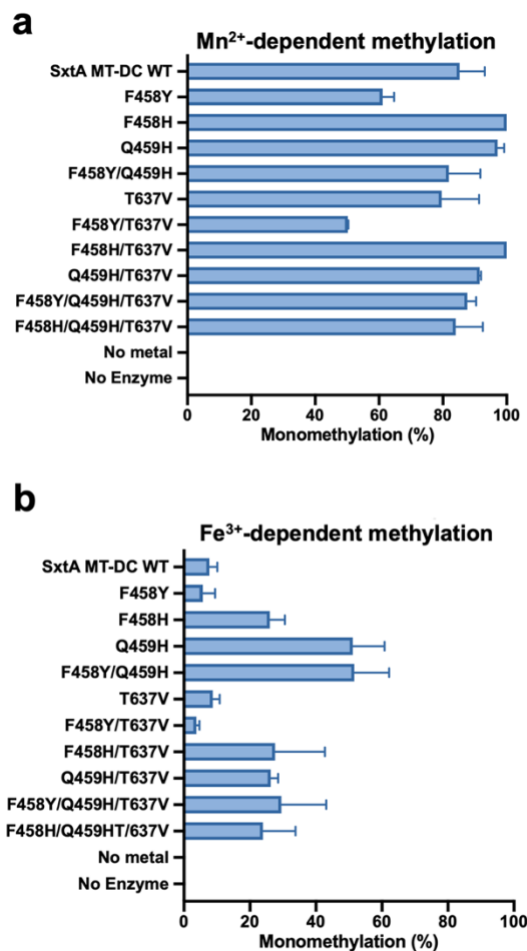


Figure 3.4 Methylation activity of SxtA MT-DC variants.

(a) Mn²⁺-dependent activity. (b) Fe³⁺-dependent activity. Methylation is quantitated as the percent of input Mal-ACP converted to monomethylated products (sum of Ppant ejection fragments from MeMal-ACP and propionyl-ACP). Dimethylated products were not detected for any variant. Error bars represent standard deviation of four or more experiments.

3.3.4 A catalytic base for dimethylation

Another difference in the SxtA MT and AprA MT1 active sites is Phe458 in SxtA in place of Tyr455 in AprA MT1 (**Figure 3.2d, e; 3.3b**). We previously showed that the second methyl transfer reaction of AprA MT1 was nearly abolished by substitution of Phe for Tyr455⁴⁴, which is positioned toward the Mal- and MeMal-ACP and may act as a catalytic base for the

second methyl transfer. Thus, we substituted Tyr or His for Phe458 in SxtA MT-DC; however, no variants with these substitutions catalyzed dimethylation. SxtA MT-DC F458Y, F458Y/T637V, F458H and F458H/T637V, under standard assay conditions, yielded 61±4%, 50±0.2%, 100%, and 100% monomethylated products, respectively, with Mn²⁺ (**Figure 3.4a**). With Fe³⁺, yields were 6±4%, 4 ±1%, 26±5%, and 28±15% mono-methylated products, respectively (**Figure 3.4b**). Interestingly, the F458H substitution led to increased product yield over the wild-type and consumed all the Mal-ACP substrate in the standard Mn²⁺-dependent reaction; this substitution also increased the yield for the Fe³⁺-dependent reaction. We also combined the substitutions at position 458 with the more efficient Q459H substitution (F458Y/Q459H, F458H/Q459H, F458Y/Q459H/T637V, and F458H/Q459H/T637V). These variants generated only monomethylated products, despite having all the features proposed to support two methylation reactions.

3.3.5 The F458H substitution increases monomethylation efficiency

Although no dimethylated products were detected under our standard reaction conditions, the SxtA F458H variants consumed all of the Mal-ACP substrate, whereas SxtA wild type and T637V converted only 85±8% and 79±12%, respectively. Using SxtA MT-DC T637V to eliminate complications from decarboxylation, we measured the time course of product formation for SxtA F458H/T637V and T637V with a fixed substrate concentration and four-fold less SxtA MT-DC than for the standard assay condition (**Figure 3.5 a, b**). Under these conditions, MT-DC F458H/T637V methylated ~68% of the Mal-ACP substrate while MT-DC T637V converted only ~11%, a sixfold increase. We then quantitated the greater catalytic efficiency of MT-DC F458H/T637V compared to the parent MT-DC T637V using a 1.45 μM enzyme concentration and 38–600 μM Mal-ACP substrate (**Figure 3.5 c, d**). The maximum

attainable Mal-ACP concentration (600 μM) was not saturating for SxtA F458H/T637V, and K_M could not be determined. Using initial velocities at low substrate concentrations, the catalytic efficiency (k_{cat}/K_M) was approximately fourfold greater for SxtA F458H/T637V ($3.17 \text{ mM}^{-1} \text{ min}^{-1}$) than for the SxtA T637V parent ($0.78 \text{ mM}^{-1} \text{ min}^{-1}$).

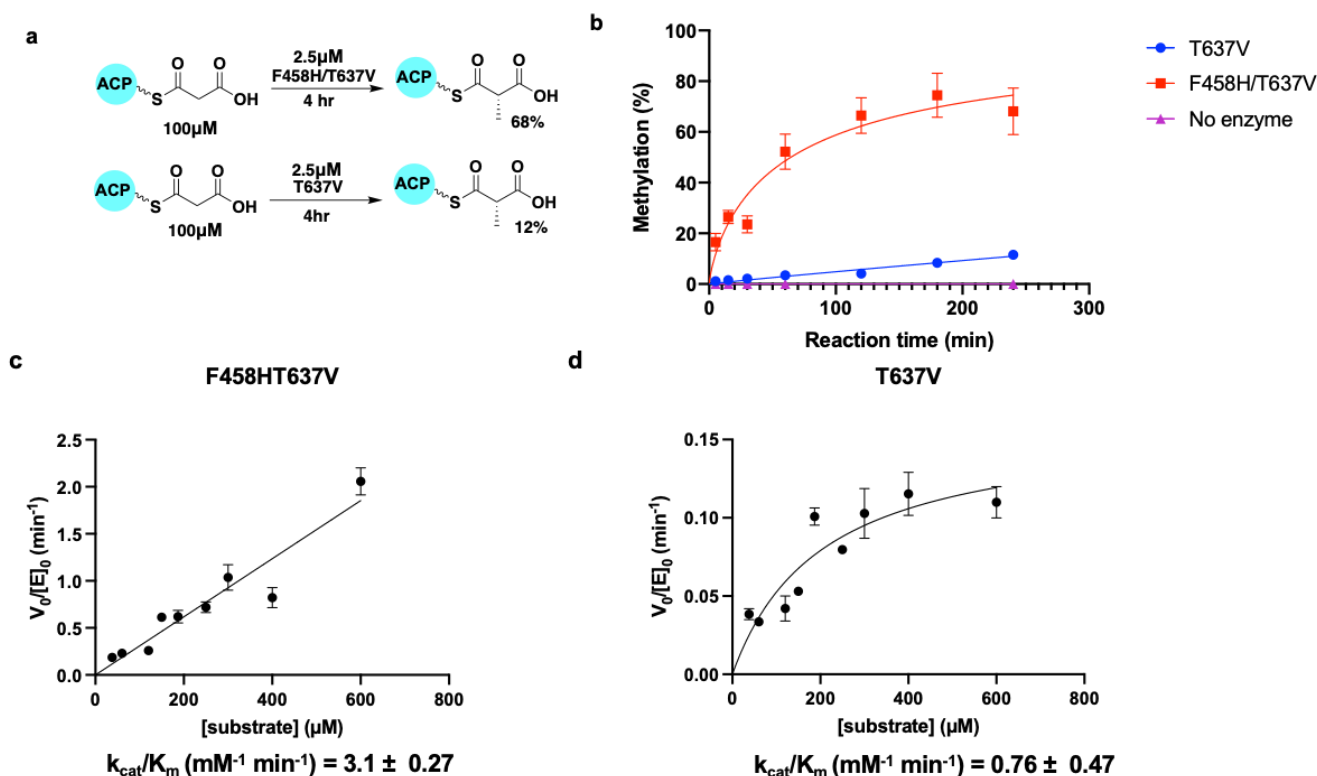


Figure 3.5 Monomethylation rate of SxtA MT-DC F458H/T637V and T637V.

(a) Reaction of SxtA F458H/T637V and T637V on Mal-ACP. (b) Time course of methylation by SxtA F458H/T637V and T637V. SxtA concentration was fourfold lower than for the standard condition in Figure 3.4. Error bars represent the spread of two replicates and are too small to be seen in some cases. Rates of methylated product formation by SxtA MT-DC F458H/T637V (c) and T637V (d) as a function of Mal-ACP concentration (38, 60, 120, 150, 187, 250, 300, 400, or 600 μM). Initial velocity (V_0) with an enzyme concentration of 1.45 μM is based on the conversion of substrate Mal-ACP to methylated species within the linear range of 5-30 min reaction time. Aliquots were analyzed at 5, 15 and 30 min with product detection by LC/MS using Ppant ejection, as described in the 'Methylation kinetic assay' paragraph of Materials and Methods. Error bars represent the variance of three measurements. Catalytic efficiency (k_{cat}/K_M) was determined by fit to the refined Michaelis-Menten equation (Johnson KA, Kinetic Analysis for the New Enzymology, Section 5.9.2, Kin Tek Corp., Austin, TX, 2019).

Based on the crystal structure with the complete SxtA MT active site, we attribute the increased activity of SxtA MT F458H to stabilization of the metal ligand sphere (**Figure 3.2d–e**). In the SxtA MT-DC wild type structure, Phe458 forms a π - π stacking interaction with the Tyr208 side chain (centroid distance 3.7 Å). In the MT active site with His458, the side chain is not stacked with Tyr208, but instead is oriented toward the malonate substrate analog and participates in the secondary metal coordination sphere via a hydrogen bond to the side chain nitrogen of the Gln459 metal ligand (**Figure 3.2e**). His458 is not positioned to interact directly with the substrate. Second-sphere interactions can be important in supporting the active site structure and reactivity of metalloenzymes¹⁰⁸ by stabilizing the metal site or a reaction intermediate, by orienting a ligand, or by mediating the transfer of a proton or electron^{109, 110}. Several other amino acids in the SxtA MT (Tyr208, Asn243, Asp373, Glu434, Phe455 and Ser462) participate in the secondary coordination sphere and are conserved among annotated MTs of this family (**Figure 3.6b**), indicating the important contribution of second-sphere interactions. Here, the SxtA MT F458H structure and kinetic assay results indicate that the enhanced catalytic rate of this variant is due to the His458 hydrogen bond with the metal ligand Gln459, perhaps by stabilizing Gln459 and the metal in an optimal position for malonyl-ACP binding or for catalysis. Interestingly, the His458 substitution had no accelerating effect on a variant where the Gln459 ligand was replaced with His (F458H/Q459H/T637V, **Figure 3.4a**), consistent with the impossibility of a hydrogen bond between His458 and His459 side chains.

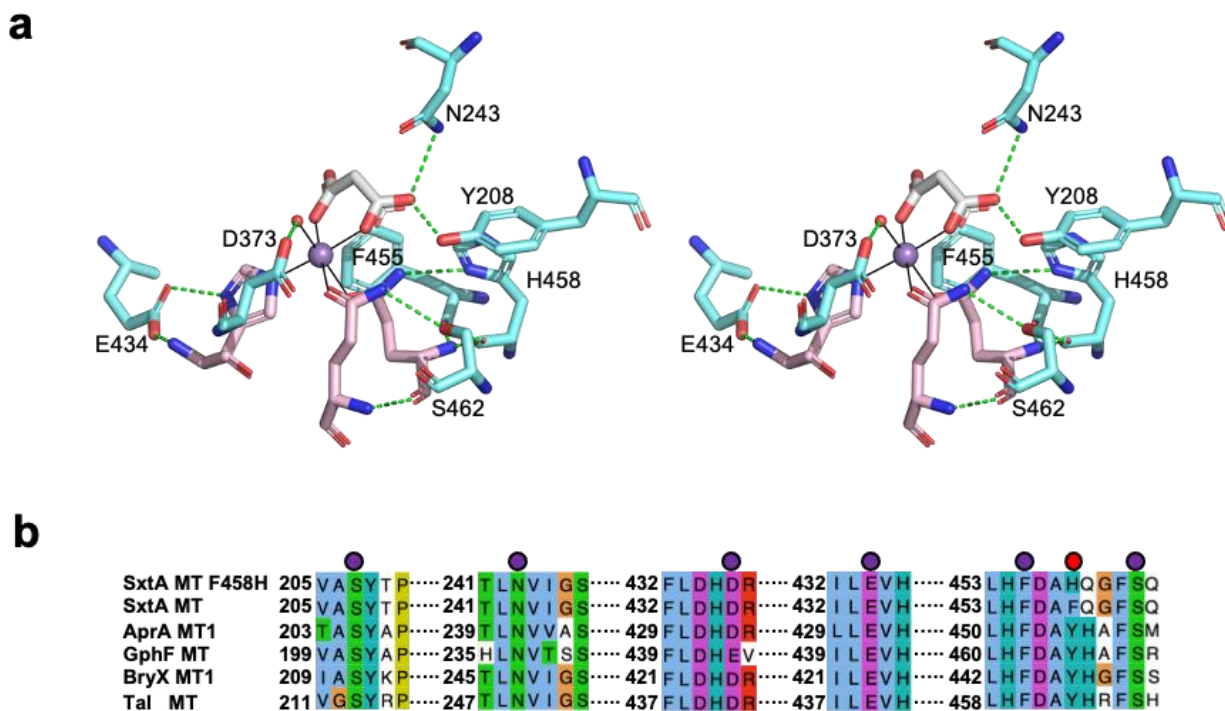


Figure 3.6. Mn²⁺ ligand sphere and second-shell environment.

(a) Stereo-image of the SxtA MT-DC F458H metal site. Details are shown for the metal (purple sphere), protein ligands (pink C), malonate (white C) and second-shell amino acids (cyan C). Metal coordination bonds are depicted as black solid lines and hydrogen bonds as green dashed lines. (b) MT sequence alignment of SxtA MT (saxitoxin, WP_009343302.1) and its F458H variant, AprA MT1 (apratoxin A, WP_075900460), GphF MT (gephyronic acid, KF479198.1), BryX MT1 (bryostatin, ABK51302.1) and Tal MT (myxovirescin A, WP_011553948.1). Residues involved in secondary metal sphere of SxtA are indicated with purple or red circles. SxtA Phe458 subjected to His substitution is marked by a red circle.

3.3.6 Other factors in the extent of methylation

Taken together, the provision of an AprA-like metal center, addition of a putative base for the second methylation reaction, and elimination of any decarboxylation activity were insufficient for SxtA MT to catalyze two methyl transfers. Thus, we re-examined the sequence alignment and the SxtA F458H structure for other features. Among the four SxtA MT homologs with known reaction products, the Tal MT (43% identical sequence to SxtA MT, 48% identity to AprA MT1) is especially interesting. The myxovirescin loading module (Tal MT-DC-ACP)

produces a propionyl starter unit⁷⁹, thus its MT should be a monomethylating enzyme. However, the Tai MT active site is more similar to the dimethylating AprA MT1 than the monomethylating SxtA MT (**Figure 3.3b**). The Tai MT possesses Tyr463 (analogous to SxtA Phe458 and AprA Tyr455) and a metal coordination sphere with two histidine ligands and one glutamine. Like our results with engineered SxtA MT-DC, this suggests that other features of the enzyme control the extent of methylation.

The SxtA MT F458H structure with bound malonate and Mn²⁺ has an ordered sub-domain linker, providing a more complete view of the MT active site. Similar to the ternary complex of AprA MT-ΨDC with malonate and SAM (PDB: 6B3B⁴⁴, the malonate in SxtA displaces two water molecules and is a bidentate Mn²⁺ ligand. We modeled dimethylmalonate into the malonate site of SxtA MT F458H (**Figure 3.7**). Installation of the first methyl group generates *S*-MeMal-ACP, with the *S*-methyl pointed toward the SAM/SAH pocket. A second methyl transfer would occur from the same direction as the first and would displace the first methyl group into the substrate pocket, where a steric clash with Ile204 appears inevitable. In the dimethylating AprA MT1, the analogous residue is Thr202. Moreover, like the SxtA MT, the presumed monomethyltransferase, Tai MT, also has isoleucine at this position whereas the dimethyltransferases (AprA MT1, BryX MT1 and GphF MT) have threonine (**Figure 3.3b**). In crystal structures, SxtA Ile204 and AprA Thr202 are located at a kink in a long and irregular helix (SxtA 189–209; AprA 187–207). We solved a crystal structure of AprA MT-ΨDC with dimethylmalonate and discovered that the Thr202 side chain adopts a different rotameric position than in the malonate complex where it is hydrogen bonded to the Gln248 side chain (**Figure 3.8a, b**). AprA MT1 accommodates two methyl groups with a rotameric position for Thr202 in which the hydroxy group is directed into the helix kink and hydrogen bonded to the backbone

carbonyl of residue 199 (**Figure 3.8b**). This rotameric position is not accessible to SxtA Ile204 (ethyl in lieu of hydroxy) (**Figure 3.8c**).

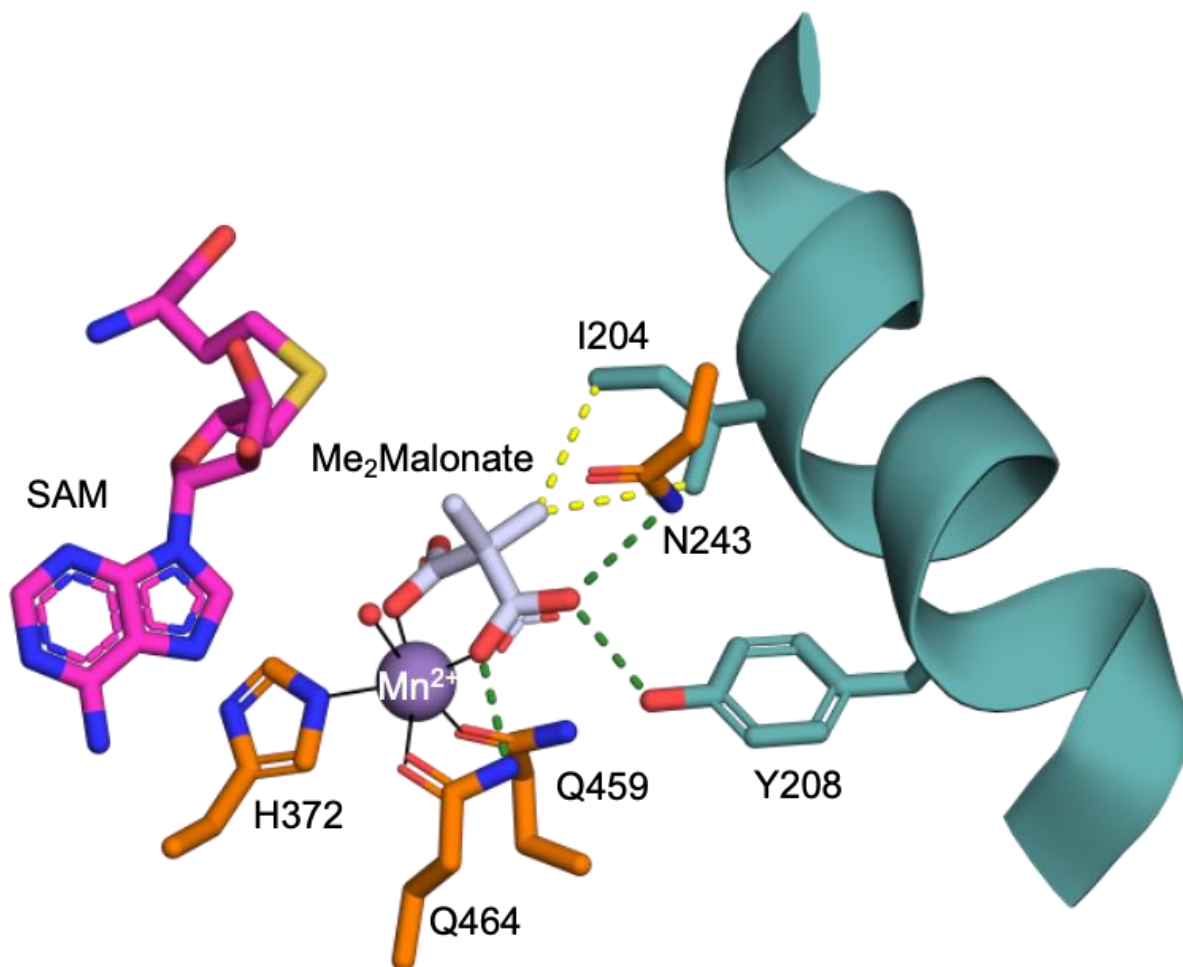


Figure 3.7. Active site of SxtA MT-DC F458H with dimethylmalonate and SAM.

SAM and the methyl groups of dimethylmalonate are modeled, based on the structures in **Figure 3.2d, e**. The pro(*R*) methyl of dimethylmalonate clashes with the Ile204 side chain. Metal ligands (His372, Gln459, and Gln464), Asn243, Ile204, and Tyr208 are colored according to the domain of origin (**Figure 2.2c**), dimethylmalonate with white C and SAM with magenta C, metal coordination bonds as solid black lines, hydrogen bonds as dashed green lines and the steric clash as dotted yellow lines

3.3.7 Selectivity filter for the extent of methylation

We investigated the role of Ile204 in methyl transfer by replacing Ile204 with Thr or other small amino acids (Ala and Val) in an SxtA MT-DC background with a candidate base for a second methyl transfer (F458Y), a ligand sphere like AprA MT1 (Q459H), and no

decarboxylase activity (T637V) (**Figure 3.3a**). In this background, the Thr204 and Ala204 variants had significant levels of Mn^{2+} -dependent dimethylation activity (**Figure 3.9a**). In the standard assay, the dimethylated product predominated for the Thr substitution ($62\pm 2\%$ Me₂Mal-ACP, $30\pm 3\%$ MeMal-ACP), whereas the Ala substitution yielded more monomethylated product ($30\pm 3\%$ Me₂Mal-ACP, $58\pm 2\%$ MeMal-ACP (**Figure 3.9a**). Despite the similar size of the Val and Thr side chains, we detected no dimethylation with the I204V variant (**Figure 3.3a**). This is consistent with the crystal structures: unlike Thr, the hydrophobic Val side chain would be unable form a hydrogen bond with the protein backbone and unable to remove its methyl substituents from the substrate pocket (**Figure 3.8 a-c**).

We confirmed that an analogous selectivity filter for the extent of methylation exists in AprA by creating AprA MT1-ΨDC T202I. In contrast to the wild type enzyme, AprA MT-ΨDC T202I had no detectable dimethylation activity, but retained monomethylation activity ($60\pm 8\%$ MeMal-ACP), confirming the critical role of position 202 in controlling methylation extent (**Figure 3.9c-d**).

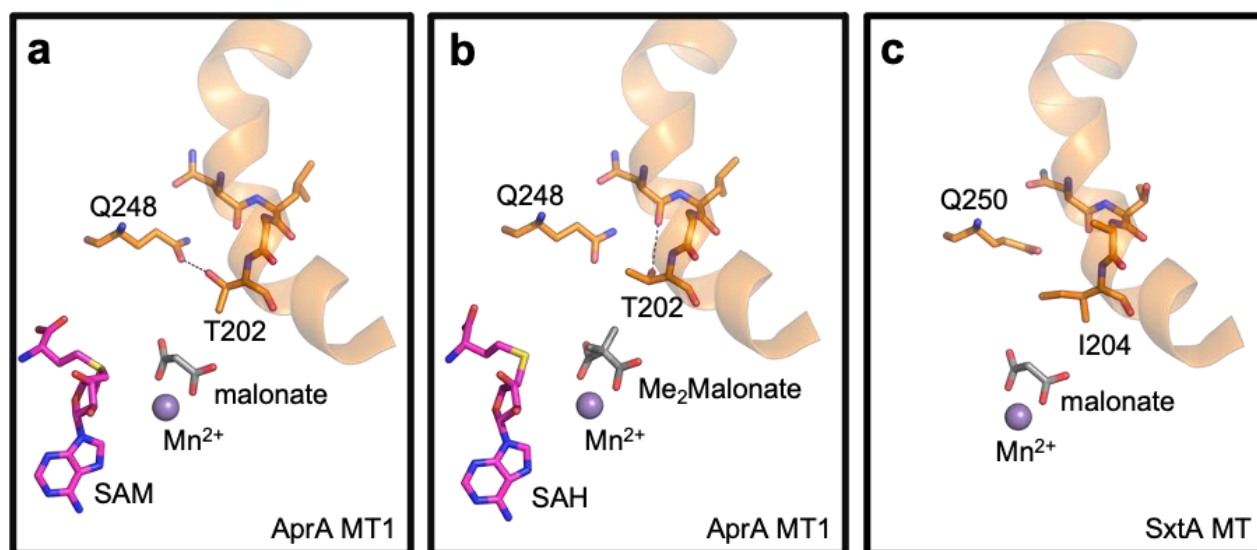


Figure 3.8. Comparison of selectivity filters for methylation extent in AprA MT1 and SxtA MT.

(a-b) Active site of AprA MT1 and of (c) SxtA MT with Mn²⁺ (purple sphere) and malonate or dimethylmalonate (gray C). Hydrogen bonds are shown in dashed black lines. Select amino acids (SxtA 201-204, 250; AprA 199-202, 248), malonate and dimethylmalonate are shown in sticks with atomic coloring (red O, blue N, yellow S, orange C). The kinked helix (SxtA 195-209; AprA 193-207) is rendered as a helix.

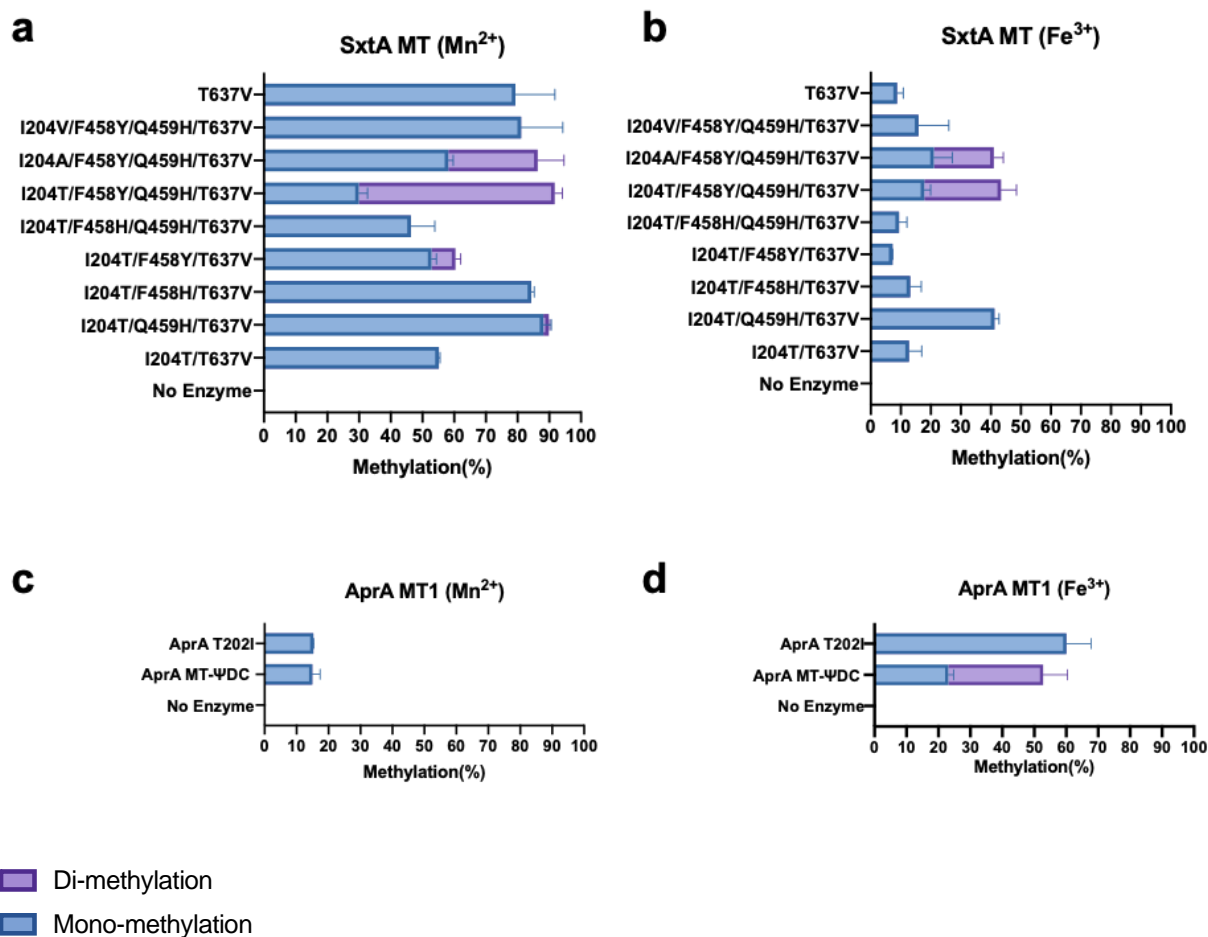


Figure 3.9. Impact of Ile204 on the extent of methylation.

(a-b) Mono- and dimethylation activity of SxtA MT-DC wild type and variants that include I204T in the presence of Mn^{2+} (a) and Fe^{3+} (b). (c-d) Mono- and dimethylation activity of AprA wild type and variants in the presence of Mn^{2+} (c) and Fe^{3+} (d). Monomethylation (sum of Ppant ejection fragments from MeMal-ACP and propionyl-ACP) and dimethylation (sum of Ppant ejection fragments from Me₂Mal-ACP and isobutyryl-ACP) were quantitated as a percent of total Mal-ACP. Error bars represent standard errors of more than three experiments.

3.3.8 SxtA MT metal preference

The His substitution for Gln at SxtA position 459 created a first-shell ligand field identical to that in AprA MT1. This substitution was essential for high levels of dimethylated product in the Mn^{2+} -dependent SxtA MT reaction, yielding eightfold greater dimethylation activity relative to the variant with Gln459 ($62 \pm 6\%$ Me₂Mal-ACP for I204T/F458Y/Q459H/T637V vs. $8 \pm 2\%$ for I204T/F458Y/Q459/T637V) (Figure 4.9a).

However, the Q459H substitution did not switch the metal preference of SxtA from Mn^{2+} to match the Fe^{3+} preference of AprA MT1. The SxtA I204T and I204A variants in the F458Y/Q459H/T637V background formed mono- and dimethylated products in an Fe^{3+} -dependent reaction, but levels of both products were more than twofold lower with Fe^{3+} than with Mn^{2+} (**Figure 4.9b**). The Q459H substitution led to no detectable dimethylation activity with either metal unless combined with I204T. In contrast, AprA MT1 supported the second methyl transfer reaction with Fe^{3+} , but not with divalent metal ions (Mn^{2+} or Fe^{2+})⁴⁴ We attempted a reciprocal experiment by substituting Gln for His at the analogous position in AprA MT-ΨDC (H456Q); however, the protein was unstable and could not be purified. No obvious structural feature of SxtA MT or AprA MT1 explains their differential metal preferences, which we conclude are due to subtle effects outside the immediate metal environment.

3.3.9 Conclusion

Our study revealed how two metal-dependent C-MTs control the extent of methylation. The discovery of a selectivity filter for one vs. two methyl transfers is directly applicable to related C-MTs in several other biosynthetic pathways. Crystal structures of SxtA MT-DC wild type and F458H together with biochemical assays of an extensive mutagenesis panel provided insights into MT function. A single substitution in the C-MT metal ligand field (Q459H) enhanced catalytic activity. A His substitution for Phe at position 458 accelerated methyl transfer by stabilizing the ligand sphere of the catalytic metal and may be useful for engineering efficient monomethylation catalysts. However, dimethylation required both a base at position 458 (Tyr) and a dimethylmalonyl-permissive filter at position 204 (Thr). The new understanding of how the C-MTs control methylation extent will aid future methyltransferase engineering for use in drug optimization and inform the engineering of valuable methyltransferase catalysts.

3.4 Materials and Methods

3.4.1 Plasmid preparation

Previously reported plasmids were used: pMSG7-*SxtA*_1_721⁶⁶ (encoding the SxtA MT-DC, residues 1–721 in SxtA; GenBank WP_009343302.1) and pMAS284 *AprA*_ACP (encoding the AprA ACP, residues 1058–1138; GenBank WP_075900460)⁴⁴. For a truncated SxtA MT-DC (residues 1–710), pMSG7-*SxtA*_1_710 was sub-cloned using primers in **Table 3.1**. Site-directed mutagenesis was done via QuikChange (Agilent) using primers in **Table 3.1**.

Table 3.1. Primers used for ligation-independent cloning (LIC) and site-directed mutagenesis.

| Name | Vector | Primer |
|--------------------|--------|--|
| SxtA 1_710 Forward | pMSG7 | TACTTCCAATCCAATGCAATGTTACAAAAGATTAATCG |
| SxtA 1_710 Reverse | | TTATCCACTTCCAATGCTACGAGTGCAAAGCACTGTCGCGCA |
| SxtA_T637V_Foward | pMSG7 | CATAATTTTCGACAGCGAACTACACCCACCACGCTCTCAAT |
| SxtA_T637V_Reverse | | ATTGAGAGCGTGGTGGGTGTAGTTTCGCTGTCGAAATATATG |
| SxtA_F458Y_Forward | pMSG7 | GAGAAAATCCCTGATACGCATCGAAATGTAAGTTTTTCGC |
| SxtA_F458Y_Reverse | | GCGAAAACCTTACATTTTCGATGCGTATCAGGGATTTCTC |
| SxtA_Q459H_Forward | pMSG7 | ACTGCTGAGAAAATCCATGAAACGCATCGAAATGTAAGTTTTTCG |
| SxtA_Q459H_Reverse | | CGAAAACCTTACATTTTCGATGCGTTTCATGGATTTTCTCAGCAGT |
| SxtA_I204T_Forward | pMSG7 | GGAGTGTAGGACGCCACCGTGGCTGTATTCAAGGCT |
| SxtA_I204T_Reverse | | AGCCTTGAATACAGCCACGGTGGCGTCCTACACTCC |
| SxtA_F458H_Forward | pMSG7 | CGAAAACCTTACATTTTCGATGCGCATCAGGGATTTTCTCAGCAGTAT |
| SxtA_F458H_Reverse | | ATACTGCTGAGAAAATCCCTGATGCGCATCGAAATGTAAGTTTTTCG |
| AprA_T202I_Forward | pMSG7 | GCATAAGACGCTGTTATTCCTAAGTTTAAGGATCTGTAC |
| AprA_T202I_Reverse | | GTGACAGATCCTTAAACTTAGGAATAACAGCGTCTTATGC |
| SxtA I204A_Foward | pMSG7 | GAGTGTAGGACGCCACTGCGGCTGTATTCAAGGCTC |
| SxtA I204A_Reverse | | GAGCCTTGAATACAGCCGCAAGTGGCGTCCTACACTC |
| SxtA I204V_Forward | pMSG7 | GTGTAGGACGCCACTACGGCTGTATTCAAGGCT |
| SxtA I204V_Reverse | | AGCCTTGAATACAGCCGTAGTGGCGTCCTACAC |

3.4.2 Bacterial expression

All plasmids were transformed into *Escherichia coli* strain BL21(DE3). Cell cultures were grown at 37 °C in 0.5 L Terrific Broth (TB) with 100 µg mL⁻¹ ampicillin until OD₆₀₀ reached 1–2, then cooled to 20°C over 0.5–1 hr, induced with 200 µM IPTG, and grown overnight. In cultures producing apo-ACP, 0.5 mL of filter-sterilized 1000X trace metal ions mix¹¹¹ was added to the 0.5 L culture to repress *E. coli entD*, which encodes a phosphopantetheinyl transferase that can act on many heterologous ACPs.

3.4.3 Purification of SxtA MT-DC and its variants, and AprA ACP

Cell pellets from 0.5 L cultures were resuspended in 35 mL Buffer A (50 mM Tris pH 7.4, 300 mM NaCl, 10% (v/v) glycerol) with 0.1 mg mL⁻¹ lysozyme, 0.05 mg mL⁻¹ DNase, 2 mM MgCl₂, 20 mM imidazole. Resuspended cells were incubated on ice for 30 min, lysed by sonication and centrifuged at 38,650 x g, for 20 min. The soluble fraction was then filtered through a 0.45 µm MILLEX-HP membrane and loaded onto a 5 mL His trap column (cytiva) pre-equilibrated with Buffer A. The column was washed with 50 mL Buffer A and eluted with a 50 mL gradient of 20–400 mM imidazole in Buffer A. For SxtA MT-DC, the N-terminal His tag was removed by overnight dialysis at 4°C in the presence of tobacco etch virus (TEV) protease⁸³ and 2–5 mM dithiothreitol (DTT) at a 50:1 molar ratio of MT-DC:protease. The mixture was reapplied to the His-trap column to remove uncleaved MT-DC and the protease. SxtA MT-DC and AprA ACP proteins were further purified via HiLoad Superdex S200 or S75 (Cytiva) gel filtration chromatography with Buffer B (50 mM Tris pH 7.4, 50 mM NaCl, 10% (v/v) glycerol). The SxtA MT-DC eluted as a monomer with apparent molecular weight 80 kDa. The purified SxtA MT-DC was concentrated to 12-14 mg mL⁻¹ and stored in aliquots at –80°C.

3.4.4 Production of acyl-ACPs

AprA apo-ACP (180 μ M) was incubated with 20 μ M *Streptomyces verticillus* phosphopantetheinyl transferase (Svp)¹⁰⁵ or *Bacillus subtilis* phosphopantetheinyl transferase (Sfp)¹⁰⁴, 20 mM MgCl₂, and a 4-fold molar excess of Mal-CoA or MeMal-CoA for 4 hr at 30°C in Buffer B. Acyl-ACPs were purified via Superdex S75 gel filtration chromatography with Buffer B.

3.4.5 Protein crystallization and structural determination

His-tagged AprA MT- Ψ DC S274I/Q548P was purified as previously described⁴⁴ and crystallized at 20°C by vapor diffusion from a 2:2 μ L mixture of protein stock (11 mg mL⁻¹ in Buffer B with 1 mM SAH, 5 mM MnCl₂) and well solution (15% PEG 3350, 0.1 M dimethylmalonate). Microseeding was used to obtain single crystals. Harvested crystals were cryoprotected with well solution supplemented with 15% (v/v) glycerol. Crystals were isomorphous with those of Mn-bound MT- Ψ DC S274I/Q548P (PDB ID 6B3A⁴⁴). Electron density was complete except for the histidine tag and residues 149–159 in the MT lid. Crystal statistic is reported in **Table 4**. Structure validation was done with MolProbity¹¹², figures were prepared in PyMol, and sequence alignments were created using Clustal in Jalview^{113, 114}

Table 3.2. Collection and refinement statistics of AprA MT-DC crystallographic data.

| AprA MT-DC | |
|--|---|
| Ligands | Mn ²⁺ |
| | SAM |
| | dimethylmalonate |
| Data Collection | |
| Space group | <i>P</i> 2 ₁ 2 ₁ 2 ₁ |
| Unit cell, a,b,c (Å) | 60.6, 88.3, 136.0 |
| Unit cell, α,β,γ (°) | 90, 90, 90 |
| X-ray source | APS 23ID-B |
| Wavelength (Å) | 1.033 |
| d _{min} (Å) | 2.2 |
| R _{merge} | 0.291 (1.628) |
| Avg I/ σ (I) | 7.37 (1.18) |
| Completeness (%) | 99.9 (99.4) |
| Multiplicity | 10.6 (12.4) |
| Total observations | 411,229 (47,522) |
| Wilson B factor (Å ²) | 33.0 |
| CC _{1/2} | 0.995 (0.495) |
| CC* | 0.999 (0.814) |
| Refinement | |
| Data range (Å) | 45.2-2.2 |
| Reflections (#) | 38,737 |
| R _{work} /R _{free} (%) | 19.3/24.1 |
| Nonhydrogen atoms (#) | 5,538 |
| protein | 5,203 |
| ligands | 16 |
| water | 319 |
| Amino acid residues | 637 |
| Deviation from ideality | |
| bond lengths (Å) | 0.009 |
| bond angles (°) | 0.95 |
| Average B-factor (Å ²) | 40.8 |
| protein | 40.9 |
| ligands | 41.5 |
| solvent | 39.2 |
| Ramachandran plot | |
| favored (%) | 96.9 |
| allowed (%) | 3.1 |
| outliers (%) | 0.0 |
| PDB code | 7UCH |

¹Values in parentheses pertain to the outermost shell of data.

3.4.6 Methylation assay

For quantitative comparison of the activities of wild type SxtA MT-DC and its mutagenized variants, a standard assay was designed in which the wild type enzyme consumed

most, but not all, of the Mal-ACP substrate, and all assays were conducted identically under these conditions. Reaction mixtures contained 10 μM SxtA MT-DC, 100 μM Mal-ACP, 1 mM SAM and 0.5 mM metal (either $(\text{NH}_4)_2\text{Fe}(\text{SO}_4)_2$ or MnCl_2) in 50 mM HEPES pH 7.8, 150 mM NaCl. The reaction was initiated by the addition of SxtA MT-DC. The mixtures were incubated at 30°C for 4 h and quenched with 10% (v/v) formic acid.

3.4.7 Decarboxylation

Reaction mixtures and assay conditions were identical to those for the methylation assay above, excepting the omission of metal to prevent any methylation activity.

3.4.8 Methylation time course assay

Reaction mixtures contained 2.5 μM SxtA MT-DC T637V or F458H/T637V (residues 1–721), 100 μM Mal-ACP, 1 mM SAM and 0.5 mM MnCl_2 in 50 mM HEPES pH 7.8, 150 mM NaCl. Reactions were initiated by addition of SxtA MT-DC, and the mixtures were incubated at 30°C. Aliquots were removed at several time points (5 min, 15 min, 30 min, 1 h, 2 h, 3 h and 4 h) and quenched with 10% (v/v) formic acid.

3.4.9 Methylation kinetic assay

Reaction mixtures contained 1.45 μM SxtA MT-DC T637V or F458H/T637V (residues 1–721), varying concentrations of Mal-ACP (38, 60, 120, 150, 187, 250, 300, 400, or 600 μM), 0.75 μM SAM and 0.38 mM MnCl_2 in 50 mM HEPES pH 7.8, 150 mM NaCl. Reactions were initiated by addition of enzyme, mixtures were incubated at 30 °C, and aliquots (10 μL) were collected at time points (5, 15 and 30 min) and quenched with 10% (v/v) formic acid. Initial velocities were obtained from the slope of product vs. reaction time (5, 15 and 30 min). The

initial velocity/enzyme concentration vs. concentration curves were fit to the classic and refined Michaelis-Menten equations¹¹⁵ using PRISM 9 (GraphPad).

$$\text{Classic: } V_0 = \frac{k_{\text{cat}}[S]}{K_M + [S]}$$

$$\text{Refined: } V_0 = \frac{k_{sp}[S]}{1 + k_{sp}[S]/k_{\text{cat}}}, \quad k_{sp} = \frac{k_{\text{cat}}}{K_M}$$

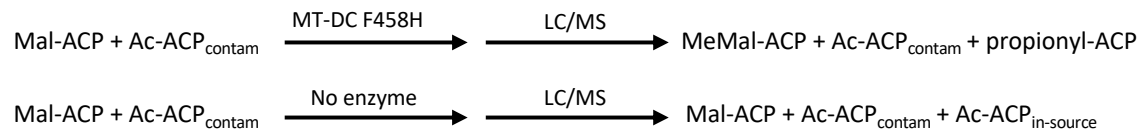
As expected, the k_{cat}/K_M values derived from either the classic or refined Michaelis-Menten equation are similar. For example, for MT-DC T637V, the values are $0.76 \pm 0.47 \text{ mM}^{-1} \text{ min}^{-1}$ (classic) and $0.78 \pm 0.45 \text{ mM}^{-1} \text{ min}^{-1}$ (refined).

3.4.10 Analysis of reaction products by liquid chromatography-mass spectrometry (LC-MS)

Reaction mixtures were analyzed using a simultaneous intact protein and phosphopantetheine (Ppant) ejection method^{116, 106} on an Agilent Q-TOF 6545 instrument (**Figure 3.10**). Insoluble material in the quenched reaction mixture was removed by centrifugation (13,000 rpm for 15 min), and the clarified reaction mixture (0.5 μL) was loaded onto a reverse-phase high-performance liquid chromatography (HPLC) column (Phenomenex Aeris widepore C4 column 3.6 μM , 50 x 2.10 mm) at flow rate of 0.5 mL/min in 0.2% (v/v) formic acid and separated with a gradient of 5–100% acetonitrile in 0.2% (v/v) formic acid over 8 min. MS operating conditions were 300 V fragment voltage, 75 V skimmer voltage, 100 V nozzle voltage, 350 °C sheath gas temperature, 325 °C drying gas temperature. The MassHunter Qualitative Analysis Software (Agilent) was used for analysis of mass spectra, based on extracted ion counts (EIC) for acetyl- (Ac-), Mal-, propionyl-, MeMal-, isobutyryl-, and Me₂Mal-ACPs and their Ppant ejection fragments. Quantitation of methylation in each reaction, where Mal-ACP was the substrate, was the summed EIC for methylated Ppant ejection species (propionyl-, MeMal-, isobutyryl- and Me₂Mal-Ppant) relative to summed EIC (Mal-, propionyl-,

MeMal-, isobutyryl- and Me₂Mal-Ppant). Similarly, the extent of mono-methylation was the total EIC for propionyl- and MeMal-Ppant relative to the overall total, and the extent of di-methylation was the total EIC for isobutyryl- and Me₂Mal-Ppant relative to the overall total. We detected Ac-ACP in all samples, even those with an inactivated DC (MT-DC T637V). The presence of Ac-ACP was due in part to a low level of ionization-induced decarboxylation of Mal-ACP in the mass spectrometer and in part to low levels of contaminating Ac-ACP in Mal-ACP preparations. The level of contaminating Ac-ACP varied with Mal-ACP preparation and time, but the in-source decarboxylation was constant given the uniform MS protocol used for all assays. We quantitated the level of in-source decarboxylation to correct the observed Mal-Ppant EIC values. For this, we used an MT-DC variant (F458H) that methylated all Mal-ACP during the 4 h reaction time, leaving no Mal-ACP for in-source decarboxylation. (We also determined that no spontaneous decarboxylation of Mal-ACP was detectable during the 4 h reaction period.) Parallel incubations were conducted with MT-DC F458H and with a no-enzyme control and As expected, Ac-ACP levels were higher in the no-enzyme control due to in-source decarboxylation of Mal-ACP, whereas the Ac-ACP in the sample incubated with MT-DC F458H was due to contamination only. The excess Ac-ACP in the no-enzyme control was $6.2 \pm 1.4\%$ (n=7), and all Mal-ACP values were corrected for this effect (EIC x 1.062). Similarly, low levels of in-source decarboxylation of MeMal- and Me₂Mal-ACP were established by detection of propionyl-ACP in samples reacted with MT-DC T637V and isobutyryl-ACP in samples of MT-DC I204T/F458Y/Q459H/T637V where enzymatic decarboxylation was absent. In-source decay values were $10.7 \pm 1.1\%$ (n=3) for MeMal-ACP and $6.0 \pm 0.7\%$ (n=6) for Me₂Mal-ACP. The quantification of decarboxylation, EIC of propionyl- or isobutyryl-ACP over the sum of MeMal- and propionyl, and of isobutyryl-ACP and Me₂Mal-ACP, was corrected according to the in-

source decay values.



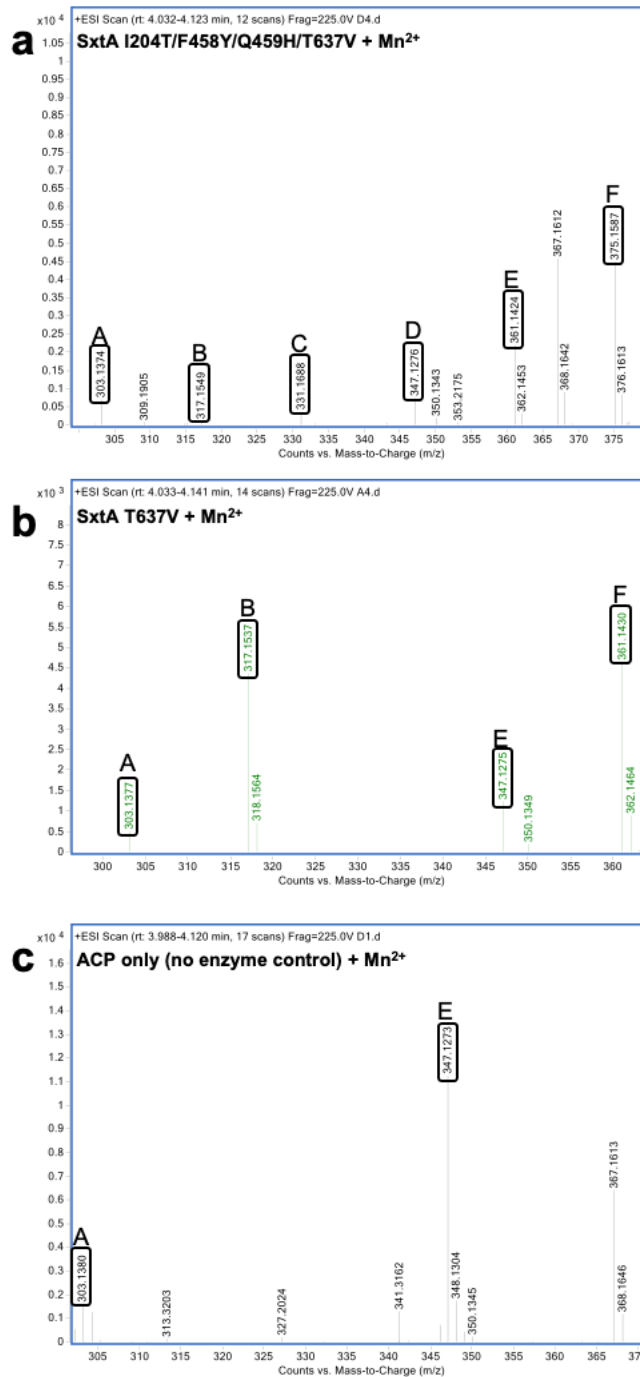
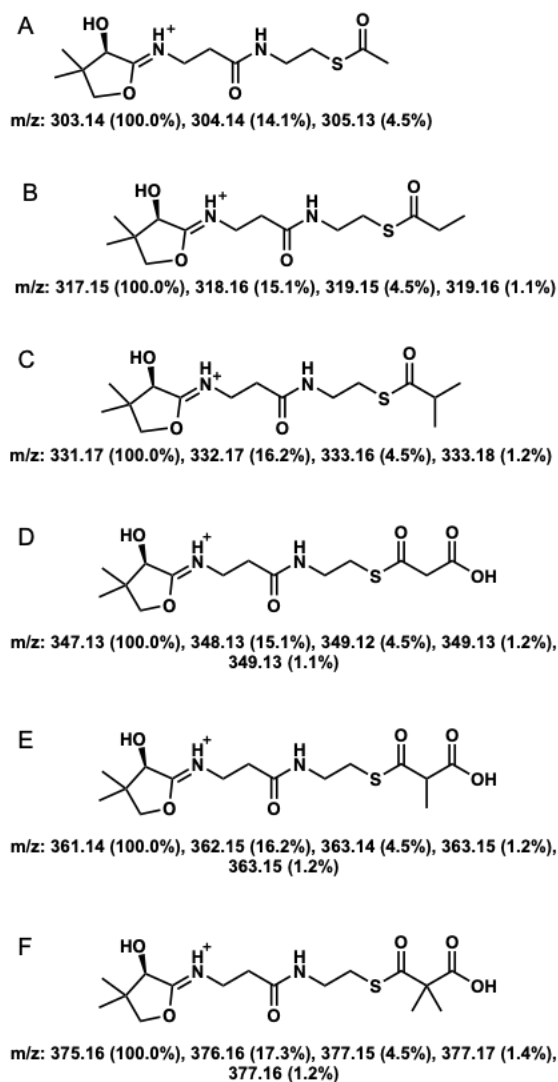


Figure 3.10. Representative electrospray-ionization (ESI) mass spectra of AprA ACP ejection fragments in reaction samples.

Chapter 4 The Functional and Structural Analysis of Saxitoxin DC and AONS

4.1 Summary

Saxitoxin (SXT) is notorious for causing paralytic poisoning associated with contaminated seafood consumption. Its tricyclic, bisguanidinium ion-containing scaffold grants a nanomolar affinity toward voltage-gated sodium channels^{91, 92}. Its exceptional toxicity also hinders the potential use of SXT to study neurodegenerative diseases and to treat acute pain. However, an SXT derivative, gonyautoxin 5 (GXT 5) (**Figure 4.1**), which differs from SXT by only one sulfate group, has reduced toxicity and is currently in a clinical trial as a pain therapeutic^{117, 118}. GXT5 demonstrates advantages over many available pain medicines because of its lower risk of causing cardiotoxicity and minimized abuse potential. The high pharmaceutical potential of SXT can be expanded through modification of the saxitoxin biosynthesis pathway to generate analogs with improved properties. Although synthetic routes for accessing SXT and GXT are available^{119, 120}, they require multiple steps and ultimately suffer from poor yield and specificity. Therefore, a chemoenzymatic method to produce saxitoxin derivatives would have high utility. Biosynthesis pathways of SXT and its derivatives share the mutual SxtA starter module; enzymatic modification of this SxtA module can lead to a different chemical outcome of the pathways. Previously, I described the success in engineering SxtA methyltransferase (MT) to catalyze an additional methyl transfer to dimethylate malonyl-acyl carrier protein (ACP). In this chapter, we will investigate the influence an engineered domain has on the chemoenzymatic outcome of the SxtA module.

In the SxtA module, SxtA decarboxylase (DC) perform catalysis after the MT reaction. SxtA DC has the (general control non-derepressible 5(GCN5)) related N-acetyltransferase

(GNAT) scaffold. Members of the GNAT family are best known to acetylate diverse amine substrates, such as aminoglycosides, antibiotics, histones, and other primary and secondary metabolites¹²¹⁻¹²⁴. They are also one of the most characterized proteins in the protein data bank (PDB), with hundreds of deposited structures. Instead of performing acyltransfer like most GNAT members, SxtA DC decarboxylates methylmalonyl (MeMal)-ACP to generate propionyl-ACP (**Figure 4.2**). Similar examples are GphF and CurA DCs^{58, 125, 51}. MT engineering to diversify the chemoenzymatic outcome of the SXT pathway may be restrained by the DC and other downstream enzymes. The DC domain may work as a gatekeeper because they could reject substrates and intermediates of the upstream MT to ensure the pathways produce only the natural compound. For example, SxtA DC acts on MeMal-ACP but not Mal-ACP; GphF acts on dimethylmalonyl (Me₂Mal)-ACP but not on MeMal- and Mal-ACPs^{125, 51}.

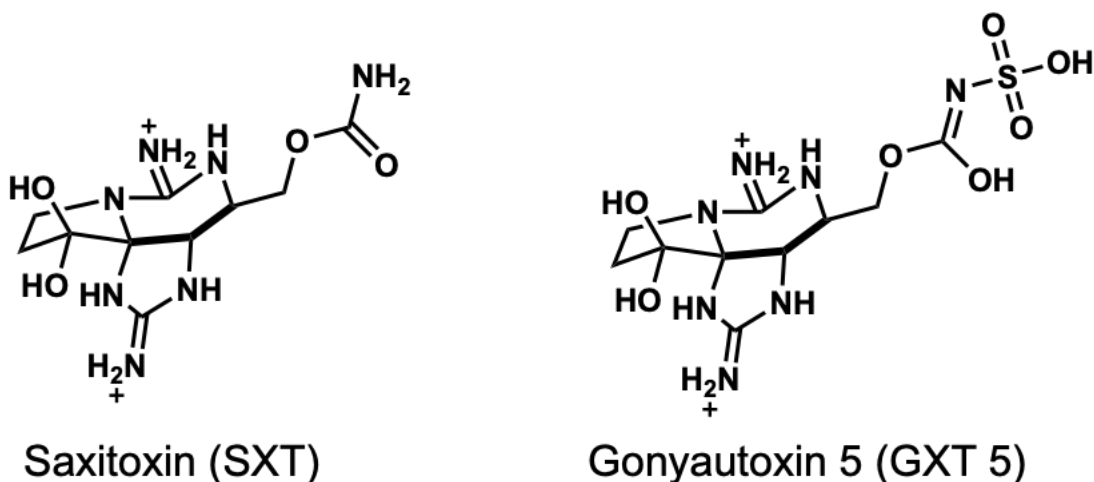


Figure 4.1. Chemical structures of saxitoxin and its derivative, gonyautoxin 5.

After the SxtA decarboxylation reaction, an 8-amino-7-oxononanoate synthase (AONS) domain catalyzes stereospecific ‘carbon-carbon formation’ between the carboxyl group on propionyl-ACP and the α -carbon of arginine to produce SxtA precursor (**Figure 4.2**). AONS can process a few non-native substrates to bear cyclic, aromatic, and saturated arginine-derived

ketones⁸⁰. In a previous report¹²⁶, SxtA AONS also demonstrated great potential as a biocatalyst as it can be repurposed to install a deuterium atom on the α -carbon of various amino acids and amino ketone with high site- and stereoselectivity. Deuteration can be a late functional functionalization strategy to modify the pharmaceutical properties of a drug candidate¹²⁷. AVP-786 is a deuterated version of dextromethorphan/quinidine that treat the pseudobulbar affect and this compound has demonstrated improved clinical efficacy (such as reduced metabolism rate and cardiac adverse effect)¹²⁸. In addition, investigation of substrate selectivity and structures of SxtA AONS provides insights about the utility of this enzyme as a chemoenzymatic

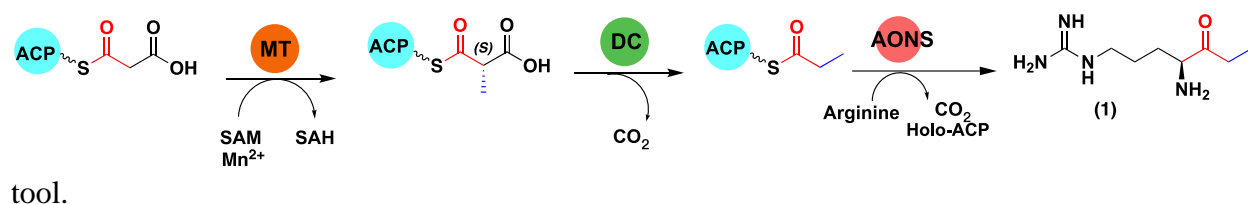


Figure 4.2 Reaction scheme of SxtA MT, DC and AONS in the SxtA module.

A more in-depth investigation of substrate selectivity of SxtA DC and AONS is essential to elucidate the chemoenzymatic effect of an engineered SxtA (from a mono- to dimethyltransferase) on the chemical outcome of the SxtA module. Herein, I report the SxtA DC activity on Me₂Mal-ACP to make isobutyryl-ACP and SxtA AONS activity on isobutyryl-ACP (**Figure 4.3 and 4.8**). We also performed structural analysis to further understand the substrate selectivity and biochemical mechanisms of SxtA DC and AONS via active site substrate modeling.

4.2 Introduction

4.2.1 The magic methyl effect

SxtA DC activity on MeMal- versus Me₂Mal-ACP was investigated with SxtA I204T/F458Y/Q459H, a variant that possesses engineered dimethylation activity and wild type decarboxylation activity. Unexpectedly, SxtA DC demonstrates a similar decarboxylation activity on both MeMal- and Me₂Mal-ACP (81% and 77%, respectively (**Figure 4.3**)). A T637V substitution inactivates the DC domain. The presence of an active decarboxylase after an engineered dimethylating SxtA reduces the yield of dimethylated products by about twofold (27.7% dimethylation for I204T/F458Y/Q459H vs. 62.2% for I204T/F458Y/Q459H/T637V, (**Figure 5.3**)). The SxtA DC domain decarboxylates monomethylated products more rapidly than the MT can facilitate a second methyl transfer. This follows our prediction in Chapter 3. In addition, this phenomenon may be influenced by conformational effects that would differ for an ACP substrate *in cis*, as in full-length SxtA, rather than *in-trans*, as in our assay. This situation does not pertain to AprA MT1 because the AprA ΨDC lacks catalytic activity, and decarboxylation is coupled to a third methyl transfer performed by the AprA MT2 domain, which is selective for Me₂Mal-ACP^{43, 44}

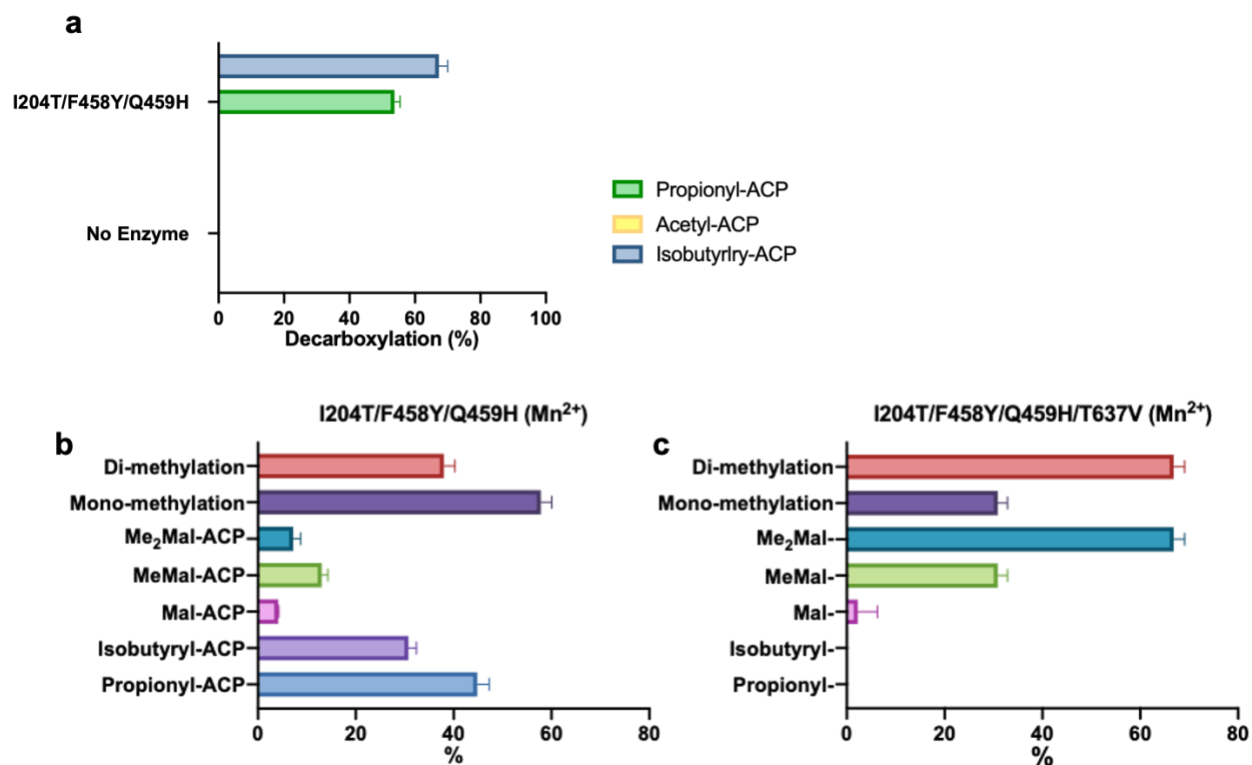


Figure 4.3. Methylation and decarboxylation activity by SxtA MT-DC.

The decarboxylation activity of Mal-, MeMal-, and Me₂Mal-ACP by the dimethylating SxtA MT-DC variant I204T/F458Y/Q459H was evaluated. (a) decarboxylation is quantified as the percent of acetyl-, propionyl- and isobutyryl- species. Error bars represent the standard deviation of at least four replicates. (b-c) acyl-ACP substrates in reaction mixtures (SxtA MT-DC I204T/F458Y/Q459H and I204T/F458Y/Q459H/T637V with an inactive DC) were quantified as above.

The gatekeeping role of PKS DCs was supported by their high substrate selectivity to ensure the production of the correct starter unit because the incorrect products could be passed to later steps. DC displayed a 100-fold higher selectivity for its natural substrate Me₂Mal-ACP over MeMal-ACP or Mal-ACP (**Figure 4.4**)⁵¹. Likewise, SxtA DC demonstrated high selectivity of MeMal-ACP over Mal-ACP. However, PKS DCs may decarboxylate acyl-ACP species that are uncommon in their biosynthesis environment because they may not have evolved a mechanism to reject them yet. For example, CurA DC, after a truncated and inactive MT, performed a similar level of decarboxylation on Mal-ACP and MeMal-ACP (90%) in a two-hour reaction⁵¹.

In addition, SxtA DC still performs catalysis on the non-native Me₂Mal-ACP substrate.

Gatekeeping in PKS has set a challenge of engineering biosynthesis pathway to generate novel compounds with high chemodiversity; therefore, we will investigate the basis of substrate selectivity among the three DCs.

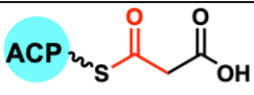
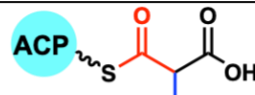
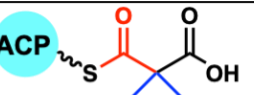
| |  |  |  |
|---------|---|---|---|
| SxA DC | No conversion in 4 h | 81% conversion in 4 h | 77% conversion in 4 h |
| GphF DC | No conversion in 48h | 50% conversion in 24h | 85% conversion in 2 h |
| CurA DC | 90% conversion in 2 h | 90% conversion in 2 h | 45% conversion in 24h |

Figure 4.4 Summary of decarboxylation activity of Mal-, MeMal- and Me₂Mal-ACP by SxtA, GphF, and CurA DCs

Previous crystallographic complexes of GphF DC/ isobutyryl-CoA (PDB:6MFD), and CurA DC/ acetyl-CoA (PDB:2REF), combined with site-directed mutagenesis and LC/MS-based assays were insufficient to reveal the basis of decarboxylation selectivity⁵¹. Therefore, we incorporated substrates (Me₂Mal- and Mal-substrates for GphF and CurA, respectively) into the inactive GphF (S626A)⁵¹ and CurA (T355A)⁵⁸ DC. These DCs require a conserved His and a Thr/Ser activity. The histidine is thought to coordinate the two oxygen atoms of the acyl-substrate, and the threonine/serine stabilizes the reaction intermediate and acts as a proton donor (**Figure 4.5**)⁵⁸. According to the mechanism, serine and threonine substitutions would abolish

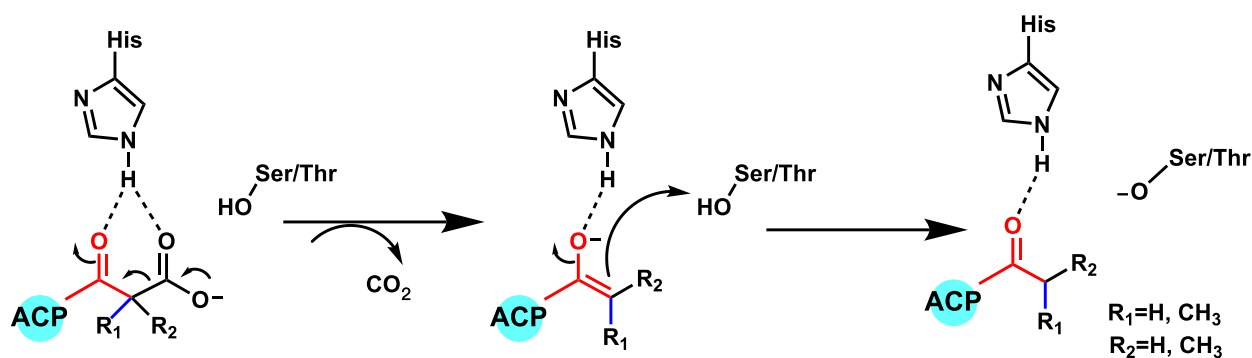


Figure 4.5. Proposed decarboxylation mechanisms for SxtA, CurA and GphF DCs.

SxtA and CurA DC apply a catalytic threonine to donate a proton to the decarboxylated intermediate; GphF DC uses a serine for the same function.

decarboxylation activity while retaining the substrate binding interaction. Structures with intact substrates bound may provide local binding information about the methyl groups of malonyl-substrates that lead to the different catalytic activities of PKS DCs. We determined structures of GphF S626A with dimethylmalonate and CurA T355A with malonyl-CoA by using X-ray crystallography (**Table 5**). The precise position of the terminal carboxylate group on their malonyl-substrates was not modeled because of the poor electron density of the region.

4.2.2 Proposed features of controlling substrate selectivity in DCs

Certain degree of steric hindrance and hydrophobicity within the active site may lead to different decarboxylation levels of Mal, MeMal, and Me₂Mal-substrates. DCs with residues within the active site that are sterically blocking the methyl groups on the α -carbon of malonyl may prefer Mal- over MeMal and Me₂Mal- substrates. Conversely, DCs with more hydrophobic residues around the malonyl binding site may choose methylated malonyl over malonyl substrates. To test this hypothesis, we modeled Me₂Mal-CoA into the active sites of GphF, CurA, and SxtA MT (**Figure 4.6a-c**). The active site in the three DCs is formed by a hydrophobic patch, and no detectable difference in hydrophobicity within is found. However, the

clefts that include the malonyl group are of different sizes for each DCs (**Figure 4.6d-f**). The malonyl binding site is the biggest for GphF DC, followed by SxtA MT, then CurA MT, possibly explaining why GphF DC prefers the bulkier Me₂Mal-substrate while CurA DC prefers the smaller malonyl-substrate. GphF DC has amino acids with smaller side chains compared to CurA and SxtA within the malonyl binding pocket; It contains His690 (corresponded to CurA Tyr419/SxtA Tyr701), Gly624 (CurA Ala353/SxtA Gly635), Thr555 (CurA I284/SxtA I566) and Val688 (CurA Val688/ SxtA Ile699). These amino acids can be examined to identify the basis for the differing substrate selectivity. Contrary to the hydrophobicity hypothesis, it appears that steric hindrance and size of the pocket are more important for substrate selectivity. These features are influenced by amino acid side-chain composition and their respective orientation.

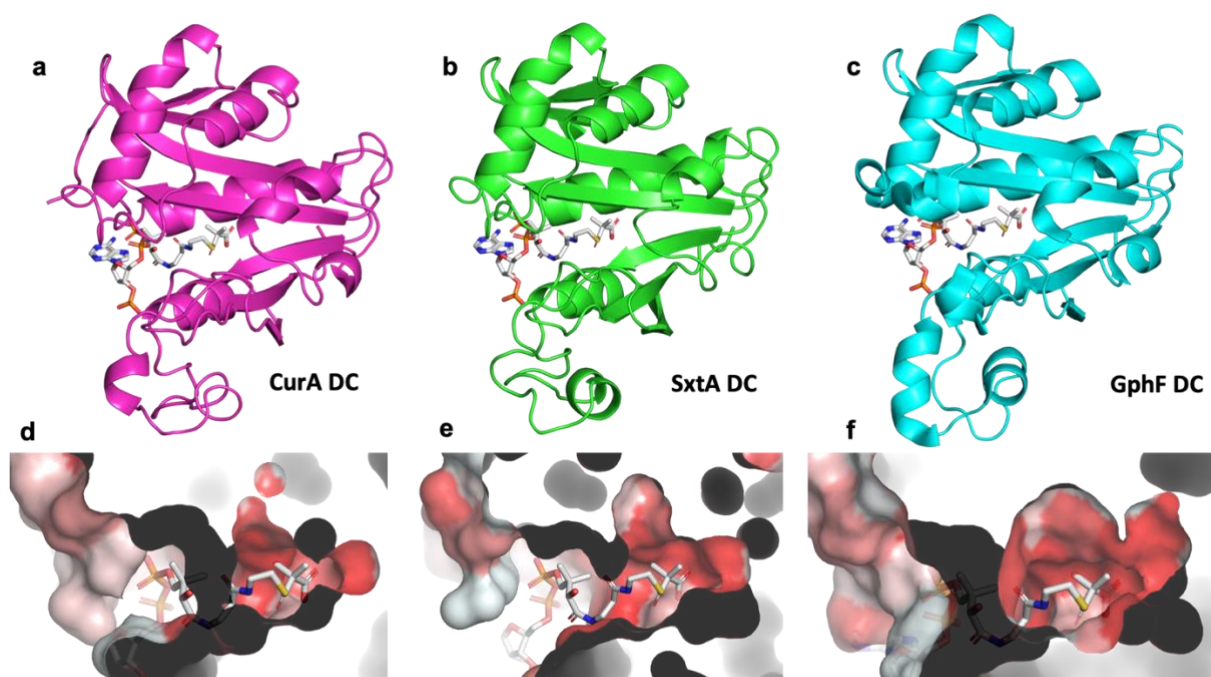


Figure 4.6. Comparing active sites of CurA, SxtA, and GphF DCs

Cartoon structure of CurA (**a**), SxtA (**b**), and GphF (**c**) DCs with modeled dimethylmalonyl-CoA (shown in sticks with atomic coloring (red O, blue N, yellow S, white C)). Active sites of CurA (**d**), SxtA (**e**), and GphF (**f**) are shown as sliced surface views to reveal pocket size. Hydrophobicity (red, nonpolar; white, polar).

4.2.3 AONS activity on Isobutyryl-ACP

In contrast to the DC domain, a few studies have reported that AONS have broad substrate promiscuity, operating on a variety of CoA and amino acid substrates^{129, 80, 126}. Furthermore, AONS yielded nearly twofold corresponding amino ketone product with n-butyl-CoA than with the native substrate, propionyl-CoA, and mediated the formation of ketones bearing a cyclic and an aromatic substituent^{129, 80}. VsAOS1 from marine *Vibrio* sp, an AONS homolog that condenses L-glycine with an acyl-CoA, demonstrates that the substrate selectivity of AONS can be easily shifted¹³⁰. A single amino acid substitution in VsAOS1 allows it to generate a sphingoid derivative from L-serine and lauroyl-CoA. Upon testing, SxtA AONS catalyzes the formation of (2) from isobutyryl-ACP (Figure 4.7), a methylated (1). The quantification of the small molecule products of AONS ((1) and (2)) requires a standard curve generated using a variety concentration of synthetic standard of (1) and (2). The absolute quantification of AONS small molecule products requires a synthetic standard that we currently lack.

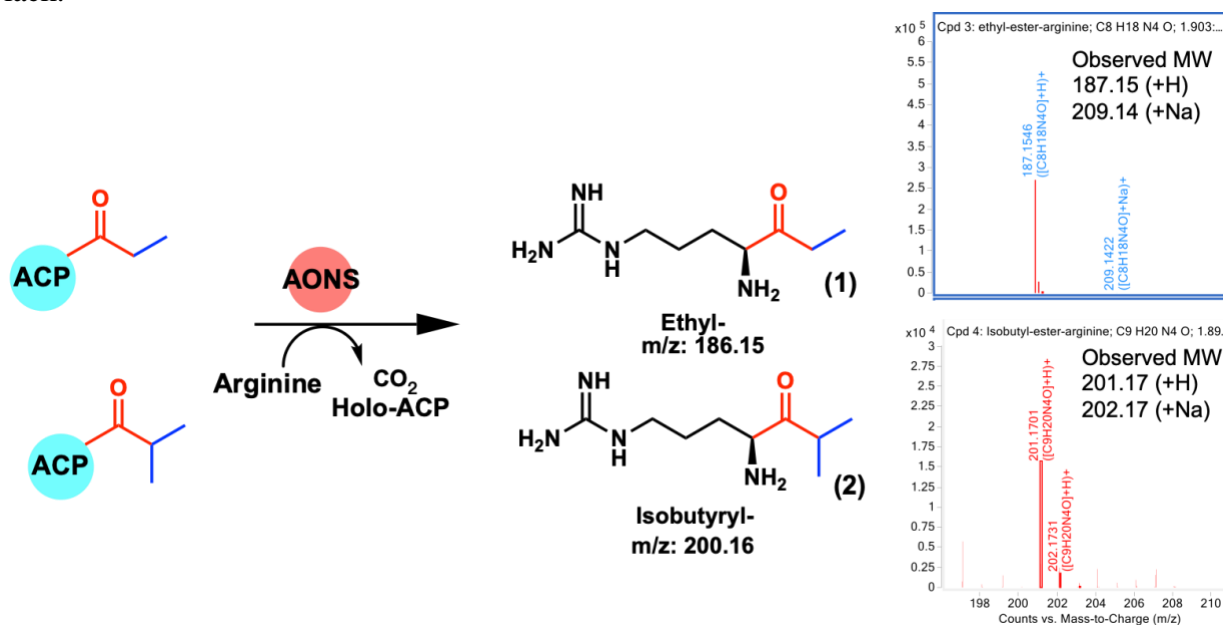


Figure 4.7. Representative electrospray-ionization (ESI) mass spectra of AONS product.

Chemical structures and calculated m/z values for ethyl- and isobutyryl ketone products are at the left and indicated on the mass spectra to the right.

4.2.4 AONS structure

A SxtA AONS structure will provide us insight into its broad substrate scope and features we can potentially alter to engineer SxtA AONS to accept different types of substrates it initially cannot. The structural determination of the AONS domain has been challenging. The AONS domain tends to be poorly soluble, resulting in very low yields upon purification. After comparing expression constructs of SxtA from both *Microseira wollei* and *Cylindrospermopsis raciborski*, the *M. wollei* construct displayed improved solubility, so it was chosen for crystallographic trials and biochemical studies. AONS members adopt a pyridoxal phosphate (PLP)-dependent mechanism (**Figure 4.8**)^{131, 1}. The aldehyde group of PLP forms an internal aldimine with the amino group of lysine. The pyridine ring of PLP is a strong electrophile that induces electron transfer from the respective amino site, displacing a substituent at the α carbon atom, and is essential for stabilizing a charged intermediate. The first step of the proposed reaction is to displace the lysine with the substrate, arginine. Then, the electrophilic pyridine ring induces electron transfer to the α carbon of arginine, facilitating deprotonation of this site by a basic amino acid. An external aldimine results. Then the nucleophilic aldimine attacks the carbonyl group of the acyl-ACP substrate to form a tetrahedral intermediate. The holo-ACP is released as a by-product, followed by decarboxylation of the tetrahedral intermediate. Finally,

the active site lysine displaces the arginine ester product to close the catalytic cycle by restoring the internal aldimine.

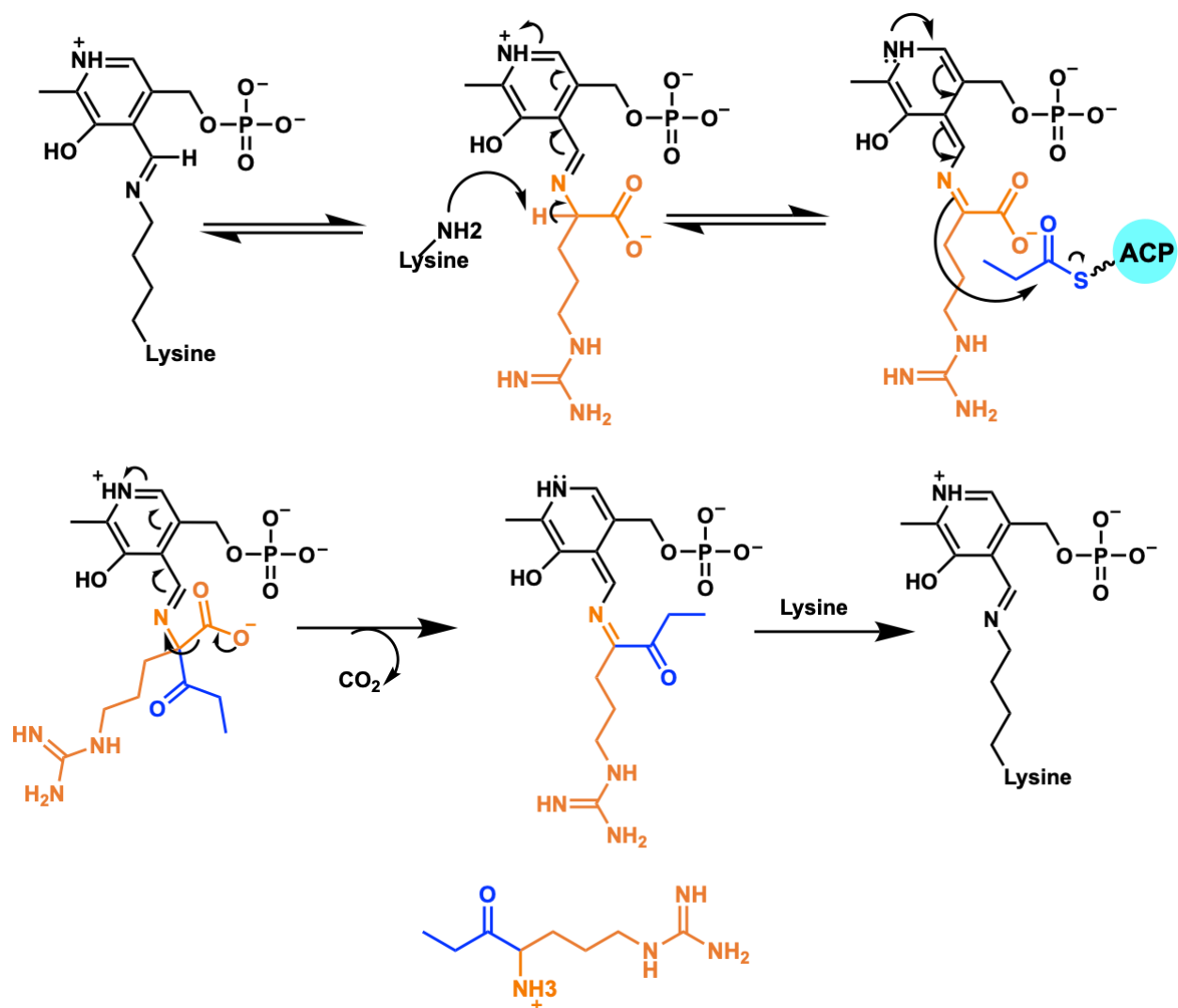


Figure 4.8. Proposed AONS mechanism.

4.2.5 AONS may mediate dimerization of the SxtA module

SxtA AONS is a homodimer in solution (demonstrated by size exclusion chromatography; data not shown) like most SxtA AONS homologs such as VsAOS1¹³⁰ and BioF AONS from the biotin synthesis pathway^{131, 1}. Therefore, I used AlphaFold to predict the structure of a SxtA AOND homodimer (**Figure 4.9**). Two α -helices partially wrapped by a β -

sheet are packed against their symmetric partner to form the center of the dimer. The SxtA AONS prediction structurally resembles that of BioF AONS (**Figures 4.9 and 4.10**). two AONS reaction intermediate (**3**) are modeled into the two active sites of this dimeric structure by using BioF AONS structure in complex with its PLP reaction intermediate (**Figure 4.9**) as a reference. Position of the modeled intermediate is further adjusted according to nearby interaction using Pymol editing. The BioF AONS ligand-interacting residues are mostly conserved among the AONS family. For the few amino acids that are not conserved (such as BioF AONS Gly108 and Phe109), only their backbone atom is involved in the ligand interaction (**Figures 4.10b,c and 4.11**). Some of these interactions cannot form in the predicted SxtA AONS structure, possibly because the prediction did not account for the potential conformational changes associated with substrate binding. In BioF AONS structures, substrate binding promotes an overall 1.4-Å conformational shift¹. Mg²⁺ ion coordination is also found in the substrate bound BioF AONS structure. However, metal binding is likely a crystallographic artifact because the BioF reaction is not metal-dependent. In conclusion, the AlphaFold predicted structure could not accurately provide us details about substrate-protein interaction because it could not predict the conformation shift upon substrate binding. The investigation of substrate selectivity among different AONS domains requires comparison of their experimentally determined structures. We are in the process of setting crystallization tray to solve an AONS structure in complex with its reaction intermediate.

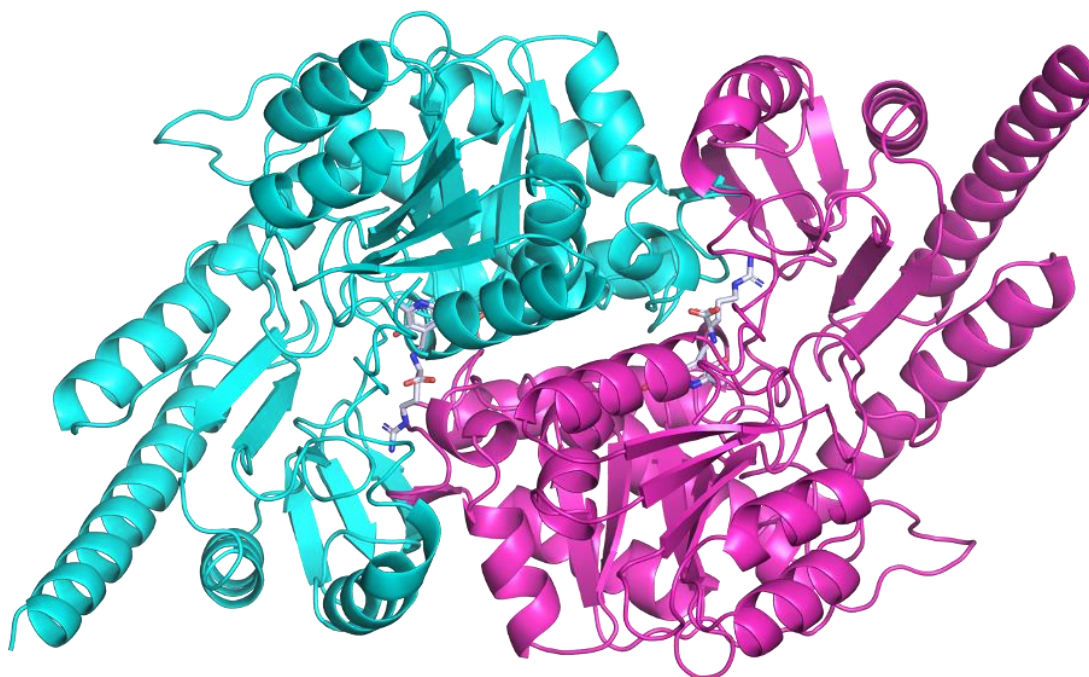


Figure 4.9. Structure of SxtA AONS in complex with its reaction intermediate (3).

(a) The SxtA AONS structure in a homodimer complex is predicted by AlphaFold. The reaction intermediate is modeled into the structure using PDB 1DJ9 as a reference¹. The protein structure is shown in the cartoon view, and two identical protein chains are colored in cyan and pink. Modeled (3) is shown in stick form red (O), blue (N), orange (P), and white (C).

Dimerization is essential for PKS function and is usually mediated by the KS, DH, and ER domains. The PKS-like SxtA module lacks these domains, so we propose that AONS promotes this dimer interface, evidenced by its behavior in solution. In addition, dimerization may be essential to the AONS function because, in the BioF AONS (PDB 1DJ9) structure, the reaction intermediate is coordinated by amino acid residues from both monomers of the dimer (**Figure 4.10**).

4.2.6 Conclusion

Me₂Mal-substrate modeling in CurA, GphF and SxtA DCs provide new insight into features distinguishing substrate selectivity of the three DCs. The size of their malonyl-binding

pocket determines if they would prefer the bulkier Me₂Mal over the malonyl-substrate. In each DC, Amino acids that account for malonyl-binding are identified. Site directed mutagenesis and biochemical assay will be conducted to further test this proposed idea.

The behavior of SxtA AONS in solution and its predicted structure in a homodimer have suggested that AONS functions as a dimer and may mediate dimerization of the whole SxtA module. Structural determination of the intact SxtA module will give us more information about the modular architecture and how substrate is passed onto the next domain according to the reaction sequence.

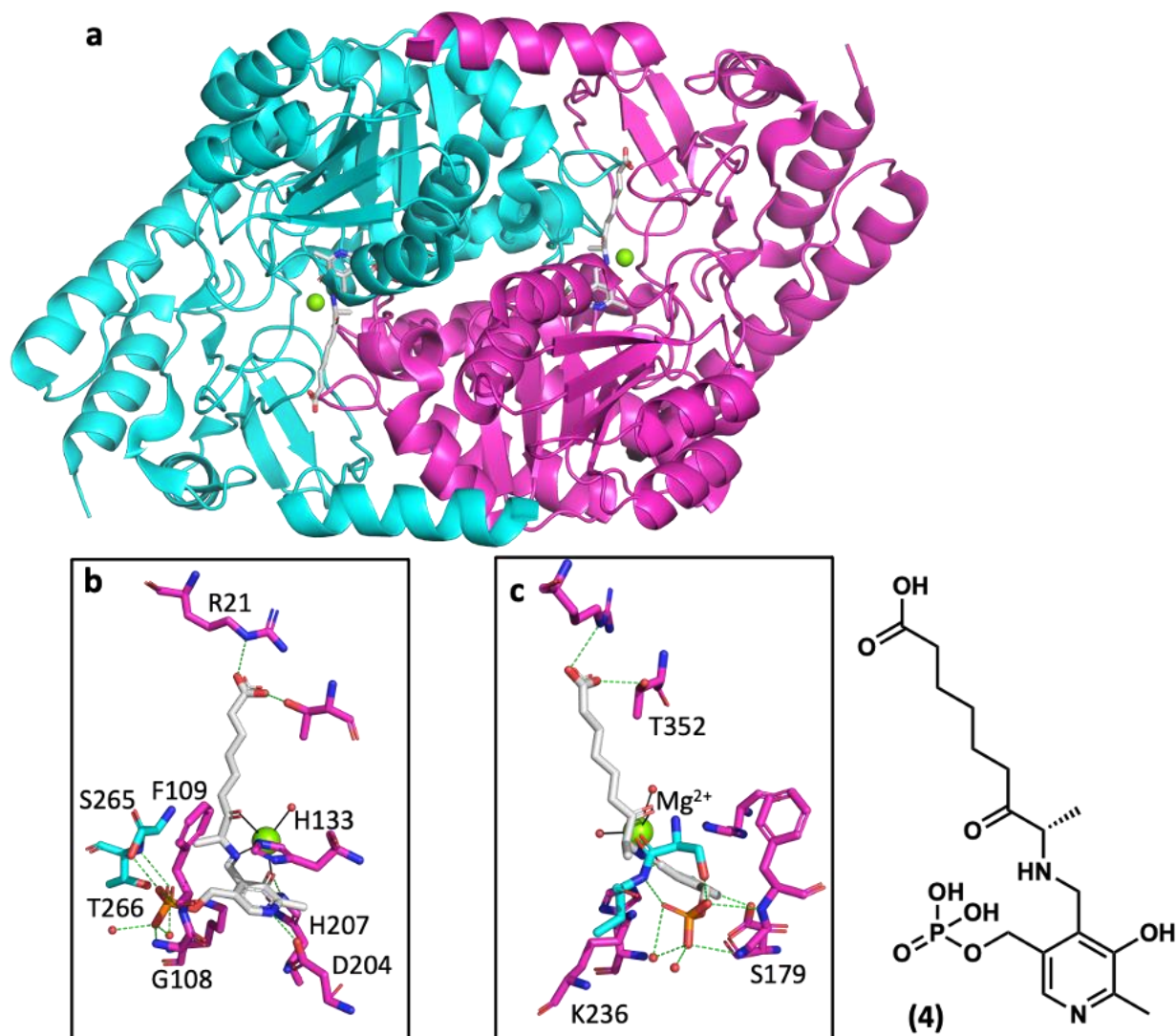


Figure 4.10. Structure of BioF AONS in complex with its reaction intermediate (4) (PDB: IDJ9).

The BioF AONS functions in a homodimer complex (**a**). Two identical active sites are formed at the dimerization interface to bind two individual substrates. Protein structure is shown in the cartoon view, and two identical protein chains are colored in cyan and magenta. (**b,c**) BioF AONS reaction intermediate (**4**) is coordinated by residues from the two identical proteins (pink and blue). Metal coordination bonds are shown as solid black lines, and hydrogen bonds as dashed green lines. Mg²⁺ is depicted as a green sphere and water molecules as red spheres. (**b**) and (**c**) are related by a 90 °C rotation on the Y-axis. Modeled (**4**) is shown in stick form (red, blue (N), orange (P), and white (C)).

Figure 4.11. Sequence alignments of SxtA AONS and its structural homologs.

PDB code of each homolog is listed on the left. BioF and VsAOS1 AONS mentioned in this chapter have the PDB code 1DJ9 and 7V58, respectively. Residues involved in ligand coordination of BioF are indicated with purple circles.

4.3 Materials and Methods

4.3.1 Plasmid preparation

DNA (pMCSG7-GphF_498_705 and pMCSG7-CurA_219-439) encoding the GphF DC (residues 498-705; GenBank [KF479198.1](#)) and CurA DC (residues 219-439; GenBank: [AEE88289.1](#)) were provided by Meredith Skiba and DNA (pMCSG7-SxtA_822-1243) encoding the SxtA AONS (residues 822-1243, GenBank: [WP_009343302.1](#)) was gifted by Stephanie Chun. All *gphF* and *curA* site-directed mutants were introduced using the QuikChange (Agilent) protocol. All PCR primers are listed in **Table 5.2**. All constructs and mutations were verified by Sanger sequencing at Genewiz sequencing core.

4.3.2 Bacterial expression

All plasmids were transformed into *Escherichia coli* strain BL21(DE3). Cell cultures were grown at 37 °C in 0.5 L Terrific Broth (TB) with 100 µg mL⁻¹ ampicillin until OD₆₀₀ reached 1–2, then cooled to 20°C over 0.5–1 hr, induced with 200 µM IPTG, and grown overnight.

4.3.3 Purification of GphF DC, CurA DC and SxtA AONS

Cell pellets from 0.5 L cultures were resuspended in 35 mL Buffer A (50 mM Tris pH 7.4, 300 mM NaCl, 10% (v/v) glycerol) with 0.1 mg mL⁻¹ lysozyme, 0.05 mg mL⁻¹ DNase, 2 mM MgCl₂, 20 mM imidazole. Resuspended cells were incubated on ice for 30 min, lysed by

sonication and centrifuged at 38,650 x g, for 20 min. The soluble fraction was then filtered through a 0.45 μm MILLEX-HP membrane and loaded onto a 5 mL His trap column (cytiva) pre-equilibrated with Buffer A. The column was washed with 50 mL Buffer A and eluted with a 50 mL gradient of 20–400 mM imidazole in Buffer A. For CurA DC, the N-terminal His tag was removed by overnight dialysis at 4°C in the presence of tobacco etch virus (TEV) protease⁸³ and 2–5 mM dithiothreitol (DTT) at a 50:1 molar ratio of CurA DC:protease. The mixture was reapplied to the His-trap column to remove uncleaved CurA DC and the protease. GphF DC, CurA DC and SxtA AONS proteins were further purified via HiLoad Superdex S200 or S75 (Cytiva) gel filtration chromatography with Buffer B (50 mM Tris pH 7.4, 50 mM NaCl, 10% (v/v) glycerol). The GphF and CurA DC eluted as a monomer with apparent molecular weight 25 kDa and were concentrated to 20 mg mL⁻¹ and stored in aliquots at –80°C. The AONS eluted as dimer with molecular weight of 100 kDa and were concentrated to 10 mg mL⁻¹ and stored in aliquots at –80°C.

4.3.4 Protein crystallization and structure determination

His-tagged GphF DC S626A was purified as previously described⁴⁴ and crystallized at 20°C by vapor diffusion from a 2:1 μL mixture of protein stock (20 mg mL⁻¹ in Buffer B) and well solution (30-35% PEG3350, 0.23-0.3M Ammonium acetate, 0.1M Bis-Tris and HCl pH5.5). Microseeding was used to obtain single crystals. CurA DC T355V was also purified as previously described⁴⁴ and crystallized at 20°C by vapor diffusion from a 1:1 μL mixture of protein stock (13 mg mL⁻¹ in Buffer B) and well solution (100mM Bis-Tris pH 6.8, 100mM NaCl, 1.5M ammonium sulfate and 20% glycerol). Microseeding was used to obtain single crystals. Crystals were harvested and stored in liquid nitrogen. Diffraction data were collected at beamline 23ID-B (GM/CA@APS) and processed using XDS. The GphF and CurA DC variants

structures were solved by molecular replacement from the wild type structures (PDB:2REF and 6MFD) using Phaser. Model building was done with *Coot* and refinement with phenix.refine. CurA crystals are not in the best quality (such as having poor completeness %). We are in the progress of optimizing the CurA T355V crystal. Structure validation was done with MolProbity¹¹², figures were prepared in PyMol, and sequence alignments were created using Clustal in Jalview^{113, 114}

4.3.5 Decarboxylation

Reaction mixtures and assay conditions were identical to those for the methylation assay mentioned in chapter 3, excepting the omission of metal to prevent any methylation activity.

4.3.6 AONS assay and assay analysis by LC-MS

Reaction mixtures contained 8 μ M SxtA MT-DC F458Y/Q459H/I204T and wild type, 8 μ M SxtA AONS, 250 μ M Mal-ACP, 1 mM SAM and 0.5 mM MnCl₂, 2 mM PLP, 2 mM L-Arginine in 50 mM HEPES pH 7.8, 150 mM NaCl. Reactions were initiated by an incubation at 30°C. Aliquots were removed at 4 h and quenched with 10% (v/v) formic acid. Precipitate was pelleted at 12,000 x g for 15 min. The residual protein in supernatant was then precipitated with 1:3 (v/v) supernatant and acetonitrile. Insoluble material in the quenched reaction mixture was removed by centrifugation (13,000 rpm for 15 min). Protein in reaction mixtures were precipitated Reaction mixtures were analyzed using the intact protein method on an Agilent Q-TOF 6545 instrument), and the clarified reaction mixture (0.5 μ L) was loaded onto a Waters Acquity 1.7 μ m UPLC BEH Amide HILIC 2.1 x 100 mm column at flow rate of 0.3mL/min in 0.2% (v/v) formic acid and separated with a gradient of 85-60% acetonitrile in 0.2% (v/v) formic acid over 15 mins. MS operating conditions were 300 V fragment voltage, 75 V skimmer

voltage, 100 V nozzle voltage, 350 °C sheath gas temperature, 325 °C drying gas temperature. B at 0.3 mL/min for 2 min, followed by a linear gradient to 75% B at 0.4 mL/min over 3 min and a second linear gradient to 60% B over 0.5 min, 60% B for 1 min and then 6.5 min re-equilibration at 85% B at 0.3 mL/min (total time 15 min). The MassHunter Qualitative Analysis Software (Agilent) was used for analysis of mass spectra, based on extracted ion counts (EIC) for AONS products.

4.3.7 AONS structure prediction and substrate modeling

Predicted AONS structure was obtained from the AlphaFold2-ColabFold server. AONS reaction intermediate ((3) in Figure 4.9) is modeled into the structure using PDB IDJ9 as a reference in Pymol.

Chapter 5 Conclusions and Future Directions

5.1 Overview

In this work, we report the biochemical and structural characterization of the MT, DC, and AONS domains of the SxtA starter module. Investigation of the MT activity and the underlying mechanisms of controlling methylation extent facilitated the successful engineering of SxtA MT to generate a dimethylated product. This resulted in the transfer of an additional methyl group compared to the wild type MT. Surprisingly, this dimethylated product is compatible with downstream pathway processing by SxtA DC and AONS to generate methylated SxtA precursors (**Figure 5.3 & 5.8**). This work contributes to the development of MTs as biocatalysts for synthetically challenging stereo- and site-selective methylation. Engineered SxtA MT, other similar MTs in other pathways, may lead to the production of a library of novel methylated saxitoxin analogs, which could have altered bioactivities and reduced inherent toxicity.

5.1.1 Structural comparison of PKS starter and extender MTs reveals substrate binding features

The starter SxtA C-MT adapted the metal-mediated catalytic mechanism to initiate saxitoxin biosynthesis. It shares <15% sequence identity with extender CurJ MT in the curacin biosynthesis pathway. Nonetheless, they likely share a common ancestor because their MT core sub-domains possess structural features of the Class I MT superfamily enzymes. In addition, they have a helical insertion at the same site within their MT core that constructs their substrate and cofactor binding pocket. This SxtA and

CurJ MTs structural insertion exhibits high sequence variation, possibly explaining why SxtA MT prefers a metal cofactor and acts on malonyl-ACP, while CurJ MT accepts a more extended β -keto polyketide substrate. A conserved His-Glu dyad is found in both CurJ and SxtA MT. In CurJ MT, the dyad deprotonates the substrate α -carbon to generate a carbanion nucleophile for methylation; however, SxtA MT instead uses this dyad to coordinate the metal. Furthermore, the SxtA MT has a large MT lid sub-domain and a metal coordination sphere which is not present in the CurJ MT. These structural similarities solidify their evolutionary relationship, while their differences explain their divergent catalytic mechanism, metal requirement, and substrate specificity.

5.1.2 PKS starter MTs require a permissive filter for the dimethylated product

SxtA and AprA MTs share high sequence similarity (54%) but prefer different metal ions for catalysis. SxtA MT transfers one methyl group onto malonyl-ACP, while AprA MT1 can perform this reaction twice. In AprA MT1, metal specificity also contributes to the control of methylation extent (monomethylation (Fe^{3+}); dimethylation (Mn^{2+} , Mg^{2+} , Co^{2+} and other divalent cations)).

My structural studies and sequence comparisons helped elucidate critical features that control methylation extent¹²⁵. An isoleucine side chain in the SxtA active site inhibited dimethylation due to steric bulk that could not allow space for a second methylation event. In contrast, the dimethylating AprA MT1 has a threonine at a similar site to the SxtA isoleucine. This threonine side chain can adopt a different rotameric position to provide adequate space for the second methyl transfer (**Figure 4.8**).

Other critical features to control methylation extent include the substitution of a metal ligand (from histidine to glutamine) and a catalytic base to remove the remaining α -proton of MeMal-ACP, which has a higher pK_a than Mal-ACP. A substitution to eliminate the decarboxylation activity of SxtA DC also promotes dimethylation because an active DC domain forms the monomethylated product more rapidly than the second methyl transfer. However, an inactive DC is not required for dimethylation. During the course of generating a small library of MT variants to identify these critical features, serendipitously, we discovered a faster SxtA MT variant, F458H, which demonstrates more than fivefold

greater catalytic efficiency than the wild type MT. This single substitution increases monomethylation efficiency because it supports the active site structure and reactivity via a secondary sphere interaction with the metal (**Figure 3.6**).

SxtA and AprA MTs share high sequence similarity (54%) but prefer different metal ions for catalysis. SxtA MT transfers one methyl group onto malonyl-ACP, while AprA MT1 can perform this reaction twice. In AprA MT1, metal specificity also contributes to the control of methylation extent (monomethylation (Fe^{3+}); dimethylation (Mn^{2+} , Mg^{2+} , Co^{2+} and other divalent cations)).

My structural studies and sequence comparisons helped elucidate critical features that control methylation extent¹²⁵. An isoleucine side chain in the SxtA active site inhibited dimethylation due to steric bulk that could not allow space for a second methylation event. In contrast, the dimethylating AprA MT1 has a threonine at a similar site to the SxtA isoleucine. This threonine side chain can adopt a different rotameric position to provide adequate space for the second methyl transfer (**Figure 4.8**).

Other critical features to control methylation extent include the substitution of a metal ligand (from histidine to glutamine) and a catalytic base to remove the remaining α -proton of MeMal-ACP, which has a higher pK_a than Mal-ACP. A substitution to eliminate the decarboxylation activity of SxtA DC also promotes dimethylation because an active DC domain forms the monomethylated product more rapidly than the second methyl transfer. However, an inactive DC is not required for dimethylation. During the course of generating a small library of MT variants to identify these critical features, serendipitously, we discovered a faster SxtA MT variant, F458H, which demonstrates more than fivefold greater catalytic efficiency than the wild type MT. This single substitution increases monomethylation efficiency because it supports the active site structure and reactivity via a secondary sphere interaction with the metal (**Figure 3.6**).

5.1.3 Substrate selectivity of PKS DCs is influenced by active pocket size and hydrophobicity

The GNAT-like DC domain was once thought to perform acyl transfer activity to load the acyl-group from acyl-CoA onto the ACP prior to initiation. However, recent data suggests that

the DCs only perform selective decarboxylation to ensure the correct precursor is passed down for further processing in the pathway. For example, CurA and GphF DCs strongly prefer malonyl- and dimethylmalonyl-ACP, respectively, correlating with the production of their pathway precursors. We tested the activity of SxtA DC on the dimethylated product of the engineered SxtA MT and surprisingly, SxtA catalyzed a significant amount of decarboxylation on this non-native dimethylmalonyl-substrate.

Pre-existing crystal structures of the CurA, GphF, and SxtA DCs with manually modeled dimethylmalonyl CoA provided insight to identify features determining substrate selectivity. The active site clefts to bind the malonyl-group are all differently sized across the three DCs. GphF DC has the largest active site cleft among the three DC, possibly explaining its preference for dimethylmalonyl-ACP over methylmalonyl- or malonyl-ACP. Vice versa, CurA DC, which prefers malonyl-ACP, has the smallest active site cleft.

5.1.4 AONS structure and activity

We investigated the potential influence an engineered MT has on the chemical outcome of the SxtA module. As mentioned previously, SxtA DC processed and consume the dimethylated product to generate isobutyryl-ACP. Then, the AONS also accepted this non-native substrate and performed C-C condensation with arginine to yield a saxitoxin precursor with an additional methyl group. The AONS structure in complex with its reaction intermediate was predicted by alpha-fold as a symmetrical homodimer. Each homodimer binds two substrates between their dimerizing interfaces. This interaction may be essential to facilitating dimerization of the whole SxtA module, and modular dimerization is important for polyketide processing. MT-DC are monomers in solution, suggesting they have a lower affinity to form a homodimer.

5.2 Future Directions

5.2.1 Investigate and expand the substrate scope of SxtA MT

Insights into the catalytic mechanism and structure of SxtA MT imply developing this MT as a biocatalyst to perform direct and selective methylation on chemicals under mild in-vitro reaction conditions. Simple substitution of a few residues in SxtA MT can significantly boost its catalytic efficiency and introduce an additional methyl transfer step. However, the challenge that remains before this MT can be exploited to its full potential is to examine and expand the substrate scope while retaining the selectivity of the reaction.

Whether the SxtA active site can accommodate a variety of substrates other than malonyl- or methylmalonyl-ACP can be investigated using synthetic substrate mimics. The AprA MT crystal structures suggest that the metal center and the surrounding the architecture could accommodate various carboxylated substrates, as carboxylated buffer components (tartrate, citrate, and more) bind to the metal center, and exhibit strong electron density¹³².

Features that determine substrate selectivity can be easily identified in the existing SxtA MT structure with substrate mimics. In addition, the molecular dynamic simulation may provide a view of additional substrate and protein interaction that is not available in a static protein structure. From features identified through these methods, the enzyme can be engineered via amino acid substitution to alter the substrate selectivity to accommodate substrates of interest.

5.2.2 Expanding the MTs utility

MTs naturally catalyze the transfer of an activated methyl group from SAM onto the C-nucleophile of their substrate. SAH serves as a leaving group during this SN₂ MT- catalyzed

reaction. The use of SAM analogs could expand the utility of MTs for numerous novel applications such as diversification of the product of a biosynthesis pathway⁷¹⁻⁷³. For instance, SAM analogs with an extended methyl group replacement can be used to transfer these activated groups from the sulfonium center onto the substrates for targeted functionalization. Examples of the extended methyl group include but are not limited to alkyl, alkenyl, and alkynyl side chains. They are easily obtained in a one-step chemo-selective alkylation of SAH with alkyl triflates¹³³. In addition, the engineered SxtA MT can also be repurposed to transfer two alkyl groups from a SAM analog onto the malonyl-substrate. Alkylation of malonyl-ACP with SAM analogs may potentially lead to the production of novel saxitoxin derivatives.

5.2.3 Understanding the full SxtA module architecture

Structural information of the intact SxtA module is essential to understand saxitoxin biosynthesis fully. Interdomain interactions and linkers contribute to how the substrate is passed onto the following enzyme domains for catalysis. Also, PKS modules function in a dimeric form^{81, 82}, in contrast to the monomeric functioning NRPS¹³⁴. The underlying reasons explaining why modular PKS dimerization is essential for PKS function is not yet identified. Module dimerization may help control the interaction between ACPs and each catalytic domain according to the proper reaction order. The KS, DH and ER domains mediate the dimerization of the whole module⁸¹. However, the SxtA module does not contain these domains. Instead, the AONS is proposed to mediate dimerization of the module because it is a homodimer in solution. Structures of the excised SxtA enzymes (MT-DC (as described in this thesis) and AONS (predicted by AlphdFold) may not provide view of these domains in their native environment. A high-resolution of intact PKS module is important to understanding polyketide processing and

diversification. The high-resolution structure of the intact SxtA module can be obtained through either cryo-electron microscopy (EM) or x-ray crystallography.

5.2.4 Further investigation of substrate selectivity of SxtA, GphF and CurA DCs

CurA, SxtA and GphF DCs, the downstream domain following a methyltransferase (except for Curacin DC, which follows a truncated, inactive MT), selectively decarboxylate the product of the MT to generate acetyl-, propionyl- or isobutyryl-ACP; the precursor of curacin, saxitoxin and gephyronic acid, respectively. High-resolution structures of CurA, SxtA and GphF DCs with their substrates, malonyl-, methylmalonyl- and dimethylmalonyl- ACP will provide structural details responsible for the substrate selectivity. However, the DCs decarboxylate the substrates during crystallization conditions. Therefore, an inactive version of the DCs will be used for structural determination in complex with the substrate.

Bibliography

Rubin, Elyse. " The Dissertation Handbook: A Guide to Submitting Your Doctoral Dissertation and Completing Your Doctoral Degree Requirements." Diss. U of Michigan, 2017

1. Webster, S. P.; Alexeev, D.; Campopiano, D. J.; Watt, R. M.; Alexeeva, M.; Sawyer, L.; Baxter, R. L., Mechanism of 8-amino-7-oxononanoate synthase: spectroscopic, kinetic, and crystallographic studies. *Biochemistry* **2000**, *39* (3), 516-28.
2. Newman, D. J.; Cragg, G. M., Natural Products as Sources of New Drugs over the Nearly Four Decades from 01/1981 to 09/2019. *J Nat Prod* **2020**, *83* (3), 770-803.
3. Challis, G. L.; Hopwood, D. A., Synergy and contingency as driving forces for the evolution of multiple secondary metabolite production by *Streptomyces* species. *Proc Natl Acad Sci U S A* **2003**, *100 Suppl 2* (Suppl 2), 14555-61.
4. Egan, S.; Harder, T.; Burke, C.; Steinberg, P.; Kjelleberg, S.; Thomas, T., The seaweed holobiont: understanding seaweed-bacteria interactions. *FEMS Microbiol Rev* **2013**, *37* (3), 462-76.
5. Molloy, E. M.; Hertweck, C., Antimicrobial discovery inspired by ecological interactions. *Curr Opin Microbiol* **2017**, *39*, 121-127.
6. Seyedsayamdost, M. R.; Case, R. J.; Kolter, R.; Clardy, J., The Jekyll-and-Hyde chemistry of *Phaeobacter gallaeciensis*. *Nat Chem* **2011**, *3* (4), 331-5.
7. Cevizci, D.; Ulug, D.; Cimen, H.; Touray, M.; Hazir, S.; Cakmak, I., Mode of entry of secondary metabolites of the bacteria *Xenorhabdus szentirmaii* and *X. nematophila* into *Tetranychus urticae*, and their toxicity to the predatory mites *Phytoseiulus persimilis* and *Neoseiulus californicus*. *J Invertebr Pathol* **2020**, *174*, 107418.
8. Huitu, O.; Forbes, K. M.; Helander, M.; Julkunen-Tiitto, R.; Lambin, X.; Saikkonen, K.; Stuart, P.; Sulkama, S.; Hartley, S., Silicon, endophytes and secondary metabolites as grass defenses against mammalian herbivores. *Front Plant Sci* **2014**, *5*, 478.
9. Pan, L.; Ren, L.; Chen, F.; Feng, Y.; Luo, Y., Antifeedant Activity of Ginkgo biloba Secondary Metabolites against *Hyphantria cunea* Larvae: Mechanisms and Applications. *PLoS One* **2016**, *11* (5), e0155682.
10. Stratton, C. F.; Newman, D. J.; Tan, D. S., Cheminformatic comparison of approved drugs from natural product versus synthetic origins. *Bioorg Med Chem Lett* **2015**, *25* (21), 4802-4807.
11. Knudsmark Jessing, K.; Duke, S. O.; Cedergreen, N., Potential ecological roles of artemisinin produced by *Artemisia annua* L. *J Chem Ecol* **2014**, *40* (2), 100-17.
12. Clemensen, A. K.; Provenza, F. D.; Hendrickson, J. R.; Grusak, M. A., Ecological Implications of Plant Secondary Metabolites - Phytochemical Diversity Can Enhance Agricultural Sustainability. *Frontiers in Sustainable Food Systems* **2020**, *4*.

13. Dias, D. A.; Urban, S.; Roessner, U., A historical overview of natural products in drug discovery. *Metabolites* **2012**, *2* (2), 303-36.
14. Sabbagh, F.; Muhamad, I. I., Production of poly-hydroxyalkanoate as secondary metabolite with main focus on sustainable energy. *Renewable and Sustainable Energy Reviews* **2017**, *72*, 95-104.
15. Krishna, S.; Bustamante, L.; Haynes, R. K.; Staines, H. M., Artemisinins: their growing importance in medicine. *Trends Pharmacol Sci* **2008**, *29* (10), 520-7.
16. Fuzimoto, A. D., An overview of the anti-SARS-CoV-2 properties of *Artemisia annua*, its antiviral action, protein-associated mechanisms, and repurposing for COVID-19 treatment. *J Integr Med* **2021**, *19* (5), 375-388.
17. Cragg, G. M.; Newman, D. J., Biodiversity: A continuing source of novel drug leads. *Pure and Applied Chemistry* **2005**, *77* (1), 7-24.
18. Schmitz, R., Friedrich Wilhelm Sertürner and the discovery of morphine. *Pharm Hist* **1985**, *27* (2), 61-74.
19. Pham, V. H.; Kim, J., Cultivation of unculturable soil bacteria. *Trends Biotechnol* **2012**, *30* (9), 475-84.
20. Pye, C. R.; Bertin, M. J.; Lokey, R. S.; Gerwick, W. H.; Linington, R. G., Retrospective analysis of natural products provides insights for future discovery trends. *Proc Natl Acad Sci U S A* **2017**, *114* (22), 5601-5606.
21. Bertrand, R. L.; Sorensen, J. L., A comprehensive catalogue of polyketide synthase gene clusters in lichenizing fungi. *J Ind Microbiol Biotechnol* **2018**, *45* (12), 1067-1081.
22. Chiang, Y. M.; Szewczyk, E.; Davidson, A. D.; Keller, N.; Oakley, B. R.; Wang, C. C. C., A Gene Cluster Containing Two Fungal Polyketide Synthases Encodes the Biosynthetic Pathway for a Polyketide, Asperfuranone, in *Aspergillus nidulans*. *J. Am. Chem. Soc.* **2009**, *131*, 2965.
23. McDaniel, R.; Thamchaipenet, A.; Gustafsson, C.; Fu, H.; Betlach, M.; Ashley, G., Multiple genetic modifications of the erythromycin polyketide synthase to produce a library of novel "unnatural" natural products. *Proc Natl Acad Sci U S A* **1999**, *96* (5), 1846-51.
24. Felnagle, E. A.; Jackson, E. E.; Chan, Y. A.; Podevels, A. M.; Berti, A. D.; McMahon, M. D.; Thomas, M. G., Nonribosomal peptide synthetases involved in the production of medically relevant natural products. *Mol Pharm* **2008**, *5* (2), 191-211.
25. Mizuno, C. M.; Kimes, N. E.; López-Pérez, M.; Ausó, E.; Rodríguez-Valera, F.; Ghai, R., A hybrid NRPS-PKS gene cluster related to the bleomycin family of antitumor antibiotics in *Alteromonas macleodii* strains. *PLoS One* **2013**, *8* (9), e76021.
26. Weissman, K. J., The structural biology of biosynthetic megaenzymes. *Nat Chem Biol* **2015**, *11* (9), 660-70.
27. Staunton, J.; Weissman, K. J., Polyketide biosynthesis: a millennium review. *Nat Prod Rep* **2001**, *18* (4), 380-416.
28. Hertweck, C.; Luzhetskyy, A.; Rebets, Y.; Bechthold, A., Type II polyketide synthases: gaining a deeper insight into enzymatic teamwork. *Nat Prod Rep* **2007**, *24* (1), 162-90.
29. Byers, D. M.; Gong, H., Acyl carrier protein: structure-function relationships in a conserved multifunctional protein family. *Biochem Cell Biol* **2007**, *85* (6), 649-62.
30. Abe, I.; Morita, H., Structure and function of the chalcone synthase superfamily of plant type III polyketide synthases. *Nat Prod Rep* **2010**, *27* (6), 809-38.
31. Katsuyama, Y.; Ohnishi, Y., Type III polyketide synthases in microorganisms. *Methods Enzymol* **2012**, *515*, 359-77.

32. Cortes, J.; Haydock, S. F.; Roberts, G. A.; Bevitt, D. J.; Leadlay, P. F., An unusually large multifunctional polypeptide in the erythromycin-producing polyketide synthase of *Saccharopolyspora erythraea*. *Nature* **1990**, *348* (6297), 176-8.
33. Donadio, S.; Staver, M. J.; McAlpine, J. B.; Swanson, S. J.; Katz, L., Modular organization of genes required for complex polyketide biosynthesis. *Science* **1991**, *252* (5006), 675-9.
34. Su, L.; Hôtel, L.; Paris, C.; Chepkirui, C.; Brachmann, A. O.; Piel, J.; Jacob, C.; Aigle, B.; Weissman, K. J., Engineering the stambomycin modular polyketide synthase yields 37-membered mini-stambomycins. *Nat Commun* **2022**, *13* (1), 515.
35. Wang, H.; Liang, J.; Yue, Q.; Li, L.; Shi, Y.; Chen, G.; Li, Y. Z.; Bian, X.; Zhang, Y.; Zhao, G.; Ding, X., Engineering the acyltransferase domain of epothilone polyketide synthase to alter the substrate specificity. *Microb Cell Fact* **2021**, *20* (1), 86.
36. Robbins, T.; Kapilivsky, J.; Cane, D. E.; Khosla, C., Roles of Conserved Active Site Residues in the Ketosynthase Domain of an Assembly Line Polyketide Synthase. *Biochemistry* **2016**, *55* (32), 4476-84.
37. Fischbach, M. A.; Walsh, C. T., Assembly-Line Enzymology for Polyketide and Nonribosomal Peptide Antibiotics: Logic, Machinery, and Mechanisms. *Chemical Reviews* **2006**, *106* (8), 3468-3496.
38. Hertweck, C., The biosynthetic logic of polyketide diversity. *Angew Chem Int Ed Engl* **2009**, *48* (26), 4688-716.
39. Ames, B. D.; Nguyen, C.; Bruegger, J.; Smith, P.; Xu, W.; Ma, S.; Wong, E.; Wong, S.; Xie, X.; Li, J. W.; Vederas, J. C.; Tang, Y.; Tsai, S. C., Crystal structure and biochemical studies of the trans-acting polyketide enoyl reductase LovC from lovastatin biosynthesis. *Proc Natl Acad Sci U S A* **2012**, *109* (28), 11144-9.
40. Ma, S. M.; Li, J. W.; Choi, J. W.; Zhou, H.; Lee, K. K.; Moorthie, V. A.; Xie, X.; Kealey, J. T.; Da Silva, N. A.; Vederas, J. C.; Tang, Y., Complete reconstitution of a highly reducing iterative polyketide synthase. *Science* **2009**, *326* (5952), 589-92.
41. Li, Y.; Dodge, G. J.; Fiers, W. D.; Fecik, R. A.; Smith, J. L.; Aldrich, C. C., Functional Characterization of a Dehydratase Domain from the Pikromycin Polyketide Synthase. *J Am Chem Soc* **2015**, *137* (22), 7003-6.
42. Skiba, M. A.; Sikkema, A. P.; Fiers, W. D.; Gerwick, W. H.; Sherman, D. H.; Aldrich, C. C.; Smith, J. L., Domain Organization and Active Site Architecture of a Polyketide Synthase C-methyltransferase. *ACS Chem Biol* **2016**, *11* (12), 3319-3327.
43. Skiba, M. A.; Sikkema, A. P.; Moss, N. A.; Lowell, A. N.; Su, M.; Sturgis, R. M.; Gerwick, L.; Gerwick, W. H.; Sherman, D. H.; Smith, J. L., Biosynthesis of t-Butyl in Apratoxin A: Functional Analysis and Architecture of a PKS Loading Module. *ACS Chem Biol* **2018**, *13* (6), 1640-1650.
44. Skiba, M. A.; Sikkema, A. P.; Moss, N. A.; Tran, C. L.; Sturgis, R. M.; Gerwick, L.; Gerwick, W. H.; Sherman, D. H.; Smith, J. L., A Mononuclear Iron-Dependent Methyltransferase Catalyzes Initial Steps in Assembly of the Apratoxin A Polyketide Starter Unit. *ACS Chem Biol* **2017**, *12* (12), 3039-3048.
45. Zhao, S.; Ni, F.; Qiu, T.; Wolff, J. T.; Tsai, S. C.; Luo, R., Molecular Basis for Polyketide Ketoreductase-Substrate Interactions. *Int J Mol Sci* **2020**, *21* (20).
46. Gokhale, R. S.; Hunziker, D.; Cane, D. E.; Khosla, C., Mechanism and specificity of the terminal thioesterase domain from the erythromycin polyketide synthase. *Chem Biol* **1999**, *6* (2), 117-25.

47. Korman, T. P.; Crawford, J. M.; Labonte, J. W.; Newman, A. G.; Wong, J.; Townsend, C. A.; Tsai, S. C., Structure and function of an iterative polyketide synthase thioesterase domain catalyzing Claisen cyclization in aflatoxin biosynthesis. *Proc Natl Acad Sci U S A* **2010**, *107* (14), 6246-51.
48. Liu, L.; Zhang, Z.; Shao, C. L.; Wang, C. Y., Analysis of the Sequences, Structures, and Functions of Product-Releasing Enzyme Domains in Fungal Polyketide Synthases. *Front Microbiol* **2017**, *8*, 1685.
49. Cheng, Y. Q.; Tang, G. L.; Shen, B., Type I polyketide synthase requiring a discrete acyltransferase for polyketide biosynthesis. *Proc Natl Acad Sci U S A* **2003**, *100* (6), 3149-54.
50. Young, J.; Stevens, D. C.; Carmichael, R.; Tan, J.; Rachid, S.; Boddy, C. N.; Müller, R.; Taylor, R. E., Elucidation of gephyronic acid biosynthetic pathway revealed unexpected SAM-dependent methylations. *J Nat Prod* **2013**, *76* (12), 2269-76.
51. Skiba, M. A.; Tran, C. L.; Dan, Q.; Sikkema, A. P.; Klaver, Z.; Gerwick, W. H.; Sherman, D. H.; Smith, J. L., Repurposing the GNAT Fold in the Initiation of Polyketide Biosynthesis. *Structure* **2020**, *28* (1), 63-74.e4.
52. Struck, A. W.; Thompson, M. L.; Wong, L. S.; Micklefield, J., S-adenosyl-methionine-dependent methyltransferases: highly versatile enzymes in biocatalysis, biosynthesis and other biotechnological applications. *Chembiochem* **2012**, *13* (18), 2642-55.
53. Liscombe, D. K.; Louie, G. V.; Noel, J. P., Architectures, mechanisms and molecular evolution of natural product methyltransferases. *Nat Prod Rep* **2012**, *29* (10), 1238-50.
54. Wlodarski, T.; Kutner, J.; Towpik, J.; Knizewski, L.; Rychlewski, L.; Kudlicki, A.; Rowicka, M.; Dziembowski, A.; Ginalski, K., Comprehensive structural and substrate specificity classification of the *Saccharomyces cerevisiae* methyltransferome. *PLoS One* **2011**, *6* (8), e23168.
55. Hanukoglu, I., Proteopedia: Rossmann fold: A beta-alpha-beta fold at dinucleotide binding sites. *Biochem Mol Biol Educ* **2015**, *43* (3), 206-9.
56. Zubieta, C.; Ross, J. R.; Koscheski, P.; Yang, Y.; Pichersky, E.; Noel, J. P., Structural basis for substrate recognition in the salicylic acid carboxyl methyltransferase family. *Plant Cell* **2003**, *15* (8), 1704-16.
57. Jansson, A.; Koskiniemi, H.; Mäntsälä, P.; Niemi, J.; Schneider, G., Crystal structure of a ternary complex of DnrK, a methyltransferase in daunorubicin biosynthesis, with bound products. *J Biol Chem* **2004**, *279* (39), 41149-56.
58. Gu, L.; Geders, T. W.; Wang, B.; Gerwick, W. H.; Håkansson, K.; Smith, J. L.; Sherman, D. H., GNAT-like strategy for polyketide chain initiation. *Science* **2007**, *318* (5852), 970-4.
59. Mattheus, W.; Gao, L. J.; Herdewijn, P.; Landuyt, B.; Verhaegen, J.; Masschelein, J.; Volckaert, G.; Lavigne, R., Isolation and purification of a new kalimantacin/batumin-related polyketide antibiotic and elucidation of its biosynthesis gene cluster. *Chem Biol* **2010**, *17* (2), 149-59.
60. Shishido, T. K.; Wahlsten, M.; Laine, P.; Rikkinen, J.; Lundell, T.; Auvinen, P., Microbial Communities of Cladonia Lichens and Their Biosynthetic Gene Clusters Potentially Encoding Natural Products. *Microorganisms* **2021**, *9* (7).
61. Klaus, M.; Grininger, M., Correction: Engineering strategies for rational polyketide synthase design. *Nat Prod Rep* **2021**, *38* (7), 1409.

62. Barajas, J. F.; Blake-Hedges, J. M.; Bailey, C. B.; Curran, S.; Keasling, J. D., Engineered polyketides: Synergy between protein and host level engineering. *Synth Syst Biotechnol* **2017**, *2* (3), 147-166.
63. Yi, D.; Acharya, A.; Gumbart, J. C.; Gutekunst, W. R.; Agarwal, V., Gatekeeping Ketosynthases Dictate Initiation of Assembly Line Biosynthesis of Pyrrolic Polyketides. *J Am Chem Soc* **2021**, *143* (20), 7617-7622.
64. Kumar, P.; Li, Q.; Cane, D. E.; Khosla, C., Intermodular communication in modular polyketide synthases: structural and mutational analysis of linker mediated protein-protein recognition. *J Am Chem Soc* **2003**, *125* (14), 4097-102.
65. Tsuji, S. Y.; Cane, D. E.; Khosla, C., Selective protein-protein interactions direct channeling of intermediates between polyketide synthase modules. *Biochemistry* **2001**, *40* (8), 2326-31.
66. Chun, S. W.; Hinze, M. E.; Skiba, M. A.; Narayan, A. R. H., Chemistry of a Unique Polyketide-like Synthase. *J. Am. Chem. Soc.* **2018**, *140*, 2430.
67. Barreiro, E. J.; Kümmerle, A. E.; Fraga, C. A., The methylation effect in medicinal chemistry. *Chem Rev* **2011**, *111* (9), 5215-46.
68. Schönherr, H.; Cernak, T., Profound methyl effects in drug discovery and a call for new C-H methylation reactions. *Angew Chem Int Ed Engl* **2013**, *52* (47), 12256-67.
69. Ghosh, P.; Kwon, N. Y.; Kim, S.; Han, S.; Lee, S. H.; An, W.; Mishra, N. K.; Han, S. B.; Kim, I. S., C-H Methylation of Iminoamido Heterocycles with Sulfur Ylides*. *Angew Chem Int Ed Engl* **2021**, *60* (1), 191-196.
70. Stevens, D. C.; Wagner, D. T.; Manion, H. R.; Alexander, B. K.; Keatinge-Clay, A. T., Methyltransferases excised from trans-AT polyketide synthases operate on N-acetylcysteamine-bound substrates. *J Antibiot (Tokyo)* **2016**, *69* (7), 567-570.
71. Klimasauskas, S.; Weinhold, E., A new tool for biotechnology: AdoMet-dependent methyltransferases. *Trends Biotechnol* **2007**, *25* (3), 99-104.
72. Lukinavicius, G.; Lapiene, V.; Stasevskij, Z.; Dalhoff, C.; Weinhold, E.; Klimasauskas, S., Targeted labeling of DNA by methyltransferase-directed transfer of activated groups (mTAG). *J Am Chem Soc* **2007**, *129* (10), 2758-9.
73. Zhang, J.; Zheng, Y. G., SAM/SAH Analogs as Versatile Tools for SAM-Dependent Methyltransferases. *ACS Chem Biol* **2016**, *11* (3), 583-97.
74. Meinke, J. L.; Mehaffey, M. R.; Wagner, D. T.; Sun, N.; Zhang, Z.; Brodbelt, J. S.; Keatinge-Clay, A. T., Structural and Functional Studies of a gem-Dimethylating Methyltransferase from a trans-Acyltransferase Assembly Line. *ACS Chem Biol* **2018**, *13* (12), 3306-3314.
75. Fischbach, M. A.; Walsh, C. T., Assembly-line enzymology for polyketide and nonribosomal peptide antibiotics: logic, machinery, and mechanisms. *Chem Rev* **2006**, *106* (8), 3468-96.
76. Keatinge-Clay, A. T., The structures of type I polyketide synthases. *Nat Prod Rep* **2012**, *29* (10), 1050-73.
77. Schubert, H. L.; Blumenthal, R. M.; Cheng, X., Many paths to methyltransfer: a chronicle of convergence. *Trends Biochem Sci* **2003**, *28* (6), 329-35.
78. Sudek, S.; Lopanik, N. B.; Waggoner, L. E.; Hildebrand, M.; Anderson, C.; Liu, H.; Patel, A.; Sherman, D. H.; Haygood, M. G., Identification of the putative bryostatin polyketide synthase gene cluster from "Candidatus Endobugula sertula", the uncultivated microbial symbiont of the marine bryozoan Bugula neritina. *J Nat Prod* **2007**, *70* (1), 67-74.

79. Simunovic, V.; Zapp, J.; Rachid, S.; Krug, D.; Meiser, P.; Müller, R., Myxovirescin A biosynthesis is directed by hybrid polyketide synthases/nonribosomal peptide synthetase, 3-hydroxy-3-methylglutaryl-CoA synthases, and trans-acting acyltransferases. *Chembiochem* **2006**, *7* (8), 1206-20.
80. Chun, S. W.; Narayan, A. R. H., Biocatalytic synthesis of α -amino ketones. *Synlett* **2019**, *30* (11), 1269-1274.
81. Aparicio, J. F.; Caffrey, P.; Marsden, A. F.; Staunton, J.; Leadlay, P. F., Limited proteolysis and active-site studies of the first multienzyme component of the erythromycin-producing polyketide synthase. *J Biol Chem* **1994**, *269* (11), 8524-8.
82. Staunton, J.; Caffrey, P.; Aparicio, J. F.; Roberts, G. A.; Bethell, S. S.; Leadlay, P. F., Evidence for a double-helical structure for modular polyketide synthases. *Nat Struct Biol* **1996**, *3* (2), 188-92.
83. Kapust, R. B.; Tözsér, J.; Copeland, T. D.; Waugh, D. S., The P1' specificity of tobacco etch virus protease. *Biochem Biophys Res Commun* **2002**, *294* (5), 949-55.
84. Kabsch, W., Xds. *Acta Crystallogr D Biol Crystallogr* **2010**, *66* (2), 125-132.
85. McCoy, A. J.; Grosse-Kunstleve, R. W.; Adams, P. D.; Winn, M. D.; Storoni, L. C.; Read, R. J., Phaser crystallographic software. *J Appl Crystallogr* **2007**, *40* (Pt 4), 658-674.
86. Liebschner, D.; Afonine, P. V.; Baker, M. L.; Bunkóczi, G.; Chen, V. B.; Croll, T. I.; Hintze, B.; Hung, L. W.; Jain, S.; McCoy, A. J.; Moriarty, N. W.; Oeffner, R. D.; Poon, B. K.; Prisant, M. G.; Read, R. J.; Richardson, J. S.; Richardson, D. C.; Sammito, M. D.; Sobolev, O. V.; Stockwell, D. H.; Terwilliger, T. C.; Urzhumtsev, A. G.; Videau, L. L.; Williams, C. J.; Adams, P. D., Macromolecular structure determination using X-rays, neutrons and electrons: recent developments in Phenix. *Acta Crystallogr D Struct Biol* **2019**, *75* (Pt 10), 861-877.
87. Emsley, P.; Cowtan, K., Coot: model-building tools for molecular graphics. *Acta Crystallogr D Biol Crystallogr* **2004**, *60* (Pt 12 Pt 1), 2126-32.
88. Castillo, M.; Smith, P. C., Disposition and reactivity of ibuprofen and ibufenac acyl glucuronides in vivo in the rhesus monkey and in vitro with human serum albumin. *Drug Metab Dispos* **1995**, *23* (5), 566-72.
89. Johnson, C. H.; Wilson, I. D.; Harding, J. R.; Stachulski, A. V.; Iddon, L.; Nicholson, J. K.; Lindon, J. C., NMR spectroscopic studies on the in vitro acyl glucuronide migration kinetics of Ibuprofen ((+/-)-(R,S)-2-(4-isobutylphenyl) propanoic acid), its metabolites, and analogues. *Anal Chem* **2007**, *79* (22), 8720-7.
90. Wiese, M.; D'Agostino, P. M.; Mihali, T. K.; Moffitt, M. C.; Neilan, B. A., Neurotoxic alkaloids: saxitoxin and its analogs. *Mar Drugs* **2010**, *8* (7), 2185-211.
91. Llewellyn, L. E., Saxitoxin, a toxic marine natural product that targets a multitude of receptors. *Nat Prod Rep* **2006**, *23* (2), 200-22.
92. Shen, H.; Liu, D.; Wu, K.; Lei, J.; Yan, N., Structures of human Na(v)1.7 channel in complex with auxiliary subunits and animal toxins. *Science* **2019**, *363* (6433), 1303-1308.
93. Dusek, R. J.; Smith, M. M.; Van Hemert, C.; Shearn-Bochsler, V. I.; Hall, S.; Ridge, C. D.; Hardison, D. R.; Kaler, R. S. A.; Bodenstein, B. L.; Hofmeister, E. K.; Hall, J. S., Acute oral toxicity and tissue residues of saxitoxin in the mallard (*Anas platyrhynchos*). *Harmful Algae* **2021**, *109*, 102109.
94. Thottumkara, A. P.; Parsons, W. H.; Du Bois, J., Saxitoxin. *Angew Chem Int Ed Engl* **2014**, *53* (23), 5760-84.

95. Lukowski, A. L.; Denomme, N.; Hinze, M. E.; Hall, S.; Isom, L. L.; Narayan, A. R. H., Biocatalytic Detoxification of Paralytic Shellfish Toxins. *ACS Chem Biol* **2019**, *14* (5), 941-948.
96. Cullen, A.; D'Agostino, P. M.; Mazmouz, R.; Pickford, R.; Wood, S.; Neilan, B. A., Insertions within the Saxitoxin Biosynthetic Gene Cluster Result in Differential Toxin Profiles. *ACS Chem Biol* **2018**, *13* (11), 3107-3114.
97. Kellmann, R.; Mihali, T. K.; Jeon, Y. J.; Pickford, R.; Pomati, F.; Neilan, B. A., Biosynthetic intermediate analysis and functional homology reveal a saxitoxin gene cluster in cyanobacteria. *Appl Environ Microbiol* **2008**, *74* (13), 4044-53.
98. Kellmann, R.; Mihali, T. K.; Neilan, B. A., Identification of a saxitoxin biosynthesis gene with a history of frequent horizontal gene transfers. *J Mol Evol* **2008**, *67* (5), 526-38.
99. Mihali, T. K.; Carmichael, W. W.; Neilan, B. A., A putative gene cluster from a *Lyngbya wollei* bloom that encodes paralytic shellfish toxin biosynthesis. *PLoS One* **2011**, *6* (2), e14657.
100. Tsuchiya, S.; Cho, Y.; Yoshioka, R.; Konoki, K.; Nagasawa, K.; Oshima, Y.; Yotsu-Yamashita, M., Synthesis and Identification of Key Biosynthetic Intermediates for the Formation of the Tricyclic Skeleton of Saxitoxin. *Angew Chem Int Ed Engl* **2017**, *56* (19), 5327-5331.
101. Wang, D. Z.; Zhang, S. F.; Zhang, Y.; Lin, L., Paralytic shellfish toxin biosynthesis in cyanobacteria and dinoflagellates: A molecular overview. *J Proteomics* **2016**, *135*, 132-140.
102. Luo, Y.; Li, B. Z.; Liu, D.; Zhang, L.; Chen, Y.; Jia, B.; Zeng, B. X.; Zhao, H.; Yuan, Y. J., Engineered biosynthesis of natural products in heterologous hosts. *Chem Soc Rev* **2015**, *44* (15), 5265-90.
103. Chakrabarty, S.; Romero, E. O.; Pyser, J. B.; Yazarians, J. A.; Narayan, A. R. H., Chemoenzymatic Total Synthesis of Natural Products. *Acc. Chem. Res.* **2021**, *54* (6), 1374-1384.
104. Quadri, L. E.; Weinreb, P. H.; Lei, M.; Nakano, M. M.; Zuber, P.; Walsh, C. T., Characterization of Sfp, a *Bacillus subtilis* phosphopantetheinyl transferase for peptidyl carrier protein domains in peptide synthetases. *Biochemistry* **1998**, *37* (6), 1585-95.
105. Sánchez, C.; Du, L.; Edwards, D. J.; Toney, M. D.; Shen, B., Cloning and characterization of a phosphopantetheinyl transferase from *Streptomyces verticillus* ATCC15003, the producer of the hybrid peptide-polyketide antitumor drug bleomycin. *Chem Biol* **2001**, *8* (7), 725-38.
106. Meluzzi, D.; Zheng, W. H.; Hensler, M.; Nizet, V.; Dorrestein, P. C., Top-down mass spectrometry on low-resolution instruments: characterization of phosphopantetheinylated carrier domains in polyketide and non-ribosomal biosynthetic pathways. *Bioorg Med Chem Lett* **2008**, *18* (10), 3107-11.
107. Arnett, E. M.; Maroldo, S. G.; Schilling, S. L.; Harrelson, J. A., Ion pairing and reactivity of enolate anions. 5. Thermodynamics of ionization of β -di- and tricarbonyl compounds in dimethyl sulfoxide solution and ion pairing of their alkali salts. *J Am Chem Soc* **1984**, *106* (22), 6759-6767.
108. Span, E. A.; Suess, D. L. M.; Deller, M. C.; Britt, R. D.; Marletta, M. A., The Role of the Secondary Coordination Sphere in a Fungal Polysaccharide Monooxygenase. *ACS Chem Biol* **2017**, *12* (4), 1095-1103.
109. Dudev, T.; Lin, D.; Dudev, M.; Lim, C., First-Second Shell Interactions in Metal Binding Sites in Proteins: A PDB Survey and DFT/CDM Calculations. *J Am Chem Soc* **2003**, *125* (10), 3168-3180.
110. Mazmanian, K.; Dudev, T.; Lim, C., How First Shell-Second Shell Interactions and Metal Substitution Modulate Protein Function. *Inorg Chem* **2018**, *57* (22), 14052-14061.

111. Skiba, M. A.; Maloney, F. P.; Dan, Q.; Fraley, A. E.; Aldrich, C. C.; Smith, J. L.; Brown, W. C., PKS-NRPS Enzymology and Structural Biology: Considerations in Protein Production. *Methods Enzymol* **2018**, *604*, 45-88.
112. Chen, V. B.; Arendall, W. B., 3rd; Headd, J. J.; Keedy, D. A.; Immormino, R. M.; Kapral, G. J.; Murray, L. W.; Richardson, J. S.; Richardson, D. C., MolProbity: all-atom structure validation for macromolecular crystallography. *Acta Crystallogr D Biol Crystallogr* **2010**, *66* (Pt 1), 12-21.
113. Larkin, M. A.; Blackshields, G.; Brown, N. P.; Chenna, R.; McGettigan, P. A.; McWilliam, H.; Valentin, F.; Wallace, I. M.; Wilm, A.; Lopez, R.; Thompson, J. D.; Gibson, T. J.; Higgins, D. G., Clustal W and Clustal X version 2.0. *Bioinformatics* **2007**, *23* (21), 2947-8.
114. Waterhouse, A. M.; Procter, J. B.; Martin, D. M.; Clamp, M.; Barton, G. J., Jalview Version 2--a multiple sequence alignment editor and analysis workbench. *Bioinformatics* **2009**, *25* (9), 1189-91.
115. Johnson, K. A., New standards for collecting and fitting steady state kinetic data. *Beilstein J Org Chem* **2019**, *15*, 16-29.
116. Dorrestein, P. C.; Bumpus, S. B.; Calderone, C. T.; Garneau-Tsodikova, S.; Aron, Z. D.; Straight, P. D.; Kolter, R.; Walsh, C. T.; Kelleher, N. L., Facile detection of acyl and peptidyl intermediates on thiotemplate carrier domains via phosphopantetheinyl elimination reactions during tandem mass spectrometry. *Biochemistry* **2006**, *45* (42), 12756-66.
117. Hinzpeter, J.; Barrientos, C.; Zamorano, Á.; Martínez, Á.; Palet, M.; Wulf, R.; Barahona, M.; Sepúlveda, J. M.; Guerra, M.; Bustamante, T.; Del Campo, M.; Tapia, E.; Lagos, N., Gonyautoxins: First evidence in pain management in total knee arthroplasty. *Toxicol* **2016**, *119*, 180-5.
118. Selwood, A. I.; Waugh, C.; Harwood, D. T.; Rhodes, L. L.; Reeve, J.; Sim, J.; Munday, R., Acute Toxicities of the Saxitoxin Congeners Gonyautoxin 5, Gonyautoxin 6, Decarbamoyl Gonyautoxin 2&3, Decarbamoyl Neosaxitoxin, C-1&2 and C-3&4 to Mice by Various Routes of Administration. *Toxins (Basel)* **2017**, *9* (2).
119. Akbar, M. A.; Mohd Yusof, N. Y.; Tahir, N. I.; Ahmad, A.; Usup, G.; Sahrani, F. K.; Bunawan, H., Biosynthesis of Saxitoxin in Marine Dinoflagellates: An Omics Perspective. *Mar Drugs* **2020**, *18* (2).
120. Bhonde, V. R.; Looper, R. E., A stereocontrolled synthesis of (+)-saxitoxin. *J Am Chem Soc* **2011**, *133* (50), 20172-4.
121. Couture, J. F.; Trievel, R. C., Histone-modifying enzymes: encrypting an enigmatic epigenetic code. *Curr Opin Struct Biol* **2006**, *16* (6), 753-60.
122. Favrot, L.; Blanchard, J. S.; Vergnolle, O., Bacterial GCN5-Related N-Acetyltransferases: From Resistance to Regulation. *Biochemistry* **2016**, *55* (7), 989-1002.
123. Neuwald, A. F.; Landsman, D., GCN5-related histone N-acetyltransferases belong to a diverse superfamily that includes the yeast SPT10 protein. *Trends Biochem Sci* **1997**, *22* (5), 154-5.
124. Salah Ud-Din, A. I.; Tikhomirova, A.; Roujeinikova, A., Structure and Functional Diversity of GCN5-Related N-Acetyltransferases (GNAT). *Int J Mol Sci* **2016**, *17* (7).
125. Lao, Y.; Skiba, M. A.; Chun, S. W.; Narayan, A. R. H.; Smith, J. L., Structural Basis for Control of Methylation Extent in Polyketide Synthase Metal-Dependent C-Methyltransferases. *ACS Chem Biol* **2022**.
126. Chun, S. W.; Narayan, A. R. H., Biocatalytic, Stereoselective Deuteration of α -Amino Acids and Methyl Esters. *ACS Catal* **2020**, *10* (13), 7413-7418.

127. Prakash, G.; Paul, N.; Oliver, G. A.; Werz, D. B.; Maiti, D., C-H deuteration of organic compounds and potential drug candidates. *Chem Soc Rev* **2022**, *51* (8), 3123-3163.
128. Khoury, R.; Marx, C.; Mirgati, S.; Velury, D.; Chakkamparambil, B.; Grossberg, G. T., AVP-786 as a promising treatment option for Alzheimer's Disease including agitation. *Expert Opin Pharmacother* **2021**, *22* (7), 783-795.
129. Chun, S. W. Chemoenzymatic Synthesis of Chiral Amines by Carrier Protein-Dependent Enzymes. University of Michigan, University of Michigan Library, 2020.
130. Chang, H. Y.; Lo, L. H.; Lan, Y. H.; Hong, M. X.; Chan, Y. T.; Ko, T. P.; Huang, Y. R.; Cheng, T. H.; Liaw, C. C., Structural insights into the substrate selectivity of α -oxoamine synthases from marine *Vibrio* sp. QWI-06. *Colloids Surf B Biointerfaces* **2022**, *210*, 112224.
131. Mann, S.; Ploux, O., Pyridoxal-5'-phosphate-dependent enzymes involved in biotin biosynthesis: structure, reaction mechanism and inhibition. *Biochim Biophys Acta* **2011**, *1814* (11), 1459-66.
132. Skiba, M. A.
Structural and Biochemical Investigation of Methylation and Elucidation of t-Butyl Formation in Polyketide Biosynthesis. University of Michigan, 2018.
133. Dalhoff, C.; Lukinavicius, G.; Klimasauskas, S.; Weinhold, E., Synthesis of S-adenosyl-L-methionine analogs and their use for sequence-specific transalkylation of DNA by methyltransferases. *Nat Protoc* **2006**, *1* (4), 1879-86.
134. Sieber, S. A.; Linne, U.; Hillson, N. J.; Roche, E.; Walsh, C. T.; Marahiel, M. A., Evidence for a monomeric structure of nonribosomal Peptide synthetases. *Chem Biol* **2002**, *9* (9), 997-1008.